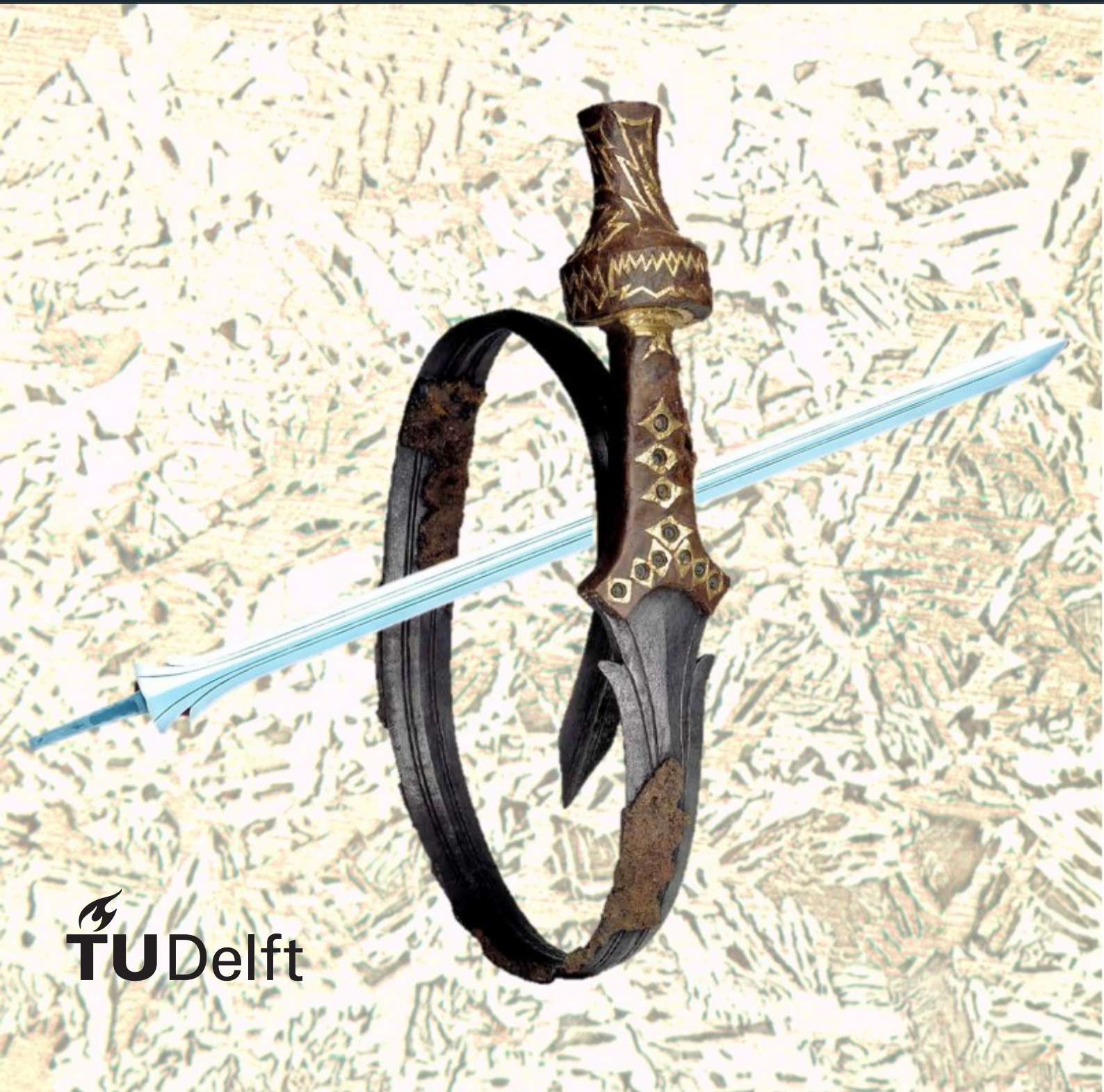


Dutch Bent Iron Swords

The Microstructure of Early Iron Age Hallstatt C Bent Swords from the Netherlands

Dorien Westert



Dutch Bent Iron Swords

The Microstructure of Early Iron Age Hallstatt C Bent Swords from the Netherlands

Thesis report

by

Dorien Westert

to obtain the degree of Master of Science
at the Delft University of Technology
to be defended publicly on June 25, 2024 at 13:00

Thesis committee:

Chair: Dr. M.J. Santofimia Navarro (TU Delft)
Supervisors: Dr. M.W.E.M. Alfeld (TU Delft)
Dr. I. Joosten (RCE, Cultural Heritage Agency of the Netherlands)
External examiner: Dr. G.H.J. Langejans (TU Delft)
Dr. M.H.G. Kuijpers (Leiden University)
Place: Faculty of Mechanical Engineering, Delft
Program: Materials Science and Engineering
Project Duration: May 2023 - June, 2024
Student number: 5596572

An electronic version of this thesis is available at <http://repository.tudelft.nl/>.



Copyright © Dorien Westert, 2024
All rights reserved.

Acknowledgements

During this time-travelling roller coaster called "Master Thesis", Teun is sitting next to me, supporting me from start to finish. I would like to thank Ineke Joosten for introducing me to this topic, giving me the opportunity to kick-start this ride, and accompanying me on many museum/research trips to collect information/data. Thank you, Maria Santofimia, for acting as chair in the thesis project, supervising my progress and ensuring that this roller coaster would not derail. Thank you, Matthias Alfeld for supervising this ride from beginning to end.

I would like to thank Thijs van de Manakker for his expertise and knowledge of forging and his help in creating the mock-up sword, Kees Kwakernaak for his expertise on SEM-EBSD and EPMA, Antonella Scherillo for her expertise on neutron diffraction and iron heritage objects, Sasja van der Vaart-Verschoof for her expertise on Dutch Iron Age archaeology and the ladies from the Valkhof Museum for their help and support regarding museum objects. These people helped design this roller coaster by creating additional loops, twists and turns that made it challenging and fun.

The remaining seats in this roller coaster are filled by the wizards of MSE, who filled the promised land with sweat and joy, the colleagues from the RCE, especially Hajar, Bart and Han, who filled the room with serious conversations, and my family who have sent postcards ever so often and created the safe haven that we call "Het Schapenmeer".

Thank you all for joining the ride.

Abstract

Deliberately mutilated weapons and other objects are repeatedly discovered in ancient burials from the Iron Age. This research is focused on the Early Iron Age bent swords from the Hallstatt C period (800-600 BC) found in archaeological sites in the Netherlands. Metallographic research methods are used to investigate how these swords were bent, i.e., using a blacksmith's fire or brute force. This elaborates on the Early Iron Age culture as it infers what kind of knowledge and skills were required for the bending process. With the help of a blacksmith, we created a replica to analyse the effect of different types of bending on the microstructure. This is compared with museum samples. Using optical microscopy and SEM(-EBSD) the microstructure of the museum sample and the replica are analysed for signs of deformation. Elemental analysis (SEM-EDS) is used on slag inclusion to estimate the initial iron and sword production processes. EPMA analysis was used to determine the carbon concentration throughout the samples, suggesting the use of wrought iron and hardening techniques. Results show that the Heythuysen sword contains multiple microstructure phases with various carbon concentrations. Most probably a combination of piling techniques and carburisation was applied during the production of the Heythuysen sword. The several bending methods of the replica show a distinction in the microstructure on the level of local misorientation. This is sensitive to the presence of inclusions and the changes in grain size and phase, which complicated the evaluation of the Heythuysen sword. The Heythuysen sword does not show strong evidence of bending by brute force and is most likely bent by a blacksmith with a fire.

Contents

List of Figures	vii
List of Tables	x
1 Introduction	1
I Literature Review on Ancient Swords	4
2 Historical Concept	5
2.1 Swords of Interest	5
2.1.1 Oss	6
2.1.2 Wijchen	8
2.1.3 Heythuysen	10
2.2 Production of Iron Swords	10
2.2.1 Production of Iron.	10
2.2.2 Welding and Forging	12
2.2.3 Casting	15
2.3 Why were the swords bent?	16
3 State of the art: Metallurgy	17
3.1 Hardening Mechanisms	17
3.1.1 The Effects of Carbon	17
3.1.2 Gangue Elements from the Iron Ore: Phosphorous	19
3.2 Microstructural Features	19
3.2.1 Fundamental Phases.	22
3.2.2 Slag	23
II Methodology	25
4 Experimental Procedure	26
4.1 Sample Selection and Construction	26
4.1.1 Museum Samples	26
4.1.2 Smithing of a Replica.	27
4.2 Experimental Materials and Techniques	29
4.2.1 Materials	29
4.2.2 Techniques	29
III Results and Discussion	32
5 Interpretation of the Results	33
5.1 Results of the Heythuysen specimen: H-CS-8	33
5.1.1 Phases	33
5.1.2 Slag Inclusions	36
5.1.3 Carbon	36
5.1.4 Crystallographic Characterisation	37
5.2 Results of the Domtoren specimens: D-1 and D-2	38
5.2.1 Phases	38
5.2.2 Slag Inclusions	40
5.2.3 Carbon	43

5.2.4	Crystallographic Characterisation	43
5.3	Results of the Not Bent Mock-up specimens: M-NB-rib and M-NB-edge	44
5.3.1	Phases	44
5.3.2	Slag Inclusions	45
5.3.3	Carbon	46
5.3.4	Crystallographic Characterisation	46
5.4	Results of the Hot Bent Mock-up specimens: M-HB-rib and M-HB-edge	47
5.4.1	Phases	47
5.4.2	Slag Inclusions	49
5.4.3	Carbon	49
5.4.4	Crystallographic Characterisation	50
5.5	Results of the Cold Bent Mock-up specimens: M-CB-rib and M-CB-edge	51
5.5.1	Phases	51
5.5.2	Slag Inclusions	51
5.5.3	Carbon	53
5.5.4	Crystallographic Characterisation	53
6	Discussion	55
6.1	The Heythuysen Sword	55
6.1.1	The Microstructure of the Heythuysen Sword	55
6.1.2	Slag Inclusions inside the Heythuysen Sword	57
6.2	The Original Anchorages of the Domtoren	58
6.2.1	The Microstructure of the Domtoren Anchorages	58
6.2.2	Slag Inclusions in the Domtoren Anchorages	59
6.3	The Mock-up Sword	60
6.3.1	The Microstructure of the Mock-up Sword	60
6.3.2	Slag Inclusions inside the Mock-up Sword	61
6.4	How were the Swords Bent?	61
6.4.1	The Bending Experiment of the M-series	61
6.4.2	Was the Heythuysen Sword Bent by Brute Force?	63
IV	Closure	64
7	Conclusion	65
8	Recommendations	67
	References	72
A	Summary of Results	73
B	Slag Inclusions: Elemental composition	76
C	Neutron imaging	83
C.1	Neutron Tomography	84
C.2	Time of Flight Neutron Diffraction	85
D	Measurements at INES	86

Nomenclature

List of Abbreviations

BCC	Body-centred cubic	NRC	Non-Reduced Compounds
BCE	Before the Common Era	NRCA	Nuclear resonance capture analysis
CCT	Continuous cooling transformation	OM	Optical microscopy
CE	Common Era	OPS	Oxide polishing suspension
EBS	Electron backscatter diffraction	RCE	Cultural Heritage Agency of the Netherlands
EDS	Energy dispersive X-ray spectroscopy	RMO	National Museum of Antiquities
EPMA	Electron probe microanalysis	SEM	Scanning electron microscopy
FCC	Face-centred cubic	ToF-ND	Time of flight - neutron diffraction
GAM	Grain average misorientation	WDS	Wavelength dispersive spectrometry
HAGB	High angle grain boundaries		
IPF	Inverse pole figure		
IQ	Image quality		
KAM	Kernal average misorientation		
LAGB	Low angle grain boundaries		

List of Symbols

α	Ferrite
α_w	Widmanstätten ferrite
α_{all}	Allotriomorphic ferrite
γ	Austenite

List of Figures

1.1	The prehistoric timeline of central Europe. Based on [1]–[3].	1
1.2	Distribution of Celtic people and languages. Based on [4], [5].	1
1.3	The anatomy of a Mindelheim sword. Drawings after [6]	2
1.4	Photographs of the current state of A) the sword of Oss, B) the sword of Wijchen, C) the sword of Heythuysen. Retrieved from [1].	3
2.1	Finding places of the swords of interest.	5
2.2	The conditions after the finding and first restoration of the sword of Oss and co-objects (situla, big bucket, right under), around 1934. Retrieved from [1].	6
2.3	The conditions after the second restoration of the sword of Oss and co-objects (around 1963). The main focus was on the sword and situla. Retrieved from [1].	7
2.4	The conditions after the third and final restoration of the sword of Oss and co-objects (around 1993). The entire set of objects is restored to recognisable items with minimal corrosion including the situla, the sword, horse-gear and ornaments. Retrieved from [1].	7
2.5	A close-up of the blade of the sword of Oss with clear ridges and attached pieces of wood and textile. Retrieved from [1].	8
2.6	All objects found in the wagon-grave of Wijchen in restored condition. Retrieved from [1].	9
2.7	Reconstruction drawings of the sword of Oss (bottom) and sword of Wijchen (Top) by R. Timmermans. Retrieved from [1].	10
2.8	A schematic illustration of a potential Iron Age furnace, including heat indication and reduction reactions. Retrieved from [23].	11
2.9	The colour change and forge resistance of wrought iron in relation to the temperature. Retrieved from [30].	13
2.10	Schematic illustrations of Celtic piling systems. 1) (i) edge to edge layering 2) (iii) diagonal arrangement 3) (ii) surface to surface bonding, retrieved from [9].	13
2.11	The forging process of sword production: 1) the stock 2) elongation toward the tip 3) broadening towards the tang 4) creating cutting edges 5) base of a simple sword 6) adding mid rib, ridges and/or ricasso notches 7) creating the shoulders or guard 8) adding the shoulders 9) additional pieces for a hilt. Retrieved from [9].	14
2.12	Iron-Carbon phase diagram. Retrieved from [34].	15
2.13	Celtic iron swords from Transylvania bent in various patterns. Retrieved from [7].	16
2.14	Bent Celtic iron swords from the Netherlands A) sword of Horst-Hegelsom before and after restoration, B) sword of Meerlo after restoration. Retrieved from [1].	16
3.1	Micrographs of Neumann bands A) in an iron Celtic blade research by Pleiner [9] and B) a carbon ferritic sample by Langford [39].	18
3.2	The microstructure of an iron Roman cleaver (200 CE) A) the heel of the cleaver and B) the blade of the cleaver. The red circles indicate slag inclusions, the blue boxes indicate bands of fine pearlite and the yellow boxes show broad bands of coarse grains of pearlite. Images retrieved from [48].	20
3.3	A graphical illustration of the phases present in the cross-section of six Roman swords (first century). The cross-sections are taken according to the schematic illustration in the right lower corner. Illustration retrieved from [37].	21
3.4	Old pearlite and cementite needle found in A) a nail from a Roman cistern (100 BCE) [44] B) a Roman nail [45] (100 BCE- 100CE) C) a Roman nail (500 CE) [45] D) Pilum Iberian (pre-roman) [51].	21
3.5	Examples from the literature regarding pearlite A) nucleation/growth [52], B) colonies [52] and C) spheroidisation [53].	22

3.6	Examples from the literature regarding allotriomorphic ferrite A) schematic illustration, B) broadened and C) almost no pearlite after intense broadening. Retrieved from [52].	22
3.7	Examples from the literature regarding Widmanstätten ferrite A) a schematic illustration and B) an optical microscopy example. Retrieved from [52].	23
3.8	Slag inclusions in wrought iron. Orange arrows) slag strings parallel to the surface and green box) slag strings perpendicular to the surface. SEM image retrieved from [22]	23
3.9	Distribution of oxides between the slag minerals. Note: these are the major oxides measured by SEM-EDS or EPMA, other forms/combinations of (hydr)oxides can exist in slag. Retrieved from [23].	24
3.10	Different types of Slags A) glass-wüstite in ferritic iron (1850 CE), B) glass-fayalite in ferritic-pearlitic iron (980 CE), C) glass in pearlitic-ferritic iron (980 CE). Retrieved from [35]. . . .	24
4.1	A) The labelled Heythuysen pieces. The yellow dashed line indicated the cross-section cut. B) Selected pieces of the Wijchen sword. Piece W-1 is circled red and specimen W-2 is in the yellow tube.	26
4.2	Furnace designed by Thijs van de Manakker for bending the replica of the sword of Oss. Photo by Thijs van de Manakker.	27
4.3	A and B) The anchors from the Domtoren. C) The cross-section of the anchor with a long slag inclusion running through the length. D) The bent tip of the anchor shows the split of the two piling layers.	28
4.4	A) The blacksmith's fire. B) The mock-up sword before bending. C) Bending the cold sword with a leverage effect. D) Bending the reheated sword by hammering.	28
4.5	All specimens in this thesis, the Heythuysen series, the Domtoren series and the Mock-up sword series.	29
5.1	Marcograph of H-CS-8, dividing the specimen in Upper- and Lower- Rib, Middle and Cutting edge. The orange circle indicates a Large α -Region, the red circles indicate α_w -Regions. The white square is the location of Figure 5.2.	34
5.2	OM of H-CS-8, showing the Widmanstätten microstructure near the surface of the sword, ferrite and pearlite alternating grains, the measurement lines of the EPMA and two types of slag inclusions. (blue: glassy. Yellow: wüstite-glassy/fayalite)	34
5.3	SEM images of H-CS-8 A) the Small α -Region and B,C,D) the α_w -Region.	35
5.4	SEM image of two types of slag inclusions in specimen H-CS-8 A) a cloud of little wüstite-glass slag inclusions and B) strings of glass slag inclusions. The green box and orange arrow refer to the elongation direction, see Figure 3.8.	35
5.5	Three groups of SiO_2/CaO NRC ratios: 10.1, 3.9 and 2.4.	37
5.6	Part of the C content from the Heythuysen sword (H-CS-8). EPMA results.	37
5.7	EBSD analysis on specimen H-CS-8, upper row are IPF +IQ images, lower row are KAM images. All images are acquired with a step size of 1 μm . The locations: A and D) near the cutting edge (α_w region), B and E) in the middle of the sample (half small α region, half α_w region) and C and F) the rib of the sword (large α region, small α region)	38
5.8	A) Macrograph and B) OM image of D1. The orange circles are large strings of inclusions.	39
5.9	SEM images of D-1 A) Large Pearlite Region and α_w -Region, B) higher magnification of the Large Pearlite Region, C and D) α_w -Region, E) Small α -Region and F) Large α -Region.	39
5.10	NRC ratio $\text{SiO}_2/\text{Al}_2\text{O}_3$ in D-1.	41
5.11	SEM-SED images on D2 with 4 types of inclusions.	42
5.12	Part of the EPMA line on the D2 sample.	42
5.13	The Carbon content (wt%) throughout specimen D1. (EPMA)	42
5.14	EBSD analysis on specimen D2 (large α region) A) IPF +IQ images and B) KAM image.	43
5.15	Macrograph of specimen M-NB-rib and -edge. The red lines are the location of the EPMA measurements.	44
5.16	SEM-EDS images of M-NB A and B) rib, Pearlite Region and Small α -Region, right edge, pearlite with allotriomorphic ferrite, C and D) right edge, α_w -Region, E) left edge, α -Region and α_w -Region and F) centre rib, Small α -Region.	45
5.17	Carbon content EPMA measurement of M-NB.	46

5.18 EBSD images of M-NB A) KAM of M-NB-rib, B) IPF+IQ of M-NB-edges and C) KAM of M-NB-edges	47
5.19 OM of M-HB-edge, Large inclusions separate the microstructures. The red line is the location of the EPMA measurements.	48
5.20 SEM of M-HB-edge A) a Large α -Region, B) a Small α -Region and C) a α_w -Region.	48
5.21 OM of M-HB-rib, deformed grains near the surfaces of the mock-up sword. A) the upper surface in the Small α -Region and B) the lower surface in the Large α -Region. C) Inclusions with glass pieces.	48
5.22 EPMA measurement of M-HB-rib and -edge.	50
5.23 EBSD analysis on specimen A,B) M-HB-rib and C,D) M-HB-edge both IPF +IQ image and KAM image (B. stepsize 2 μm , D. stepsize 1.5 μm).	50
5.24 macrographs of specimens M-CB-rib and -edges. White lines follow large cracks or inclusions; Red dots indicate the EPMA measuring line; Various phase regions are indicated.	52
5.25 SEM images and an OM image of the M-CB specimens. A) SEM (backscatter) show the pattern of inclusions. B) OM showing the α_w -Region transition into the Small α -Region. C) α_w -Region. D) Large α -Region. E) Transition between α_w - and Pearlite Region. F) Pearlite Region.	52
5.26 Carbon content, EPMA measurement of M-CB.	53
5.27 EBSD images (IPF+IQ and KAM) of specimen M-CB-rib.	54
6.1 CCT of a low alloy steel, retrieved from [62]	56
6.2 Defromation forces on a bent sword.	62
C.1 Schematic illustration of A) X-ray interaction, B) neutron interaction. C) The mass attenuation coefficient vs the atomic number for both x-rays (100 keV) and thermal neutron beams. Retrieved from [67].	83
C.2 White beam tomography images from the krisses researched in [69]. A) A horizontal slice through an entire blade and B) some vertical slices. C) A close-up of the tip of the blade. The red arrows point to the dark lines that represent the conjunction between layers as a result of piling. This would indicate a core layer with 2 outer layers. D) This is a close-up of another kris blade. It shows clear dark spots for slag inclusions and white lines for cracks. Retrieved from [69].	84
C.3 Schematic illustration of the diffraction of an incident beam on a set of lattice planes. Retrieved from [73]	85
C.4 Illustration of the Time of Flight Neutron Diffractometer INES at the ISIS neutron and muon source (UK). Retrieved from [77]	85

List of Tables

2.1	Heat colours for iron and steel forging. Retrieved from [29].	13
4.1	List of all specimens. *Part of the Thesis are specimens that are analysed by SEM-(EBSD), EPMA, OM and SEM-(EDS).	31
6.1	Microstructural comparison between H-CS-8 and D-1.	58
A.1	Summary of all observed microstructures.	74
A.2	Summary of all Slag Inclusions.	75

Introduction

This literature review goes back to approximately 800–650 BCE. In Central Europe, this period is part of the Early Iron Age and is called the Hallstatt C period. In Figure 1.1 a timeline shows part of Central Europe's prehistoric layout. The Iron Age is composed of the Early Iron Age, Hallstatt C and D period (800–450 BCE) and the Late Iron Age, La Tène periods (450 BCE - 1 CE) [1]–[3]. The Hallstatt periods A and B are part of the Late Bronze Age. Historians and archaeologists have defined these periods. In reality, these periods overlap, they gradually transform into each other and do not have strict boundaries in years or customs. The Hallstatt C period, known for its long double-edged swords, is shaped by the influence of several civilizations, including the Celts and Germans [1].

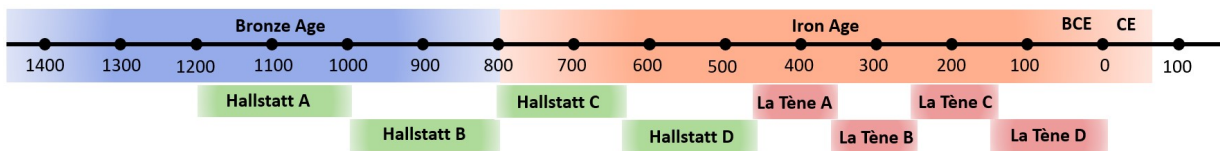


Figure 1.1: The prehistoric timeline of central Europe. Based on [1]–[3].

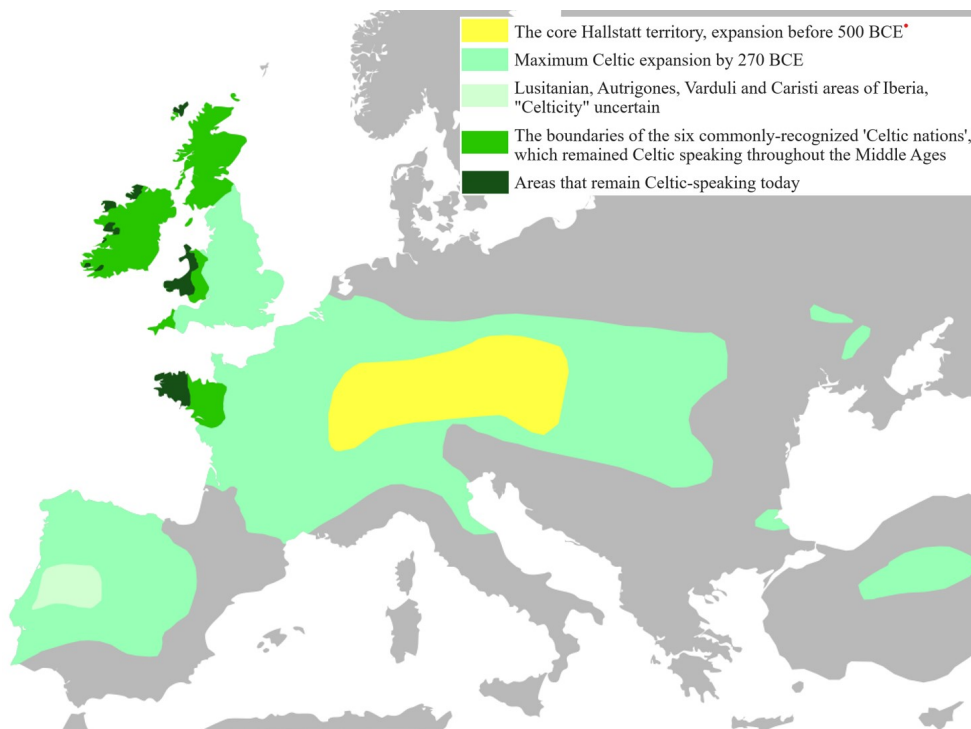


Figure 1.2: Distribution of Celtic people and languages. Based on [4], [5].

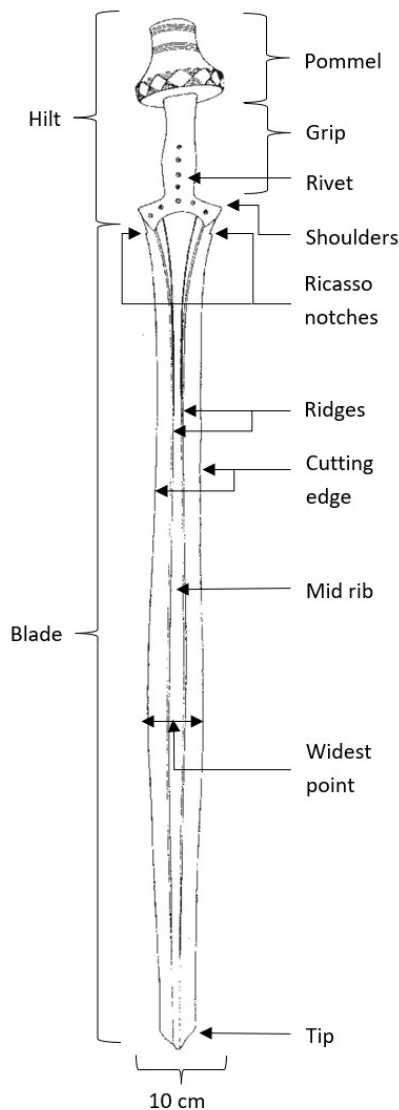


Figure 1.3: The anatomy of a Mindelheim sword. Drawings after [6]

The so-called Hallstatt culture was predominant in Central Europe, around the area of modern Austria, Switzerland, Czechia and the south of Germany as is shown in Figure 1.2 [4]. This area is based on the archaeological findings of chieftain burials with characteristic objects of the Early Iron Age Hallstatt period (i.e. iron swords/weaponry, horse-gear, wagon parts and other tools) [1]. During the Late Iron Age, the Celtic people and languages spread throughout Central Europe (Figure 1.2). It is therefore extraordinary that in the Netherlands and Belgium (an area not contiguous with the main Hallstatt area) dozens of excavations are recognized characteristics of the Hallstatt culture. Weapons have been found at several of these sites, including swords made of bronze and iron. Notably, most iron swords are categorized as characteristic Mindelheim swords, a type of sword linked to this period and area. Figure 1.3 shows an illustration of a Mindelheim sword and its characteristics. The swords are recognizable by the long blade, the hat-shaped pommels, the short ricasso notches, the ridges, and a relatively broad neck with its widest point low on the blade [1]. Most Mindelheim swords are made of iron, but some are made of bronze, which indicates the overlap between the Bronze and Iron Age. Typically, when uncovered, these iron swords are in a peculiar shape, often bent, folded, rolled, broken, or otherwise damaged [1]. Several archaeological theoretical frameworks are formed around the mutilated swords, connecting them to the customs of the Hallstatt culture [7]–[9].

Metallurgy can hold abundant information on the life cycle of a metal object including the production process, properties and use. Basic metallurgy research was performed on hundreds of Celtic swords from the La Tène period throughout the entirety of Europe. Pleiner [9], examined 27 swords with the use of cross-sections, optical microscopy and hardness measurements. Pleiner’s research was catalogued with 92 other examinations of La Tène swords. Hallstatt swords, conversely, are rarely examined on their microstructure. So far, no metallurgy research has been done on the Hallstatt swords found in the Netherlands and Belgium.

This thesis aims to use metallurgical research to determine *how* the swords were bent. Some careful predictions have been made on this topic. For example, Măndescu [7] briefly attempts to justify this by merely analysing the shape of the swords and suggesting folding and rolling techniques. However, this is not scientifically proven and does not exclude the use of reheating and a skilled smith. Moreover, (old) wrought iron is relatively soft, so brute manpower can not be excluded from the hypothesis.

The focus of the literature review is on three bent iron Hallstatt swords from the Netherlands, the bent sword of Oss (see Figure 1.4A), the bent sword of Wijchen (see Figure 1.4B) and the sword of Heythuysen (see Figure 1.4C)[1], [10]–[12]. This creates comprehensive background knowledge on Early Iron Age swords, beginning with the historical background of the swords of interest followed by a historical framework on the production and the possible mutilation of swords. Next, the state of the art in archaeometallurgy relevant to this project is addressed. The methodology presents the experimental procedure including sample selection as well as materials and techniques. The results are presented per specimen and are discussed in comparison to each other. The Heythuysen specimen represents the real old Dutch bent swords, the Domtoren specimens are the foundation for the Mock-up sword and the Mock-up sword is used for the testing of different bending techniques. The thesis is finalised with a conclusion and recommendations.

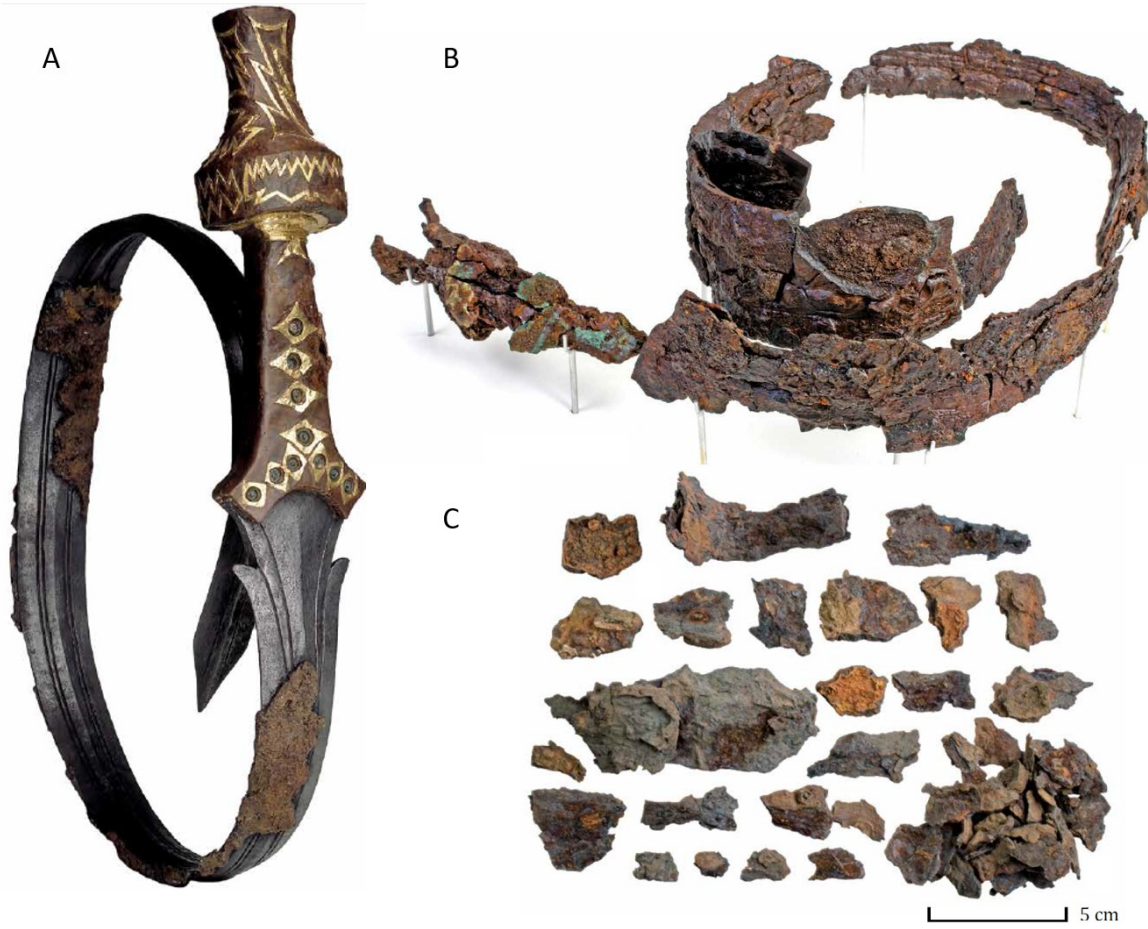


Figure 1.4: Photographs of the current state of A) the sword of Oss, B) the sword of Wijchen, C) the sword of Heythuysen. Retrieved from [1].

Part I

Literature Review on Ancient Swords

Historical Concept

In order to know what happened to the shape of the swords and to correctly interpret the metallurgical data, it is of the essence to understand the results of historical and archaeological research on the objects, as well as the hypothetical and historical framework surrounding the possible life cycle of the objects (production, use and destruction). Historical understanding enables targeted searches of the metallurgical data that could help fill gaps in the object's history. This chapter will describe the historical concept of the swords of interest, including the production of iron swords and historical theories on why the swords were bent.

2.1. Swords of Interest

The swords of interest for this literature review all originate from the Netherlands and are dated to the Hallstatt C period. They are named after the excavation locations; Oss, Wijchen and Heythuysen, as shown topographically in Figure 2.1. The swords of Oss and Wijchen are found in so-called '*vorstengraven*' or chieftains' graves, typically known as Early Iron Age graves. They can be recognized by their structure and wealth, which typically includes sets of grave goods, weapons, situla (bucket or big urn), horse-gear and wagon components [1], [10], [13]. Similar graves are found in the Hallstatt Culture area, the yellow area in Figure 1.2. Nonetheless, both grave areas have their own specific characteristics. For example, as of the Late Bronze Age in the Netherlands, cremation became a conventional way to treat the dead, whereas burials were more common in the main Hallstatt area [1], [14]. In the Iron Age in the Netherlands the addition of (metal) objects on or near the pyre became customary [14].

Sasja van der Vaart-Verschoof [1] and Nico Roymans [10] researched archaeological Iron Age findings in the Netherlands and Belgium and describe the findings from dozens of sites in detail, including the sites of interest. In the following sections, the swords of interest will be introduced in detail, mainly based on the research of Sasja van der Vaart-Verschoof [1], Nico Roymans [10] and Harry Fokkens [13], [15].



Figure 2.1: Finding places of the swords of interest.

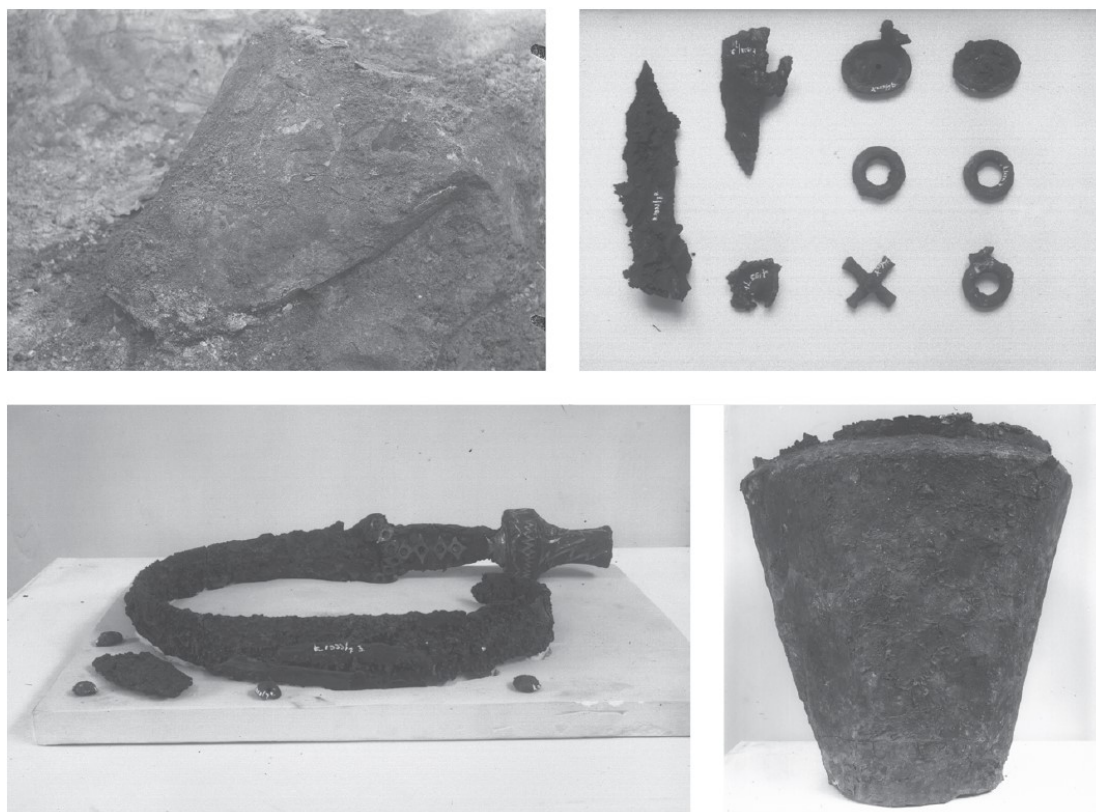


Figure 2.2: The conditions after the finding and first restoration of the sword of Oss and co-objects (situla, big bucket, right under), around 1934. Retrieved from [1].

2.1.1. Oss

The sword originates from a Chieftain's burial uncovered near Oss in 1933 [1], [10], [13], [15]. This Chieftain's burial is one of the most valued and researched prehistoric findings in the Netherlands and still provides new information for present-day studies. The bent sword was found inside a bronze bucket, also referred to as situla, together with many other objects, including human remains, horse-gear, tools and personal appearances. The sword was found in 6 pieces, including part of the wooden hilt with golden decorations in the form of lightning.

Over the years, the sword was restored three times, in 1934 by museum conservator D. Versloot, in 1963 by P.J.R. Modderman and in 1993 by Kempkens and Lupak. The state of the sword after the first restoration is pictured in Figure 2.2. Initially, two pieces of the sword were described as daggers or even a second sword. During the second examination in 1963 it was found that one 'dagger' was originally the tip of the sword, it was restored to its original placement. Figure 2.3, presents the state of the sword after the second restoration. A heavy corrosion layer is left on the surface of the sword. During the third restoration, it turned out that the second 'dagger' was also part of the sword. At this point, the full form and shape of the sword was restored, which resulted in a 117 cm long sword with a blade of 96 cm. The third restoration was an extensive restoration: the iron oxide corrosion layers were removed, the metal was polished, gaps were filled with polyester and missing parts were reconstructed. The final result after the third restoration of the entire set of grave goods is seen in Figure 2.4.

The third restoration treatment revealed multiple details on the sword. For one, the ricasso notches became visible on both sides of the double-edged sword, yet the cutting edge of the blade begins just below the notches. In addition, the removal of the corrosion layers reveals two ridges accentuated by two grooves, matching the central rib almost all the way down to the tip of the sword.

A considerable body of research has been conducted in exploring the historical and archeological features of the sword of Oss. Zooming in on the sword in its current state, it can be seen that several brown 'rusty' parts are still attached to the surface (see Figure 2.5). These brown parts are proven to be pieces of



Figure 2.3: The conditions after the second restoration of the sword of Oss and co-objects (around 1963). The main focus was on the sword and situla. Retrieved from [1].



Figure 2.4: The conditions after the third and final restoration of the sword of Oss and co-objects (around 1993). The entire set of objects is restored to recognisable items with minimal corrosion including the situla, the sword, horse-gear and ornaments. Retrieved from [1].



Figure 2.5: A close-up of the blade of the sword of Oss with clear ridges and attached pieces of wood and textile. Retrieved from [1].

wood and textile. In Figure 2.5, three of the brown preserved parts that are attached to the sword are shown in detail; the two lower parts are wood and the upper part is textile. Research could not identify the origin or function of the wooden parts. On the contrary, research on the textiles led to interesting results, suggesting that the sword was wrapped in several layers of cloth before it was laid to rest inside the bronze bucket [16]. Extensive research on textiles from the Hallstatt period has been done [17], [18]. In addition, the gold decoration found on the hilt led researchers to believe that this specific sword was not used in battle, since frequent and rough use would cause the decoration to wear off the grip. Also, the riches of the decorations are extensive and might indicate a showpiece. The ornamentation on the hilt is similar to the hilts of three swords found in the Hallstatt Culture area one from Gomadingen (Baden-Württemberg, Germany) and two from Hallstatt (Oberösterreich, Austria) [19]. Not only the 'lightning design' is similar, but also the craftsmanship and the use of expensive materials such as gold, amber and ivory, are comparable [19]. Because of this analogy, archaeologists suggest that the sword of Oss is not created in the Netherlands but instead was imported from the Hallstatt area. Moreover, the presents of part of the wooden hilt attached to the sword suggest that the sword was not burned during the cremation of the Chieftain. ^{14}C -dating analysis on the human remains and wooden objects found with the sword, resulted in dating to 1005-855 BCE (the wood fragments) and 790-540 BCE (the bone remains), which equates to the Hallstatt C period. After the extensive research that has been done on the sword, researchers are highly confident that the sword's current shape is accurate. The sword is currently in possession of the National Museum of Antiquities in Leiden.

2.1.2. Wijchen

In 1897, a wagon-grave containing the second sword of interest, was found in Wijchen. A wagon-grave is another type of traditional chieftain burial in which the dead were buried or cremated together with a four-wheeled wagon. This specific wagon-grave is extraordinary, for it is the only grave containing the metal fragments of the entire wagon, the bridles, yoke, wagon-box and wheels (see Figure 2.6). For many years the focus of the grave was concentrated on the wagon and only a select number of the grave goods. The sword was in a rather poor condition, which suggests long-term ignorance of the object. It existed out of several dozen pieces and the only facts known about it are that it is bent iron and has a central rib. In 2011, at the request of S. van der Vaart-Verschoof the sword was restored by R. Meijers of Museum Het Valkhof.



Figure 2.6: All objects found in the wagon-grave of Wijchen in restored condition. Retrieved from [1].

The restoration process involved assembling the pieces of the sword [20]. Unfortunately, the established outline of the sword is not fully secured, as no reasonably fitting spots were found for all parts of the puzzle [20]. The fitting pieces were cleaned by glass bead blasting, impregnated with Paraloid B27 and glued together with Uhu-Hart or Paraloid B27 [20]. In the restoration report, the conservator concludes that the presence of pitting corrosion, hollow spaces inside the iron, can be a sign of corrosion reactions with air. This leads to the suggestion that this sword was buried in a spacious 'bucket', like the situla from the Oss burial [20]. Unfortunately, a ceramic or metal situla is missing from the Wijchen burial. The sword after restoration is shown in Figure 1.4B.

After the restoration, multiple aspects of the sword were clarified to a certain extent. First, the construction of the blade is similar to the blade from the sword of Oss. The sword of Wijchen has a double edge blade with a central rib and double grooves on both sides, which forms small ribs parallel to the central rib. The grooves overlap each other gradually until only the central rib reaches the tip of the blade. Similar to the tip of the sword of Oss, the sword of Wijchen has an unusually pointed tip. Unlike the sword of Oss, the tang (the metal core of the hilt) is formed like a nail with a square cross-section and a knob. Visualizing all the features of the swords in a straight position led to the reconstruction seen in Figure 2.7. It is obvious that the sword of Wijchen is missing some of its fragments. Nevertheless, S. van der Vaart-Verschoof estimated the original length of the sword between 105-115 cm.

Taking into account all features of the sword, especially the tang, S. van der Vaart-Verschoof labelled the sword of Wijchen as 'one of a kind' since no significant other with this complete set of characteristics has yet been found. Consequently, regarding these unique features, it has been theorized that the sword of Wijchen was made in the external image of the sword of Oss, without the shape of the tang inside the hilt being known. The sword of Wijchen might be a locally produced sword instead of an imported product from the Hallstatt Culture.

Whether the iron objects from the wagon-grave were burned during cremation cannot be determined by visual observation. Although some bronze residue is found, no remains of a wooden hilt or such are found on pieces of the sword. S. van der Vaart-Verschoof substantiated that in the case of the Wijchen burial, it is most likely that the entire wagon was placed on the pyre and burned. The main arguments are the heat distortions on the bronze objects. A pre-historic cremation pyre can reach over 1000°C and even 1200°C in the centre [14], [21]. These are temperatures that can easily alter bronze but not iron objects.

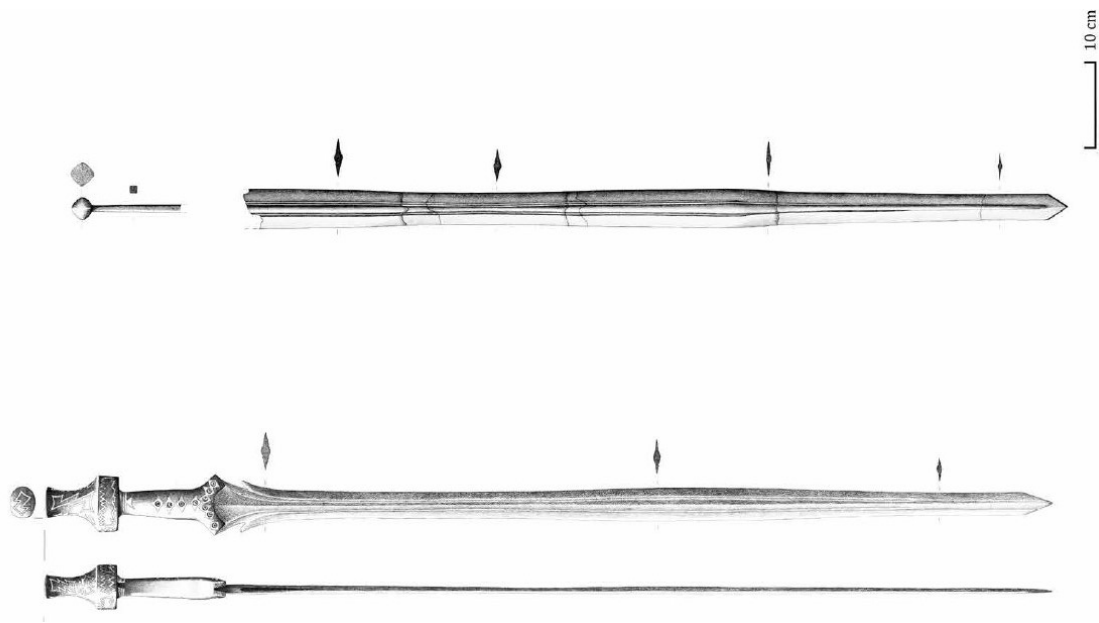


Figure 2.7: Reconstruction drawings of the sword of Oss (bottom) and sword of Wijchen (Top) by R. Timmermans. Retrieved from [1].

Moreover, temperature fluctuations are present in the entire pyre and are hard to track, so the degree of deformation of a metal object by heat cannot be linked to a specific spot or temperature inside the pyre [14], [21]. Because the temperature of pyres is below the melting point of iron objects it is not possible to visually determine the object's presence in the fire. Thus, the sword of Wijchen was feasible present in the pyre because most of the bronze objects in this grave were, but there is no hard evidence. The sword is currently in possession of the Valkhof Museum in Nijmegen.

2.1.3. Heythuysen

The sword of Heythuysen has a vague history and not much is known about it. In documents, it is said that the sword was found and discarded in 1934 by a farmer, probably during plowing. An amateur archaeologist subsequently picked it up and donated it to the National Museum of Antiquities in Leiden. At one point in history, there was uncertainty about the finding place of the sword. L.D. Keus (1881-1948) connects the find to the Busjop urnfield by Heythuysen [11]. The only fact known about it, is that bent pieces of iron, most likely originated from a sword, were found inside an urn. This sword is not restored or reconstructed. The condition of the sword makes it impossible to confirm the sword to be a Mindelheim type, and it complicates dating the object (see Figure 1.4c). This archaeological finding is dated to the Hallstatt C period based on the typochronology of the urn. The sword pieces are still in possession of the National Museum of Antiquities in Leiden.

2.2. Production of Iron Swords

The production process has a major impact on the final physical and chemical properties of a metal object. For example, both chemical and phase compositions are highly dependent on the raw material, the refining process, the welding and forging process and heat treatments. The composition can in turn influence the physical properties, such as hardness and ductility. Therefore, it is in the best interest of this thesis to outline the most plausible production process.

2.2.1. Production of Iron

Before a smith in the Iron Age can create a sword, malleable iron needs to be extracted from iron ore. The most common form of worked iron at this time was wrought iron, it was the first form of iron used in the production of weapons and tools [22]. According to the Oxford Advanced Learner's Dictionary, the word 'wrought' comes from the old form of the past tense of work. This refers to an important property of wrought

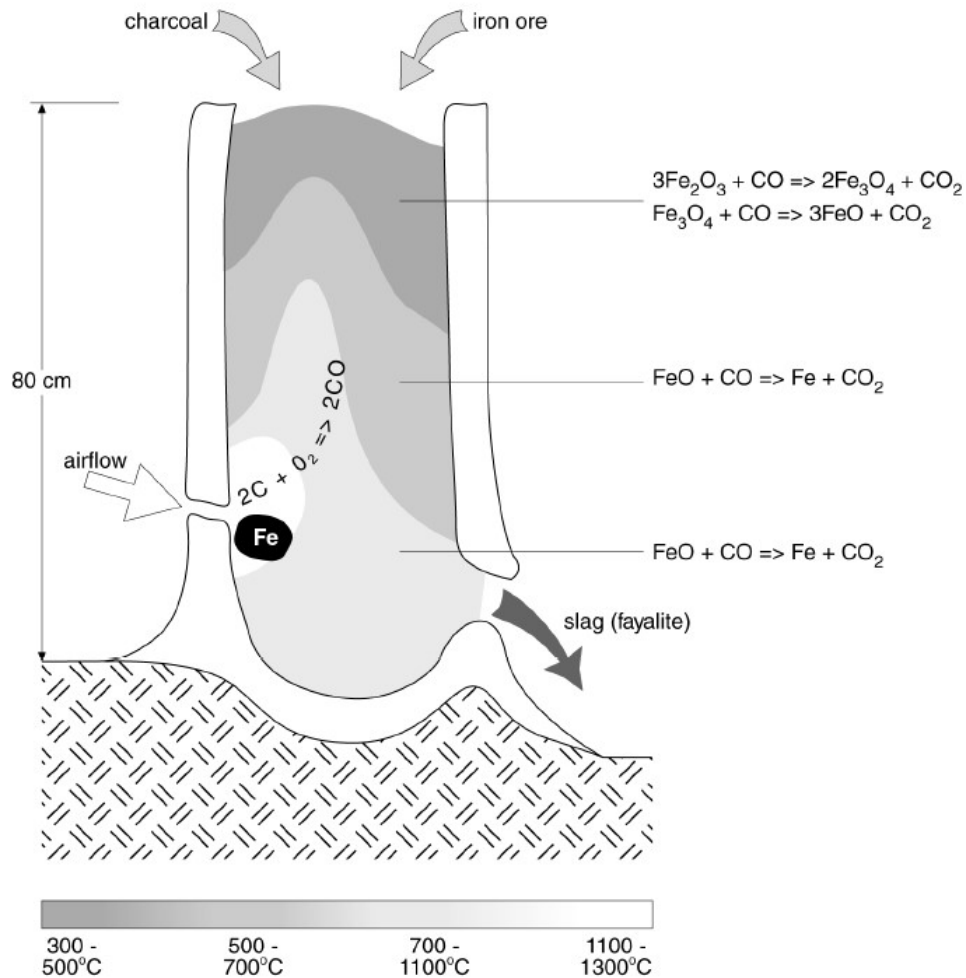


Figure 2.8: A schematic illustration of a potential Iron Age furnace, including heat indication and reduction reactions. Retrieved from [23].

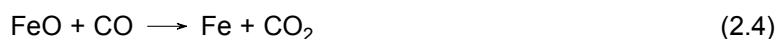
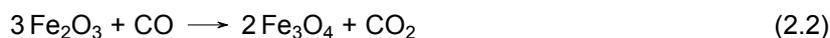
iron, namely that it could be hammered (worked) into shape. It is crucial to state that no evidence (e.g. slag or furnaces) of Early Iron Age iron production in the Netherlands exists other than the iron artefacts themselves [23].

The main process of Iron Age wrought iron production is the bloomery- or direct- process. During the bloomery process, iron ore and charcoal are heated in a primitive furnace to a temperature up to 1200°C [22], see figure 2.8. There are several models of primitive furnaces, with the earliest furnaces believed to be underground, followed by furnaces with a shaft [23], [24]. Figure 2.8, shows a slag-tapping furnace which is a model that was applied in Europe from the Late Iron Age to the Late Middle Ages [23]. During the Hallstatt C period, the period of the swords of interest, an underground furnace was more likely to be used. Often iron ore is pretreated by roasting at temperatures of 500°C and higher to extract water and other organic material [23]. The iron ore contains forms of iron (hydr)oxides and residual compounds such as silicates, calcium, manganese and phosphorous [23]. Charcoal has more than one function in this process, it fuels the furnace, it acts as the reducing agent for the iron ore reduction and it shields the hot metal against oxidation [22], [23], [25]. In the hot furnace, the charcoal burns away and the ore moves down the shaft through the reducing zones [23]. Iron ore in the form of hematite (Fe_2O_3), magnetite (Fe_3O_4) and wüstite (FeO) reacts with the carbon monoxide, which is released by the charcoal, and forms metallic iron $Fe(s)$ [22], [23]. This reducing atmosphere is responsible for the very low amount of carbon diffusing into the metal. The metallic iron is coated with the extracting slag, which prevents re-oxidation once the metallic iron reaches the more oxidising area of the air inlet and prevents carbon diffusion into

the iron [23]. The following reactions are examples of the iron ore reduction [22], [23], [26]:



or



The result of this process is a sponge-like porous, solid lump of iron called "bloom" (hence the name Bloomery process) and liquid slag. Slag is formed by non-metallic impurities and often occurs in the form of Fayalite, a silicate of iron (Fe_2SiO_4), which becomes viscous at a temperature of about 1176°C [22], [23]. The heated sponge of iron is subsequently hammered to squeeze the residual slag out of the pores and form a more compacted lump of wrought iron [22], [25], [26]. The final product, wrought iron, is a ferrous material with low carbon levels (< 0.02 wt%), high slag inclusions and impurities and without intentional alloy additions [23], [25], [26]. This makes wrought iron a relatively ductile metal which is easily hammered and joined by welding.

The further evolution of iron production starts rather late. In the 13th century, mechanically driven bellows and hammers upgraded the production process [27]. The first blast furnaces in Europe, based on the Bloomery furnaces, were built in the mid-14th century; They produced brittle, high-carbon pig iron, or liquid cast iron, which had to be refined to reduce carbon content and brittleness so that it could be malleable [24], [27]. From the 16th century onwards, the development of iron and steel increased, including among other things rolling and drawing techniques [24]. In the Netherlands, the first known blast furnace dates from the 17th century [23]. In the 18th century, coke replaced charcoal which led to the puddling furnaces; a technique that converts blast furnace-produced pig iron into wrought iron [24], [28]. The most famous example of a wrought iron construction via the puddling process is the Eiffel Tower (1889). Wrought iron was up until the 19th century the most important ferrous material used in Europe until in the 20th century the era of stainless steel started [22], [24], [25]. In 1918 the first blast furnaces in the Netherlands were established in IJmuiden, they were called the Koninklijke Nederlandse Hoogovens en Staalfabrieken (KNHS).

2.2.2. Welding and Forging

When forging, it is important to roughly know the temperature as it affects the metal phase and therefore the treatment itself. An easy and sensible estimation of the temperature can be done based on the heat colour, this is a technique still used in modern blacksmithing. Table 2.1, presents the relation between heat colour, temperature and heat treatment as taught in modern blacksmithing workshops [29]. The keen eyes and skilled hand of the ancient blacksmith might have noticed a few more aspects while forging wrought iron. The heat colour of wrought iron has a glitch in the colour change at about 900°C , which goes along with a glitch in the forge resistance during forging, see Figure 2.9 [30]. This is now known as the ferrite-austenite phase transition, and while ancient smiths did not know this, they could have noticed a sudden change in the orange heat colour and temporary strengthening of the metal [30].

The first step in creating a sword from a slab of wrought iron is to weld a stock, a rough bar that will serve as the basis for forging the blade. A schematic drawing of a stock is shown in figure 2.11.1. The stock can be formed from a single piece of metal, although this has some disadvantages. Firstly, a wrought iron slab big enough to form the blade must be produced, which is a hard job because the bloomery process often results in an iron slab too small to forge an entire sword. Secondly, the carburisation of large solid pieces of metal creates concentration gradients that result in overly carburised edges and a poorly carburised core [26]. A solution to overcome these disadvantages is to apply a method, already known by Celtic smiths in the La Tène period, named piling. It is uncertain if piling techniques were known in the Hallstatt period. For this method, smaller pieces of (non-)carburised iron are forge-weld together. Lang [31] and Pleiner [9] describe several piling arrangements found in Celtic swords, based on phase

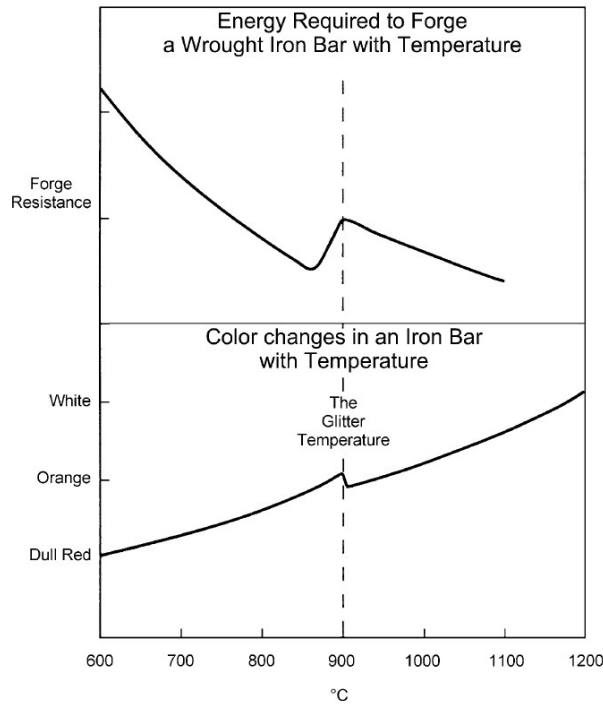


Figure 2.9: The colour change and forge resistance of wrought iron in relation to the temperature. Retrieved from [30].

Colour	Temperature (°C)	Suitable Processes
Black red	420-590	Toughening carbon tool steel after quenching. Tempering high-speed steel
Very dark red	590-700	
Dark red	700-815	Hardening and annealing carbon tool steel
Cherry red	815-870	Hardening alloy tool steel
Light cherry red	870-980	Hardening alloy tool steel
Orange red	980-1090	Hardening alloy tool steel
Yellow	1090-1260	
Yellow white	1260-1371	Hardening high-speed steel
White	1371-	Welding

Table 2.1: Heat colours for iron and steel forging. Retrieved from [29].

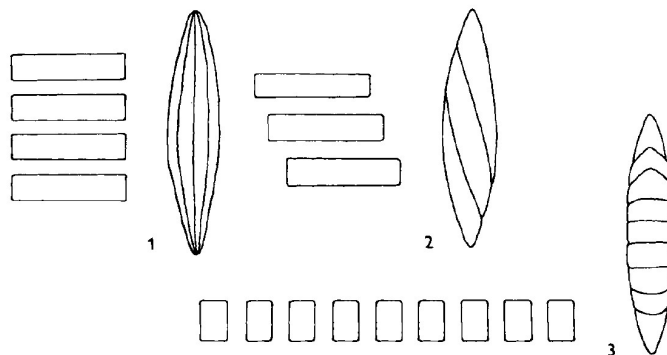


Figure 2.10: Schematic illustrations of Celtic piling systems. 1) (i) edge to edge layering 2) (iii) diagonal arrangement 3) (ii) surface to surface bonding, retrieved from [9].

composition, the distribution of slag and ghost bands [9], [31]: i) Multiple flat bars are welded together with the broad face horizontal, stacked similar to a sandwich. Lang [31] named this piling construction 'edge to edge layering' (see Figure 2.10.1). ii) Several rod-like bars are welded together which results in joints running transversely (surface to surface) across the blade (see Figure 2.10.3). iii) Pleiner [9] also illustrates a diagonal arrangement of flat bars as shown in figure 2.10.2. After piling the smith can decide to further refine the stock by fold-welding. This is a process where the stock is repeatedly reheated, folded over, and welded together again [9]. It refines the stock by dispersing trapped slag and carbon through physical displacement and diffusion during heating [9]. When the stock is finished the forging of the blade can begin.

The forging of a blade is a time-consuming and challenging process. Pleiner provides a detailed description of the process, including a comprehensible illustration [9], see Figure 2.11. Shortly summarized, first, the stock needs to be elongated by annealing cycles of (orange-) heating to about 1000 °C and hammering in the longitudinal direction, see Figure 2.11.2. Secondly, the stock needs to be broadened, which is done by reheating and hammering in the direction of the edges and the hilt, see Figure 2.11.3. Next, the two cutting edges of the Celtic sword are created by tilting the sword on the anvil and placing the point of impact on the edge only, again with cycles of heating, see Figure 2.11.4. The smith has to create a pointed tip and ensure that the blade is straight, see Figure 2.11.5. Optionally, the smith can choose to create a midrib. Therefore, the sword was reheated, placed over the edge of the anvil, and hammered with the edge of the hammer, see Figure 2.11.6. Finally, the smith is challenged to smooth out the sword with the edges exactly parallel from each other. This process can contain hundreds of heating cycles and requires experience and patience. After forging the sword to the smith's liking, the smith can choose to apply carburisation or heat-treatment techniques to strengthen the sword. In the Iron Age, knowledge of carburisation and heat-treatment techniques such as quenching and tempering was most probably known at a basic level. This assumption is supported by the fact that evidence of these techniques is irregularly found in Iron Age metal objects [31].

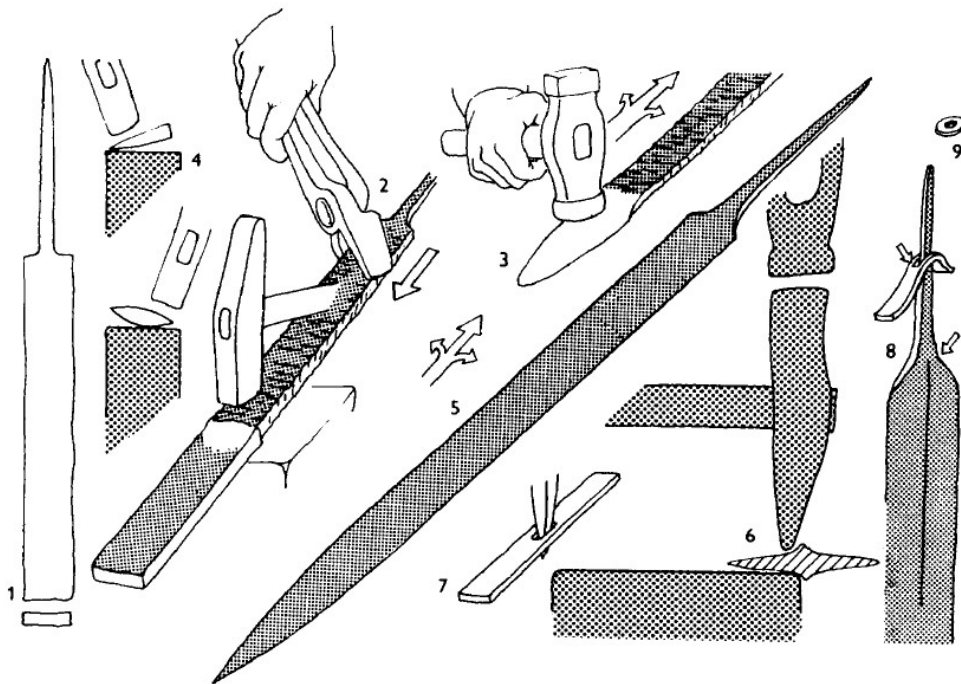
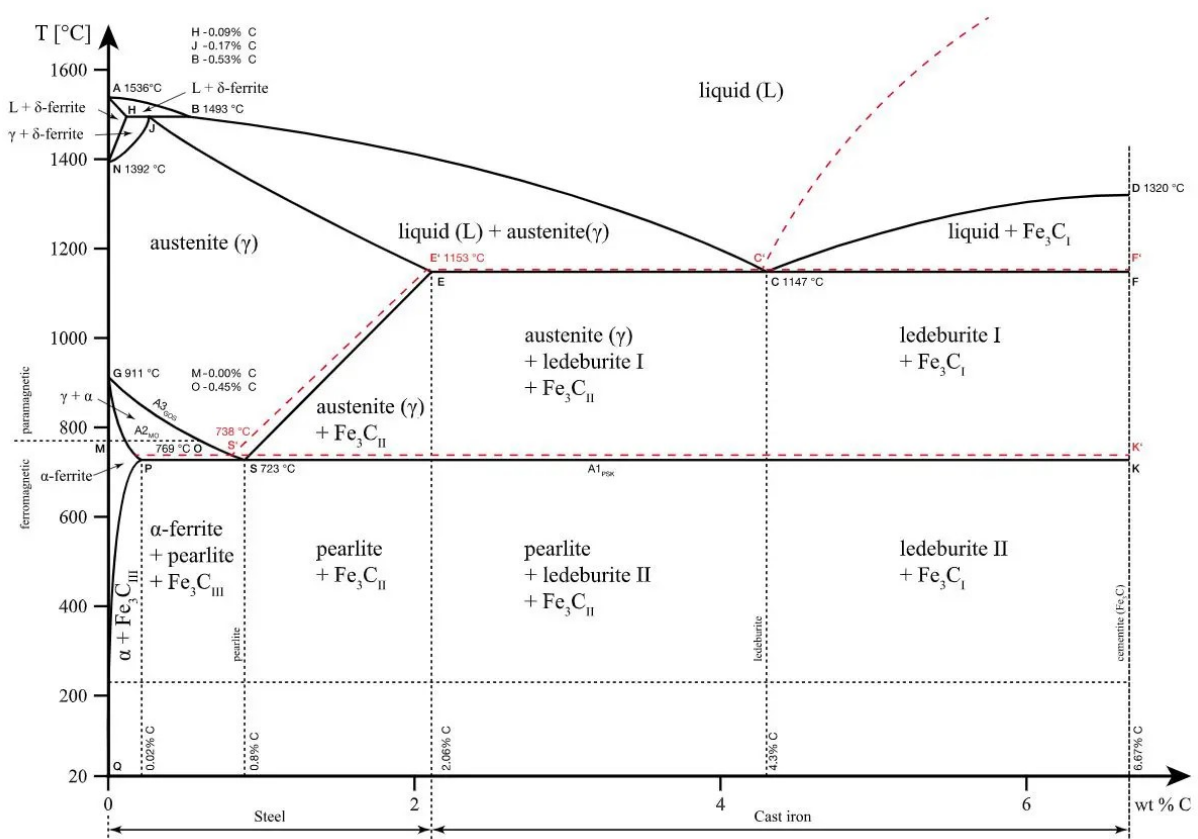


Figure 2.11: The forging process of sword production: 1) the stock 2) elongation toward the tip 3) broadening towards the tang 4) creating cutting edges 5) base of a simple sword 6) adding mid rib, ridges and/or ricasso notches 7) creating the shoulders or guard 8) adding the shoulders 9) additional pieces for a hilt. Retrieved from [9].

2.2.3. Casting

The entire sword production process, including the bloomery process, demands much time and a highly skilled smith. A justifiable question regarding sword production is: "Why not cast an iron sword?" Casting is a technique that was already known in the Bronze Age, long before the use of iron. Casting requires liquid metal to be poured into a mold. The melting point of pure iron is around 1536 °C, but for wrought iron (mostly ferritic) with a carbon concentration below 0.02 wt% the melting temperature can drop slightly to around 1493°C (see Figure 2.12). Figure 2.12 is an Iron-Carbon phase diagram, showing the iron phases in relation to the carbon percentage and the temperature. Ferrite is a Body-Centred Cubic (BCC) structural phase of iron, which allows for minimal space for carbon interstitials. When heated above 900°C it transforms into austenite, which has a Face-Centred Cubic (FCC) structure with more space for carbon atoms and thus slowly absorbs carbon from the environment. In case the final carbon concentration is between 0.02 wt% and 2.06 wt%, the product can be called steel. The diagram shows that the melting temperature for steel can decrease to just below 1400°C, whilst for cast iron (> 2.06 wt%) the eutectic temperature of 1147°C is the minimum melting temperature. Generally, the ancient furnaces used for iron reduction were heated to a maximum of about 1250°C which would challenge the limit of the refractories in the furnace [23]. However, this was not a hard limit. It was possible, depending on the type of furnace and the building material, to increase the temperature for a longer time to absorb carbon into the iron and create liquid cast iron [23], [32]. Since it was possible to create cast iron in the Iron Age, it is not surprising to find evidence of this in the archaeology [32]. While cast iron has the advantage of castability, it has the disadvantage of being extremely brittle and cannot be hot- or cold-worked [33]. This means that it can not be shaped by hammering, which appears to be the preferred production technique of iron swords in Europe during the Iron Age. It is out of the scope of this thesis to find the reason behind this preference.



2.3. Why were the swords bent?

The question of *why* the swords were bent is not the topic of this thesis, but this question can provide background information on *how* the swords were bent. The swords of interest are unique due to their shape in combination with the finding location and dating, but throughout Europe numerous bent or deformed swords were found dating back to the late Bronze Age until the start of the Common Era. Figure 2.13 shows bent Celtic iron swords from the area of Transylvania, showing a variety of deformations. Archaeologists identify deformed swords in graves exclusively as Celtic culture and have suggested several theories as to why these weapons were deformed [7].

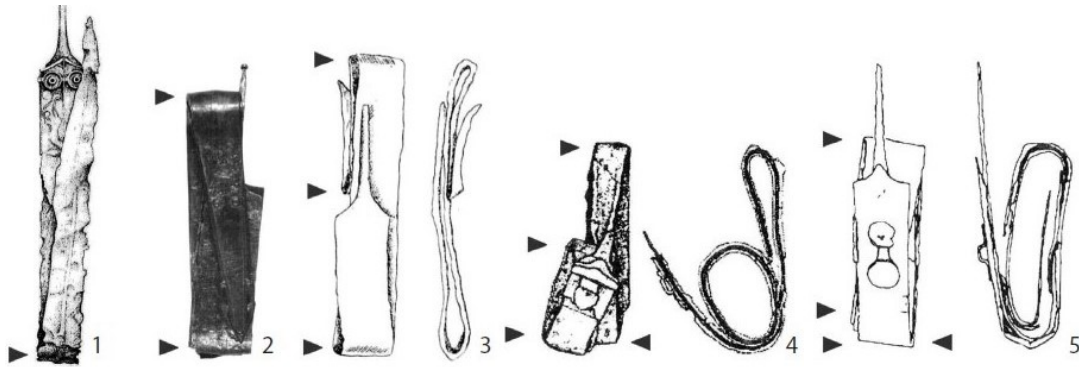


Figure 2.13: Celtic iron swords from Transylvania bent in various patterns. Retrieved from [7].

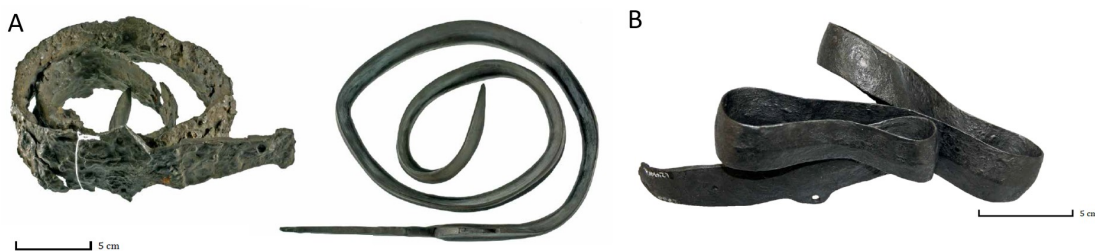


Figure 2.14: Bent Celtic iron swords from the Netherlands A) sword of Horst-Hegelsom before and after restoration, B) sword of Meerlo after restoration. Retrieved from [1].

One obvious theory is to associate the damage of a weapon with the outcome of a fight. Either the combat itself damaged the sword or the outcome of the battle required it [9]. For example, sacrificing the weapons of defeated enemies or ritually associating a weapon with its renowned warrior [9]. The latter can be substantiated by religious arguments; A sword could be seen as an extension of the body and thus can be killed alongside its warrior [7]. The sword is said to have a symbolic status and could be ritually 'killed' during the burial ceremony of its warrior [7]–[9]. According to some, publicly destroying weapons during a burial ritual would prevent grave robbery because the weapons are not utilizable anymore [7]. A more practical matter would be the fit of long swords in cremation graves. Some of the bent swords, like the sword of Oss, are found inside an urn, together with cremated bones [1]. To fit inside the urn can be a valid reason for the deformation [7]. Bent swords are not the only deformed tools that are found in Celtic burials. Spearheads, knives, and even household tools, jewellery, and pottery were found in a seemingly unnatural deformed state [7], [8].

In the Netherlands, only a few other bent swords from this age were found, including the sword from Horst-Hegelsom shown in Figure 2.14A and the sword from Meerlo shown in Figure 2.14B [1]. Both swords are dated to the Hallstatt C period and are recognized as type Mindelheim swords, similar to the sword of Oss. The swords have a specific shape which is unlike the sword of Oss or Wijchen. The sword of Horst-Hegelsom is most comparable to the swords of interest but has a sharp corner in the round spiral. On the other hand, the sword of Meerlo is clearly folded instead of bent in a spiral. This indicates that multiple methods of deformation were used in the Netherlands during the Hallstatt culture.

State of the art: Metallurgy

The study of the physical and chemical behaviour of metals is called metallurgy. The manufacturing and processing of metals is reflected in the microstructure and composition, which in turn influences the properties of the metal. In this section, the hardening mechanisms are discussed due to the importance of the hardness property of swords. Furthermore, hypothetical microstructural features are introduced, including expected metal phases and slag minerals. It is important to anticipate the physical and chemical properties of the swords in order to formulate plausible hypotheses about the bending process.

3.1. Hardening Mechanisms

The composition of wrought iron mainly consists of pure iron in the form of ferrite (α) which exists in a BCC structural phase (Figure 2.12). Other elements dissolved as a solid solution inside the ferrite structure can greatly affect the properties of the iron object. Elements such as silicon, manganese, aluminium and phosphorus derived from the iron ore in oxide forms can only enter the iron lattice structure after oxidation [9], [22], [35]. Other elements such as calcium, magnesium and potassium are derived from the coal ashes. Carbon, which comes from coal or air, contributes significantly to the hardness of iron. Fortunately, most of the gangue elements (Si, Mn, Al, P, Ca, Mg, K) leave the iron bloom via the slag. Therefore, slag inclusions remaining in the iron provide a reasonable perspective about the iron ore used. A common ore found in Europe and the Netherlands is bog iron ore, which generally contains a high concentration of phosphorus, some of which ends up in the iron lattice and greatly affects the hardness and brittleness of the iron.

3.1.1. The Effects of Carbon

Although the iron swords of interest are more than 2500 years old, there exist written texts about the quality of Celtic swords. A Greek historian, Polybius (200 BCE - 118 BCE) [36], described battles between the Romans and Gauls, a Celtic group from modern-day France in the La Tène period. Lang (1988) [37] quoted the following passage from Polybius to point out the weak qualities of the Gaulish swords: *"...could only give one downward cut with any effect but after this the edges were so turned and the blade so bent that unless they had time to straighten them out with their foot against the ground, they could not deliver a second blow... their blade has no point."* Unlike Gaulish swords, the Roman swords were described as strong weapons with sharp and hard points, suitable for thrusting [37]. In general, both Roman and Celtic swords were made of iron around 150 BCE, yet a significant difference in the quality of ironworking surfaces. In literature, several hardness measurements on Celtic swords were performed. The perceived values vary from 130 HV to 540 HV with a rough average of 250-300HV at the cutting edge and 150-200HV at the central rib [9], [31], [38].

The historical text quoted above denotes the low hardness of Celtic swords. The property of hardness is generally defined as the material's resistance to permanent deformation and can be understood as the cutting ability and wear resistance of a sword. Additionally, the fracture resistance or the amount of deformation a material can undergo before fracturing is referred to as toughness. The increase in hardness correlates with the increase in brittleness which is defined as the tendency to fracture under stress while associated with minimal deformation. Ideally, a swordsmith strives to create a tough core with hard sharp edges [38].

There are several techniques to increase the hardness of an iron object. One of the techniques is carburising, which entails the absorption of carbon into the iron crystal structure as discussed in 2.2.3. Wrought iron, produced as described above, has a low carbon content and consists mainly of ferrite, resulting in a significantly soft metal. Once, due to carburisation, the carbon content is increased, the hardness increases as well. Pleiner [9] researched over a hundred Celtic swords, and of all full cross-section examinations about 40% of the swords were made of wrought iron (no pearlite, 0.02-0.05 wt% carbon) and very mild steel (< 0.3 wt% carbon), whereas the remaining swords contained medium (0.6 wt% Carbon) or hard (0.7-0.8 wt% Carbon) steel cutting edges. In a scenario where a smith heats a sword long enough to carburise the centre, the cutting edges will become overly carburised and become too brittle for use, which can be problematic [38]. Therefore, carburising is not an easy technique. Previous research states that Celtic smiths knew carburisation techniques before the solution of piling was discovered [31] (see section 2.2.2).

Another manner to increase the hardness is quenching. Quenching is the rapid cooling of the metal, often done by immersion in water. Due to a slow diffusion rate, the carbon atoms do not have enough time to escape the crystal structure, resulting in an extremely hard martensite structure. Although quenching is nowadays well known, previous research concluded that Early Iron Age sword smiths generally did not practice quench-hardening [9], [38].

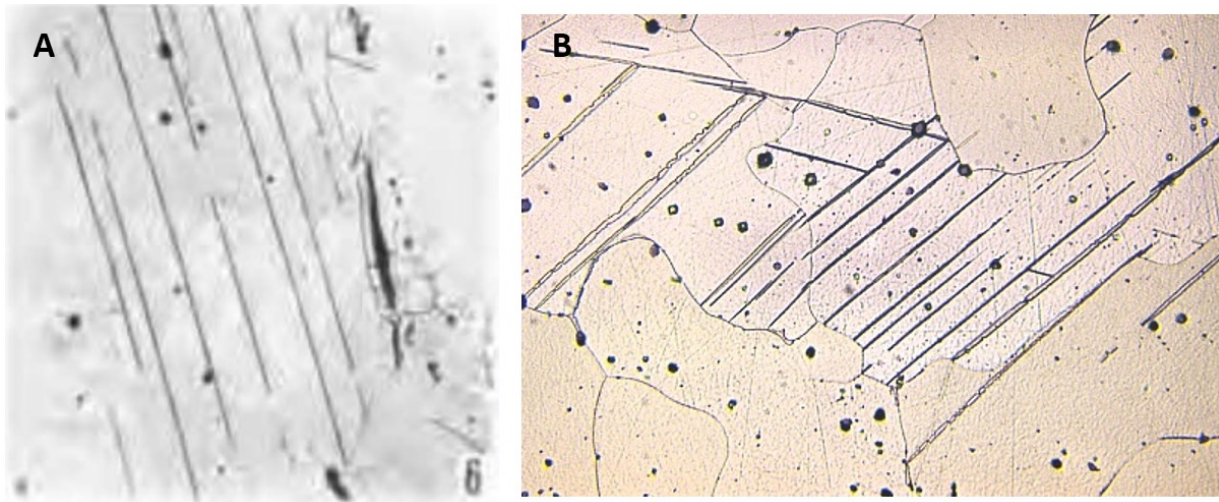


Figure 3.1: Micrographs of Neumann bands A) in an iron Celtic blade research by Pleiner [9] and B) a carbon ferritic sample by Langford [39].

Another technique to harden an iron sword is work hardening, which is simply working the metal. Work hardening is built upon the occurrence of plastic deformation in the material. It moves and creates dislocations within the crystal structure, which strengthens the material as it limits further plastic deformation. The use of cold-working techniques to shape and harden Celtic swords has been proven by the evidence of deformed ferrite grains and the presence of Neumann bands [9], [31]. Neumann bands, visible in Figure 3.1, are narrow parallel linear bands that can be identified as deformation microtwins in the (bcc) ferrite phase and only develop by shock deformation or cold-working [40], [41]. They recrystallize during annealing and thus can only indicate cold working if it was the last alteration [42]. In previous research on iron tyres from an Iron Age wagon-grave, Neumann bands were found only in the bent part of the tyre samples [42].

A theory was developed to date steel samples based on their Vickers hardness. It is said that ageing causes structural evolution, which leads to change in physical and mechanical properties [43]. The method described by Jiménez et al. [43], measures the Vickers hardness in pearlitic and ferritic grains/zones separately. The Vickers hardness is converted to Brinell hardness and then to mechanical strength. The linear correlation found between the age and the mechanical strength of pearlite phases and ferrite phases is as follows [43]:

$$\text{Pearlite phase : } Y(\text{mechanical strength MPa}) = -0.0066 * X(\text{age in years}) + 409.77 \quad (3.1)$$

$$\text{Pearlite phase : } Y(\text{mechanical strength MPa}) = -0.0159 * X(\text{age in years}) + 820.57 \quad (3.2)$$

For this theory to work the Heythuysen sample should show a Vickers hardness between 118 HV and 121 HV in ferritic zones and a hardness around 227 HV in pearlitic zones to match an age between 2500 and 3000 year old. The older the sample, the less precise this theory becomes. Initially, this theory was developed in research on the storage of nuclear materials [44]–[46].

3.1.2. Gangue Elements from the Iron Ore: Phosphorous

Some elements in the iron ore, such as calcium, magnesium and manganese, replace the iron in the slag, increasing the yield of iron production; Other elements, such as arsenic, phosphorous and sulphur (also) enter the iron lattice [23]. Sulphur is often removed before iron production by means of roasting [23]. Even though phosphorous predominantly enters the slag phase, it also affects the properties and workability of iron by diffusion into the metal structure.

Phosphorus exists naturally in bog iron ore, an ore found in bog/swamp grounds, alongside manganese and arsenic [23]. Research has found that phosphorus in the elemental composition of Celtic (mostly Late Iron Age) is a recurring phenomenon [9], [31]. Therefore, the presence of phosphorous in our swords of interest should not be surprising. A characteristic feature of phosphoric iron is its high hardness and extreme brittleness, which entails low toughness and ductility [47]. These properties make cold-working on phosphoric iron near to impossible. Iron with an elevated concentration of phosphorus can compete in hardness with unquenched ca. 0.6 wt% carbon steel, but the steel is less brittle and thus more desirable [9]. Moreover, the eutectic melting point of phosphoric iron is 1048°C, which is significantly lower than the melting point of pure iron. This could enhance the welding process at temperatures between 1000 and 1200 °C [31], [47]. However, above the phosphorus content of 2.8 wt%, a molten phase develops between the grain boundaries, due to segregation [47]. This phenomenon makes forging impossible [47].

Whether or not phosphoric iron is used deliberately by Iron Age smiths is still uncertain. Two arguments can speak for the targeted use of phosphoric iron. Firstly, phosphoric iron can easily be distinguished from non-phosphoric iron or steel, empirically or with the naked eye [9], [47]. Secondly, several metallographic examinations of Late Iron Age Celtic swords have shown a microstructure with alternating piling of phosphoric and non-phosphoric iron [9], [31]. On the contrary, some researchers doubt the intentional use of phosphoric iron. For example, Thiele [47] refutes the intentional use of phosphoric iron by sketching a scenario with a lack of non-phosphoric iron or the use of unsorted scrap iron. In addition, Lang [31] substantiates that phosphoric iron is less/not affected by carburisation as carbon absorption is inhibited by phosphorus. Therefore, it might be that a smith would only discover the presence of phosphorus in the iron after carburisation.

3.2. Microstructural Features

Studies have indicated that the microstructure and carbon content of wrought iron are highly inhomogeneous with a high probability of containing slag inclusions [25], [31]. On the other hand, the ferrite structure of wrought iron is said to consist of regular-shaped rough polyhedral grain structure due to annealed conditions or hot-working and recrystallization; Elongated-shaped grains with irregular sizes would be the result of cold-working [22]. Additionally, ghost bands are detected in Celtic swords due to localized concentrations of phosphorus or oxygen [31].

The best reference study for the swords of interest is the examination of a Hallstatt sword from France by J. Lang [31]. This Hallstatt sword was most probably made from one bloom without any form of piling. In addition, it is inhomogeneously carbonized up to half of its thickness, such that the inner half is predominantly ferritic with slag inclusions. Also, the grain size is generally small, reaching a minimum at the cutting edge and the surface. Lang concluded that the sword must have been heated and worked at an austenitic range (> 800°C) and then air cooled.

It is common to find microstructural differences within one object, as segments of an object often practice different functions [48], [49]. For example, a distinct difference in microstructure between the heel and the blade of an iron Roman cleaver (200 CE) [48]. Figure 3.2 shows the microstructure of the heel on the left side, consisting mainly of ferrite, slag strings and bands of fine pearlite and the microstructure of

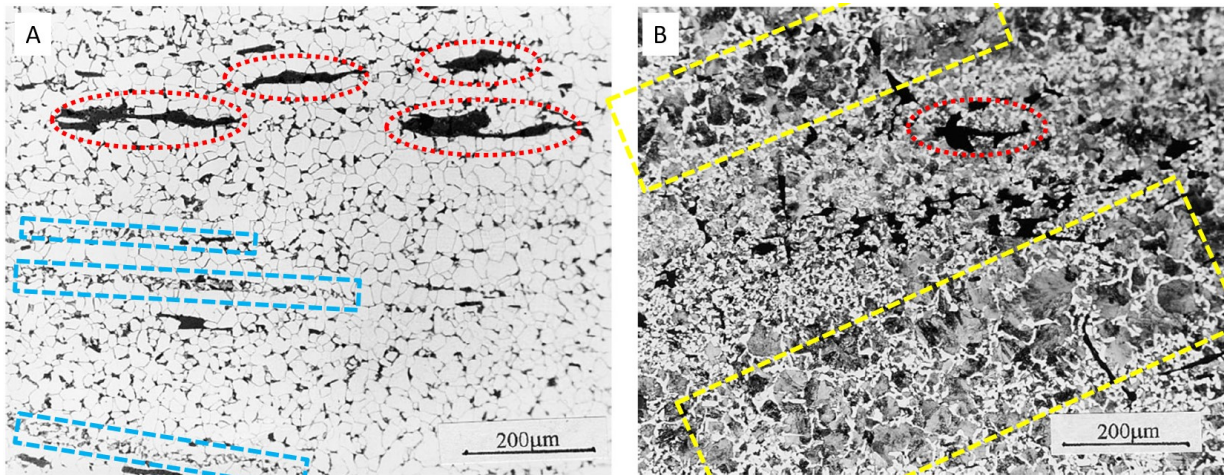


Figure 3.2: The microstructure of an iron Roman cleaver (200 CE) A) the heel of the cleaver and B) the blade of the cleaver. The red circles indicate slag inclusions, the blue boxes indicate bands of fine pearlite and the yellow boxes show broad bands of coarse grains of pearlite. Images retrieved from [48].

the blade on the right side, which shows bands of coarser grains and fine pearlite, indicative of a higher concentration of carbon [48].

Other examples of the heterogeneity within an ancient sword are the six Roman swords examined by Lang [37]. Figure 3.3 shows a graphical illustration of the phase composition in the cross-sections of the sword. The first three swords (Mansion House, Thames and Hod Hill) were constructed of carburised bloomery iron, show different degrees of piling and have a minimal change in hardness between the central rib and the cutting edge [37]. The swords Tiberius, Fulham and Chichester have a higher carbon content and were hardened by quenching [37]. The Tiberius sword was sandwiched between two strips of carburised iron, while the Fulham and Chichester swords show little evidence of being welded from strips [37]. Quenching may not be the general approach used by Hallstatt culture swordsmiths from the Early Iron Age, but it is occasionally used as there are examples of martensitic iron objects from this era and the next [9], [31], [48].

In 2006 Bravo Muños used the term "old pearlite" for the first time to name a pearlitic morphology with so-called "prismatic idiomorphous cementite layers" that present themselves in ancient carbon steels [44], [45]. Idiomorphous implies that a phase nucleates within a grain at heterogeneous nucleation sites and reflects the original crystalline form of the mother grain [50]. Figure 3.4 shows three different cases of old pearlite. The main characteristic of old pearlite is the presence of fragmented cementite films [45]. Bravo Muños explains old pearlite as a result of a very slow diffusion process of carbon, in his words "*the solubility of carbon in ferrite*". When an iron object ages over 3,000 years, this very slow diffusion process becomes observable. Moreover, it is claimed that the orderly idiomorphous behaviour of the cementite can be distinguished in colonies and becomes increasingly conspicuous for older iron, see Figure 3.4A [45]. In the research of García the microstructure of a nail from the 1st century BCE (Roman Empire) is identified as old pearlite, here the colony of parallel cementite is described as a Widmanstätten-type orientation of the crystal, as seen in Figure 3.4B [44], [46]. Figure 3.4C presents another structure identified as old pearlite, here large cementite needles are observed inside the pearlite grain alongside the fragmented cementite films. Figure 3.4D, shows a case of Pre-roman steel from Spain with a slightly different structure. Ferrite grains with idiomorphic carbides in the shape of needles [51]. This observation is explained by the slow crystal growth of carbides in ferrite, with kinetic behaviour favouring Widmanstätten needles, leading to the full exhaustion of the carbon supersaturating the ferrite phase [51].

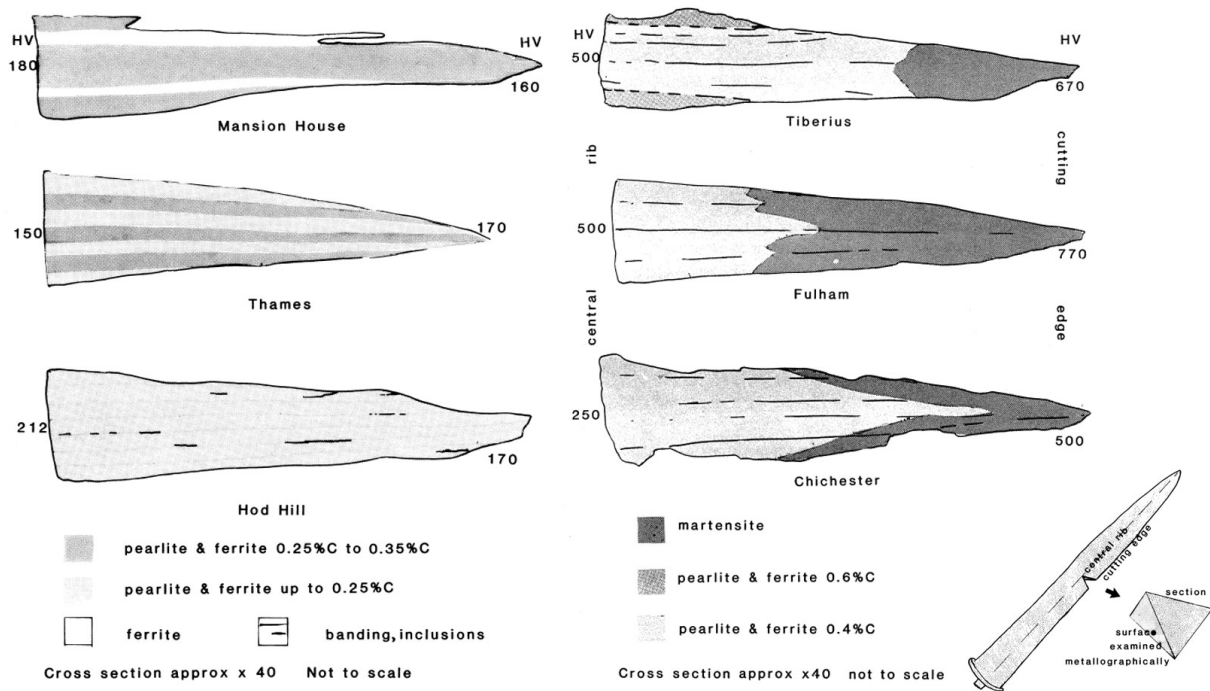


Figure 3.3: A graphical illustration of the phases present in the cross-section of six Roman swords (first century). The cross-sections are taken according to the schematic illustration in the right lower corner. Illustration retrieved from [37].

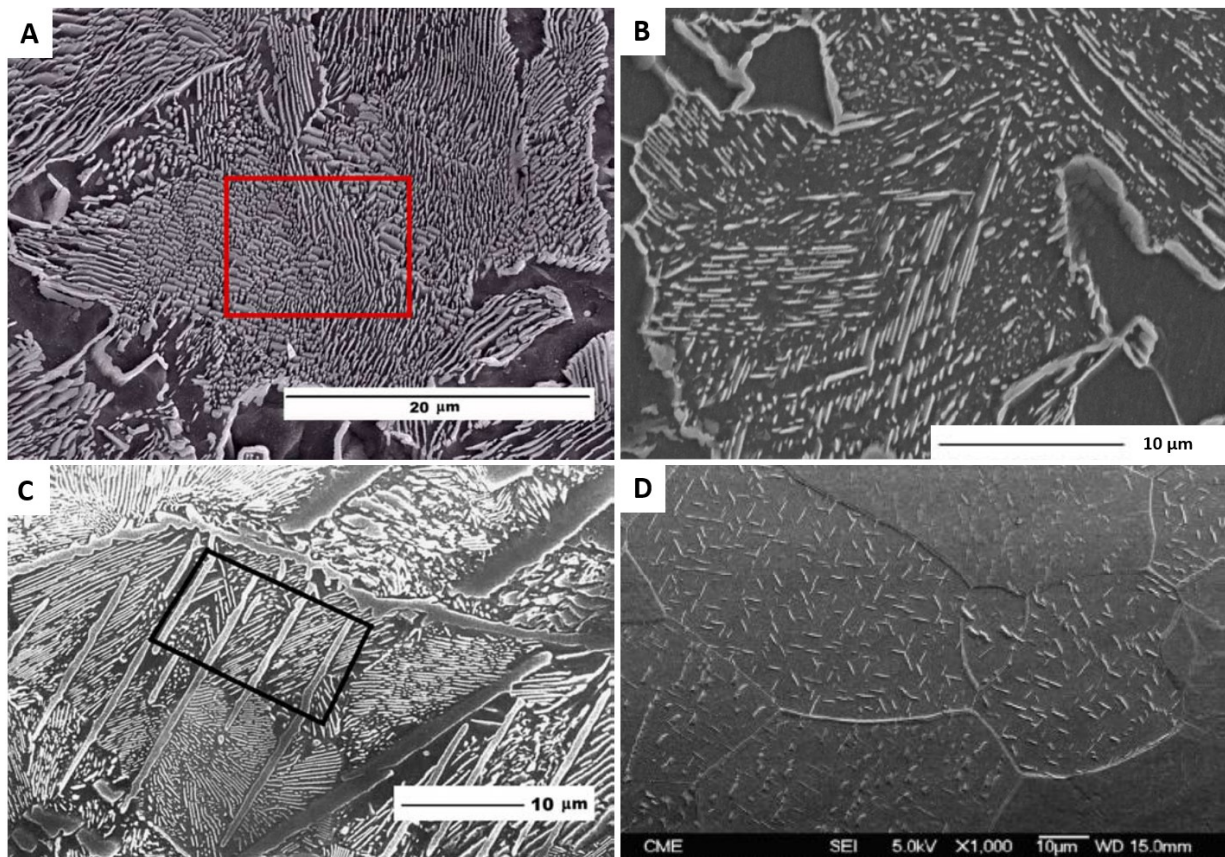


Figure 3.4: Old pearlite and cementite needle found in A) a nail from a Roman cistern (100 BCE) [44] B) a Roman nail [45] (100 BCE- 100CE) C) a Roman nail (500 CE) [45] D) Pilum Iberian (pre-roman) [51].

3.2.1. Fundamental Phases

The literature presents several phases that are observed in ancient iron objects. To create a better understanding of these phases, some fundamentals of the transformation and structure are introduced in this section.

Pearlite

The transformation of pearlite is a reconstructive process, requiring the diffusion of all atoms during nucleation and growth [50]. It is formed by the cooperative growth of ferrite and cementite from austenite grain boundaries [50]. Figure 3.5A shows a schematic illustration of pearlite growth. Pearlite has an average chemical composition similar to austenite and thus entire austenite regions can transform into pearlite. Colonies of parallel cementite films with similar interlamellar spacing exist within a pearlite region, due to cooperative growth from various fronts [50]. Figure 3.5B shows an example of pearlite colonies. One such colony represents a crystallographic grain with a rather homogenous crystallographic orientation [52]. Reduction of the interlamellar spacing increases the strength of the phase [52]. When pearlite is heat-treated below the austenitization temperature (± 700 °C) the films transform into spheres, minimizing the interfacial energy and thus reducing the hardness [53], [54]. This treatment is called spheroidisation and is driven by the interfacial area, therefore fine pearlite with narrow interlamellar spacing will spheroidise more rapidly than coarse pearlite with wide interlamellar spacing [53].

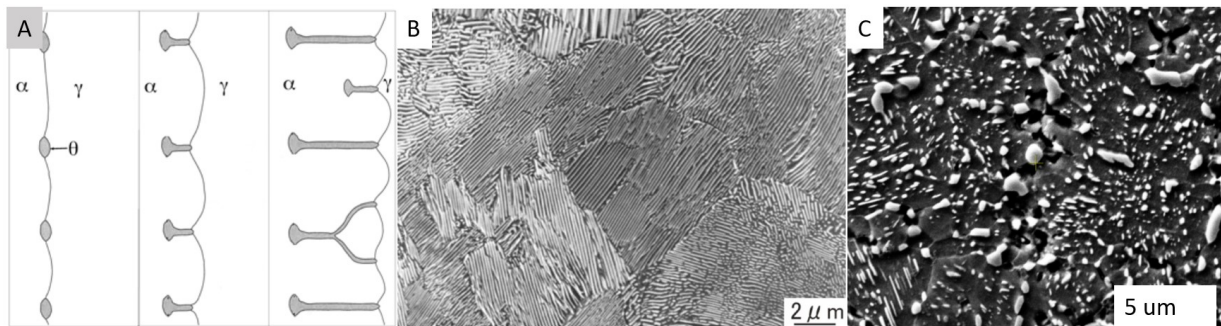


Figure 3.5: Examples from the literature regarding pearlite A) nucleation/growth [52], B) colonies [52] and C) spheroidisation [53].

Allotriomorphic Ferrite

The transformation of allotriomorphic ferrite is also a reconstructive process which means that the transformation is not restricted to the grain in which it nucleates [50]. Figure 3.6A shows a schematic illustration of allotriomorphic ferrite nucleation at the austenite grain boundary. Allotriomorphic ferrite has a shape which does not reflect the internal crystallographic symmetry but is formed along the austenite grain boundaries due to rapid growth along the austenite grain surface [50]. The ferrite grains will broaden into the adjacent austenite grains. Figure 3.6B shows broadened allotriomorphic ferrite within a pearlite matrix. The lower the carbon concentration the more space the allotriomorphic ferrite can claim, and the remaining austenite will transform into pearlite, see Figure 3.6C.

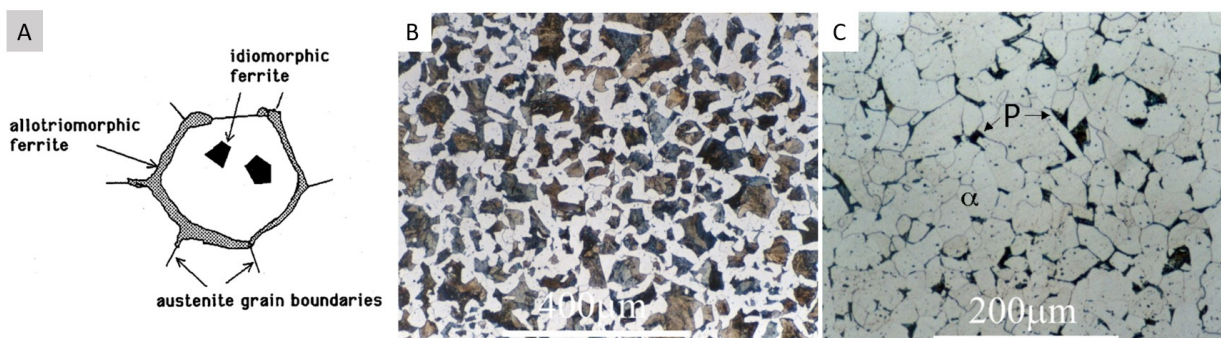


Figure 3.6: Examples from the literature regarding allotriomorphic ferrite A) schematic illustration, B) broadened and C) almost no pearlite after intense broadening. Retrieved from [52].

Widmanstätten Ferrite

The transformation of Widmanstätten ferrite is a paraequilibrium as the transformation is a displacive mechanism, meaning overall shape deformation and no iron diffusion, but the diffusion of carbon controls the transformation rate [50]. Figure 3.7A shows a schematic illustration of primary and secondary Widmanstätten ferrite nucleation in an austenite grain. Figure 3.7B, shows an optical microscopy example of a high concentration of Widmanstätten in the pearlite matrix.

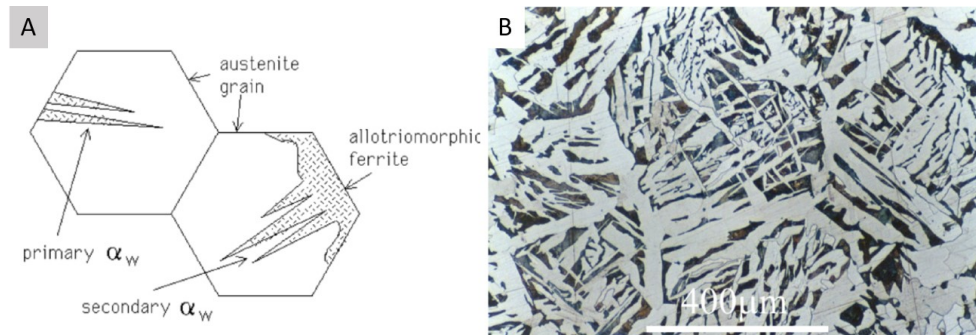


Figure 3.7: Examples from the literature regarding Widmanstätten ferrite A) a schematic illustration and B) an optical microscopy example. Retrieved from [52].

3.2.2. Slag

Slag inclusions are leftover slag entrapped in iron; They can occur in various shapes, sizes and compositions. Slag is an unavoidable byproduct of iron production and new slag scarcely enters the iron during forging and welding. Therefore, slag is often present since the beginning of the iron production and can provide information about the original production process. The characteristics of slag inclusions are mainly caused by the temperature of ancient furnaces and the composition of the ore [35]. Forging and welding can alter the shape and size of the slag, moreover, the composition could be slightly influenced. Due to hot forging, the slag inclusions are plastically deformed coherently with the shaping of the metallic matrix, resulting in elongated slag inclusions in the direction of maximum forging deformation [25], [55]. Another study describes the slag inclusions as fibres or strings that extend in the rolling direction and thus orientate either parallel to the surface in the form of long lines or perpendicular to the surface with the appearance of streaks or dots, depending on the cross-section, see figure 3.8 [9], [22], [31]. Slag inclusions can potentially account for 1-3 wt% of the total wrought iron [22].

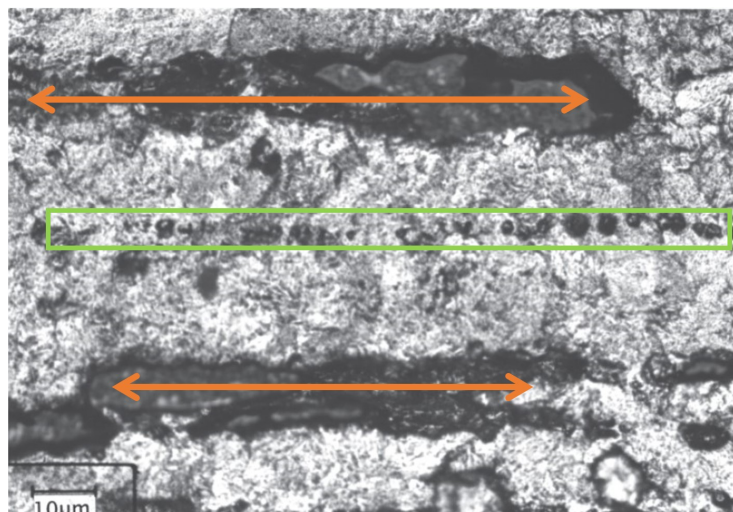


Figure 3.8: Slag inclusions in wrought iron. Orange arrows) slag strings parallel to the surface and green box) slag strings perpendicular to the surface. SEM image retrieved from [22]

Most of the time, slag displays glassy features. The main minerals found in slag inclusions are; Olivine, which is a combination of fayalite (Fe_2SiO_4) and forsterite (Mg_2SiO_4); Wüstite, which is a relatively pure iron oxide (FeO) and glass, which is a silicon oxide that can absorb several elements (Na, K, Mg, Al, etc.). Figure 3.9 shows a table with the distribution of oxides between the slag minerals [23]. It is seen that fayalite presents itself often in a 60-70:20-30 ratio of $\text{FeO}:\text{SiO}_2$ in wt% and that wüstite is relatively pure with a FeO concentration above 90 wt% [23].

	Olivine	Wüstite	Glass	Fe^0
SiO_2	X	-	X	-
TiO_2	-	x	X	-
Al_2O_3	-	-	X	-
FeO	X	X	X	X
MnO	X	x	X	-
MgO	X	-	X	-
CaO	X	-	X	-
K_2O	-	-	X	-
Na_2O	-	-	X	-
P_2O_5	X	-	X	-

X: present in major amounts, x: present in minor amounts; X: occasionally present; -: absent.

Figure 3.9: Distribution of oxides between the slag minerals. Note: these are the major oxides measured by SEM-EDS or EPMA, other forms/combinations of (hydr)oxides can exist in slag. Retrieved from [23].

Slag inclusions in ancient iron objects can be categorised into two groups, according to Buchwald and Wivel [35]. Firstly, there are bulky FeO -rich slag inclusions consisting of two phases, glass and wüstite or fayalite, which are generally localised in ferritic areas. This type of slag is correlated with a low furnace temperature, which restricts CO/CO_2 as a reducing agent causing the metal phase to be almost carbon-free and slag to become FeO -rich. Visually this group can be separated in two since the relatively large bubble shapes of wüstite are easily distinguished from the laths or lamina shapes of fayalite as can be seen in Figure 3.10A and B. The second group consists of elongated stings of SiO_2 -rich glass inclusions, which primarily consist of glass and are generally localised in pearlitic zones, see Figure 3.10C. This type of slag is correlated with a high furnace temperature, which enhances CO/CO_2 as a reducing agent causing the metal phase to absorb carbon (become pearlitic) and the slag to become FeO -poor.

More oxides such as MnO , K_2O , Al_2O_3 , CaO , MgO , P_2O_5 and TiO_2 can also be found within the slag inclusion, originating from the iron ore or coal ashes [35]. These oxides, together with SiO_2 , can be identified as Non-Reduced Compounds (NRC) when they are characteristic of the iron production stage and have a constant ratio [56]. When the NRC ratios vary, it is often the result of phase partitioning during the processing stage or the use of additives during the forging stage [56]. The different ratios of these oxides in one object can help determine the number of iron bars used with the piling technique.

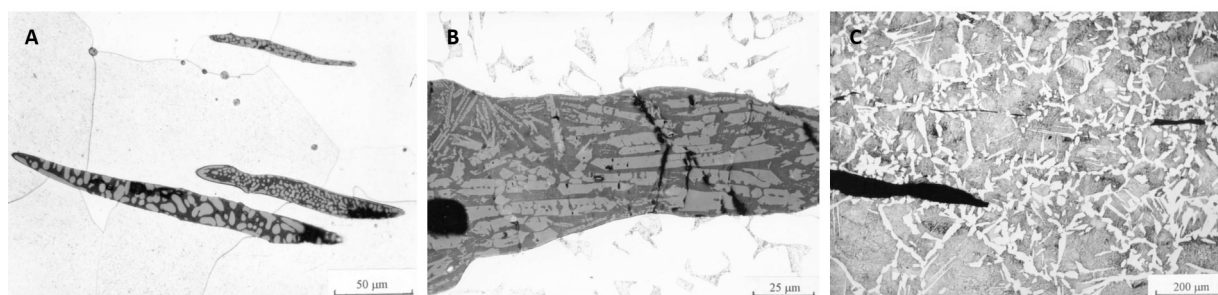


Figure 3.10: Different types of Slags A) glass-wüstite in ferritic iron (1850 CE), B) glass-fayalite in ferritic-pearlitic iron (980 CE), C) glass in pearlitic-ferritic iron (980 CE). Retrieved from [35].

Part II

Methodology

Experimental Procedure

4.1. Sample Selection and Construction

In archaeometallurgy, suitable specimens are often restricted by museum regulations and historical value. Mock-up samples increase research opportunities as they provide controlled conditions and plenty of specimens. This chapter discusses the museum samples and the smithing of a replica.

4.1.1. Museum Samples

As discussed in Section 2.1, the swords of interest are properties of the RMO and the Valkhof Museum and have archaeological and historical value. The sword of Oss is a centrepiece of the RMO's museum collection and was displayed in the exhibition: "De Vorst van Oss & Tijdgenoten: Elite in de IJzertijd" (*The Chieftain of Oss & Contemporaries: Elite of the Iron Age*) at the Museum Jan Cunen in Oss during the length of this research. Therefore, the sword of Oss is not available for metallurgical research.

The Heythuysen sword, see in Figure 4.1A, is not a (current) exhibition piece, has not undergone extensive conservation/restoration treatments and has a lower estimated historical value compared to the other swords. The RMO authorized the RCE to use non-invasive techniques on all pieces of the sword and to take one cross-section sample. The specimens from the Heythuysen sword are referred to as the **H-series**.

The sword of Wijchen, seen in Figure 4.1B, is a centrepiece of the Valkhof Museum's collection but is not exhibited during this research. The Valkhof Museum allowed the RCE to use non-invasive neutron diffraction on the most stable part of the restored sword, marked in red in Figure 4.1B. Before conservation and restoration work, a fragment of the sword was taken for research purposes (Figure 4.1). The specimens from the sword of Wijchen are referred to as the **W-series**.

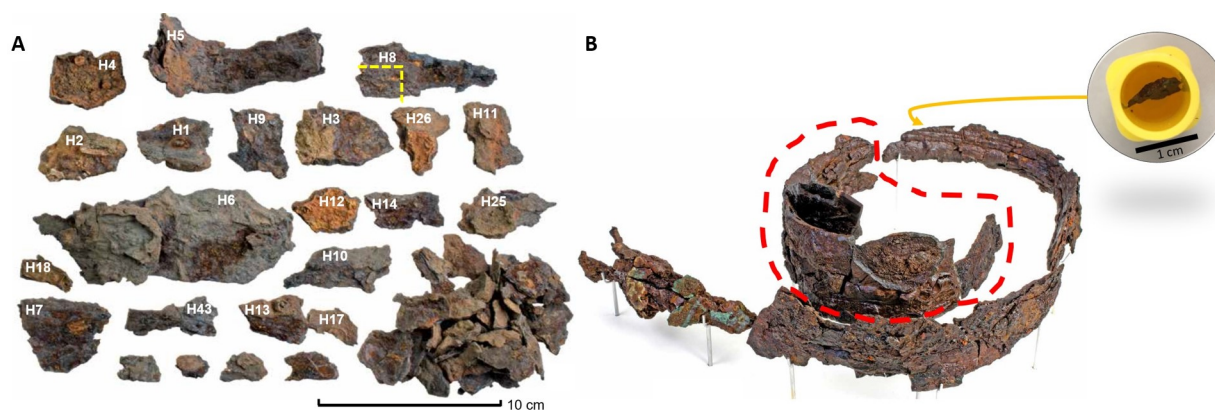


Figure 4.1: A) The labelled Heythuysen pieces. The yellow dashed line indicated the cross-section cut. B) Selected pieces of the Wijchen sword. Piece W-1 is circled red and specimen W-2 is in the yellow tube.

4.1.2. Smithing of a Replica

Creating a replica with similar metallurgical characteristics as the swords of interest is challenging. The swords of interest have aged for about 3000 years and the hypothetical production process is based on historical research. Previous attempts to create metallurgical replicas stated that modern commercial construction steels (0.1-0.2% Carbon) were unsuitable [9]. Furthermore, although artificial ageing is a modern technique for reducing ductility and increasing the strength and hardness of steel [57], it has not been proven to correctly artificially age an object for thousands of years. This chapter describes the creation of the mock-up sword for this research, which specimens will be referred to as the **M-series**.

Step 1: Selection of Material

The opportunity arose to use an old iron anchorage from the Domtoren in Utrecht. In 2019, a major, five-year restoration project began, encompassing the entire tower. In this project, the original wrought iron anchorages from the pillars of the lantern (upper part of the tower) were removed. The anchors can be seen as large staples that secure the blocks together. There is a strong possibility that the anchorages date from the 14th century, as the Domtoren was completed in 1382 after sixty years of construction. However, it is documented that the first restoration project took place in 1519, that a five-year renovation in 1836 was required to ensure that the tower did not collapse and that the first major restoration project took place from 1901 to 1930, which included the lantern [58]. So the next best possibility is that the anchorages date back to the early 20th century. Even if the anchors are from the early 20th century, they are most likely still made of wrought iron as described in section 2.2.1, and are the oldest iron we could use. Based on this it was decided to use the anchors to make the sword replica. More specifically, the anchorages used were salvaged from the east side of the lantern. Specimens of the Domtoren anchorages are referred to as the **D-series**.

Step 2: Selection of the Forging Method

The next challenge is to create this replica. As described in Section 2.2.2, forging a sword is a time-consuming process that requires expertise. Thijs van de Manakker was so kind to help create the mock-up sword. He is an old-fashioned blacksmith with over fifty years of blacksmithing experience and a passion for the Celtic style. Over the course of his career, he experimented with prehistoric iron production by recreating the clay furnaces. In addition, he created several replicas of the sword of Oss, both bent and not bent. For one of the replicas, he was asked to bend a sword using only prehistoric tools. He built a low and long furnace with bellows made of wood and leather to heat as much of the length of the blade at once. Figure 4.2, is a picture of the furnace and the replica created by van de Manakker. First, the tip of the blade was heated to an orange-yellow heat colour and then immediately bent around a tree trunk using leverage. This process continued until the entire sword was bent. Meanwhile, the hilt itself was protected from the heat of the furnace with damp cloths. The replica used for this bending experiment was forged from modern structural steel S235 (or steel 37) and C45. S235 is commonly used by modern blacksmiths and can contain up to 0.22 wt% carbon; C45 is a malleable steel with 0.45 wt% carbon. This experiment was a success.



Figure 4.2: Furnace designed by Thijs van de Manakker for bending the replica of the sword of Oss. Photo by Thijs van de Manakker.

Step 3: Forging of the Mock-up sword

After the material and skills are found, the mock-up sword must be created. Van de Manakker starts with two small tests to assess the Domtoren iron. Figure 4.3, shows the anchors before treatment, including the results of the two tests. First, the part of the lead casting is cut off. Visual analysis of the anchor cross-section shows a cross-width meandering slag inclusion most likely caused by piling (Figure 4.3C). A slag inclusion caused by piling is often nonlinear due to the heterogeneous working and hammering of the material. Secondly, a hard hammer blow on the cold anchor shows ductile behaviour as the anchor bents. The two layers seen in the cross-section break apart along the entire length of the anchor, confirming the presence of poor piling (Figure 4.3D). From experience, van de Manakker guesses that this is iron from bog iron ore with a high concentration of phosphorus in the elemental composition. According to van de Manakker, phosphorus would have made the iron so brittle that it would not have survived this hammer blow.



Figure 4.3: A and B) The anchors from the Domtoren. C) The cross-section of the anchor with a long slag inclusion running through the length. D) The bent tip of the anchor shows the split of the two piling layers.



Figure 4.4: A) The blacksmith's fire. B) The mock-up sword before bending. C) Bending the cold sword with a leverage effect. D) Bending the reheated sword by hammering.

The forging of the mock-ups is similar to the process described in section 2.2.2. Figure 4.4A shows the coal-fueled blacksmith's fire. The Domtoren wrought iron was heated until it turned yellow-orange, about 1100/1200 °C. The forging started in the length of the blade towards the tip and then in the width towards the hilt. The anchor is forged into a bar of the same dimensions as the sword of Oss (33 mm wide and 8

mm thick) and then the shape of a sword is created including a midrib. The mock-up is cooled by summer air. Finishing the mock-up sword is accelerated by electrically grinding the edges sharp and creating a neat tip.

Experimental bending of the mock-up is done using two methods as seen in Figures 4.4C and D. One part of the mock-up is bent by brute force in cold conditions with a leverage effect (Figure 4.4C). The other part is reheated to a light cherry/orange-red colour (approximately 870-1090 °C) and hammered until the desired angle is achieved (Figure 4.4D). The remaining part of the sword is not bent and serves as a control sample for the bending techniques.

4.2. Experimental Materials and Techniques

In this chapter, the experimental materials are listed and described in detail, including the sample preparation. Subsequently, the experimental techniques are explained step by step.

4.2.1. Materials

Table 4.1 presents a list of specimens. The specimens are divided into the following series, see Figure 4.5.

- **The H-series** are all parts of the Heythuysen sword, selected for their size, preferably large enough to have a bulk of not corroded iron, and for their shape, a variation in bends. Specimen H-CS-8 is the cross-section of Heythuysen's sword, which was made and embedded in a preceding project (by Vanessa Fontana) and is reused in this project. The cross-section covers the hypothetical rib up to the cutting edge.
- **The W-series** are pieces of the Wijchen sword, as discussed and shown in Section 4.1.1.
- **The D-series** are samples taken from the anchorages of the Domtoren before the mock-up sword was forged.
- **The M-series** are samples taken from the mock-up sword described in Section 4.1.2. Three cross-section samples are cut from the mock-up: one from the hot-bent part, one from the cold-bent part and one from a straight part. Within the cross-sections, a distinction is made between the rib (middle part) and the cutting edges (outer parts) of the sword. For user convenience, these specimens are sandwiched between metal clams before treatment.

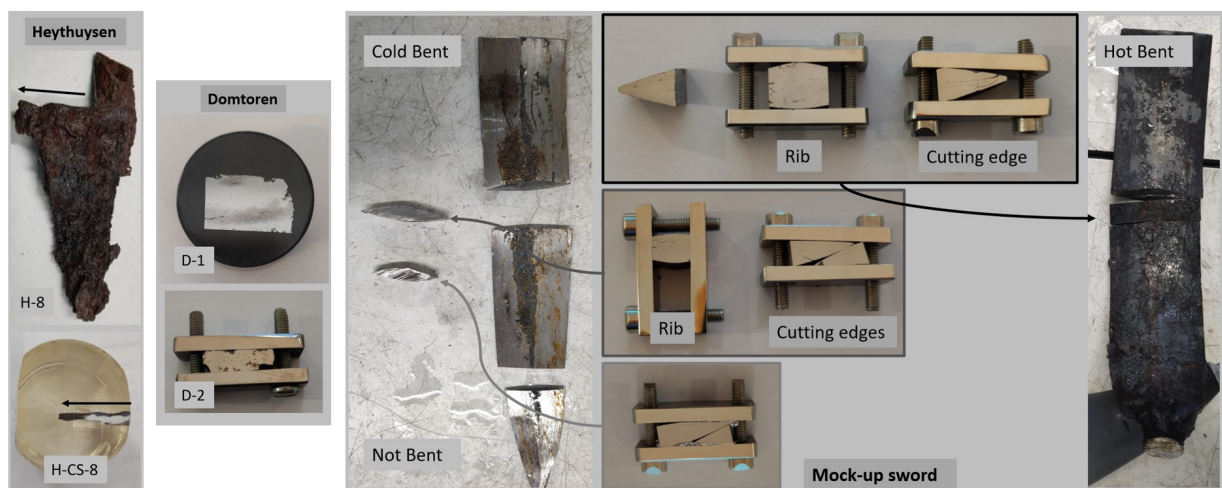


Figure 4.5: All specimens in this thesis, the Heythuysen series, the Domtoren series and the Mock-up sword series.

4.2.2. Techniques

Step 1: Electron Backscatter Diffraction

First, all specimens selected for electron backscatter diffraction (EBSD) measurements are ground and polished up to oxide polishing suspension (OPS) 0.25 μm . EBSD is done first due to the time-schedule of the measurements abroad. OPS is a sufficient polish to enhance the Kikuchi lines and enable successful

electron backscatter diffraction (EBSD) measurements. EBSD can provide microstructural information such as crystallographic orientation, grain boundary orientation, misorientation, preferred orientation and texture. The EBSD measurements were carried out using a Helios G4 PFIB UXe at TU Delft with a step-size of 1, 2 or 5 μm to determine the grain size distribution, crystallographic orientation (IPF), misorientation angles and the Kernel Average Misorientation (KAM). The latter analysis reveals local misorientation that may indicate local deformation, dislocation density, local lattice distortion and residual stresses [59]. Inverse pole figure (IPF) maps show the crystal axes normal to the plain of observation, using colour to indicate the crystallographic orientation.

Intermediate step: Time of Flight Neutron Diffraction

During this thesis, a non-invasive analysis was performed on the museum samples mentioned in section 4.1.1 to determine the phase fraction and defect distribution and intensity of the microstructure. This analysis, Time of Flight Neutron Diffraction (ToF-ND), was carried out at the INES station at the ISIS Neutron and Muon source in the UK. The correlation between the results of the non-invasive ToF-ND and the destructive SEM-EBSD would present an interesting comparison between techniques. Due to time and length limitations of this master thesis, the ToF-ND results are not presented and discussed in this report. In Appendix C and D the basic principle of this ToF-ND diffraction is explained and a first impression of the result is stated.

Step 2: Electron Probe Microanalysis

Secondly, based on EBSD measurements and the literature, electron probe microanalysis (EPMA) is performed to determine the carbon content within the specimen. EPMA is a technique that is used for elemental analysis, based on the elemental-specific X-ray wavelengths and is performed using a JEOL JXA 8900R microprobe at TU Delft with a wavelength dispersive spectrometry (WDS) beam current of 100 nA, a step-size of 15 μm and a spot size of 5 μm . To track the location of the EPMA measurements microhardness indentations are made. This was applied with a Vickers Hardness test, HV load of 0.025 kg (and 0.1 kg). Three indentations are made in the width of the samples, the rib and the edges separate.

Step 3: Optical Microscopy and Scanning Electron Microscopy

Subsequently, the samples are etched with 2% nital for 10-20 seconds as preparation for optical microscopy (OM) and Scanning electron microscopy (SEM). OM is performed on the Leica LMD7 and the Olympus Stereo SZX9 (TU Delft) to analyse the phase distribution on a macroscale. SEM is performed on both the JEOL JSM-IT700HR (RCE) and the JEOL JSM-IT 100 (TU Delft) to analyse the grain structure, phase distribution and defects such as cracks, voids and inclusions on higher magnification.

Step 4: Energy Dispersive X-ray Spectroscopy

Lastly, SEM-energy dispersive X-ray spectroscopy (EDS) is a semi-quantitative technique used to analyse the elemental composition of the slag inclusion within the specimen.

Specimen name	Source	Description	Part of Thesis*	ToF-ND
H-1, 5-7, 9-11, 13, 14, 16 and 28	Sword of Heythuysen	Archaeologically found pieces. No conservation/restoration treatments.	NO	YES
H-8	Sword of Heythuysen	Minus the cross-section	NO	YES
H-CS-8	Sword of Heythuysen	Cross-section taken from the H8 piece	YES	NO
W-1	Sword of Wijchen	Small chip before restoration	NO	YES
W-2	Sword of Wijchen	Large restored piece, glued with Uhu-Hart and coated with Paraloid B27	NO	YES
D-1	Domtoren original	From the exact same anchorage as the Mock-up	YES	NO
D-2	Domtoren original	Different anchorage	YES	NO
M-NB-rib	Mock-up	Not bent, rib area	YES	YES
M-NB-edge	Mock-up	Not bent, edge area	YES	YES
M-CB-rib	Mock-up	Cold bent, rib area	YES	YES
M-CB-edge	Mock-up	Cold bent, edge area	YES	YES
M-HB-rib	Mock-up	Hot bent, rib area	YES	YES
M-HB-edge	Mock-up	Hot bent, edge area	YES	YES

Table 4.1: List of all specimens. *Part of the Thesis are specimens that are analysed by SEM-(EBSD), EPMA, OM and SEM-(EDS).

Part III

Results and Discussion

Interpretation of the Results

The cross-section from the Heythuysen sword (H-CS-8) is the main specimen of this thesis. All other specimens, the D- and M-series, are used to assist in the analysis of the H-series. The D-series is the original state of the iron from which the M-series was made. The M-series is used to determine what microstructural differences occur when bent by brute force (cold) or blacksmithing techniques (hot). The results are summarised in the Tables of Appendix A. Several microstructures are observed in the specimen. In this thesis, we define the microstructures as follows:

- **Large α -Region:** This microstructure consists only of large ferrite grains with a diameter between 30-150 μm . Per specimen, the average diameter of this microstructure can vary. The presence of carbides within the ferrite grains is a possibility.
- **α -Region:** This microstructure consists only of small ferrite grains with a grain size between 10 and 30 μm . In this microstructure, cementite occupies the grain boundaries.
- **Small α -Region:** This microstructure consists of small ferrite grains and small pearlite grains. The grain size is smaller than 30 μm and varies per specimen. In some specimens, the cementite occupies the grain boundaries in this microstructure.
- **Pearlite Regions:** This microstructure consists of large pearlite grains and minimal ferrite grains. The pearlite grains can reach sizes of around 600 μm with multiple colonies/subgrains inside. The cementite features (i.e. degree of film fragmentation, interlamellar spacing and spheroidisation) inside the pearlite can differ per specimen.
- **α_w -Region:** This microstructure consists of coarse pearlite grains that are interrupted by allotriomorphic ferrite at the grain boundaries and Widmanstätten ferrite needles inside the pearlite grain. The degree of ferrite inside this microstructure can differ per specimen or even within a specimen. Also, the cementite features inside the pearlite grains can vary per specimen.

5.1. Results of the Heythuysen specimen: H-CS-8

The H-series has some general features that need to be noted. All pieces of the H-series are heavily corroded, meaning the entire surface is transformed into iron (hydr)oxides, leaving only a portion of the iron core suitable for metallurgical research. This will influence the perspective of H-CS-8 towards the M-series and literature.

5.1.1. Phases

Figure 5.1 shows a macrograph of the entire cross-section. Corrosion can be seen around the iron bulk and in some spots within the bulk, see lower-middle and -cutting edge. Investigation of the cross-section with OM from the rib to the cutting edge shows several phases:

- A Large α -Region with a grain size around 100 μm is observed in the centre of the rib. This region is marked with an orange circle on the lower rib area in Figure 5.1. This microstructure transitions into a Small α -Region towards the surfaces of the sword.
- A cloud of small slag inclusions interrupts the Large α Region. Thereafter, the grain size significantly decreased to around 15 μm and small pearlite grains were introduced, a Small α -Region. This is the bulk of specimen H-CS-8.

- Near the upper rib surface and the lower middle surface of H-CS-8, α_w -Regions are observed. A third α_w -Region dominates in the upper cutting edge area. These regions are marked with red circles in Figure 5.1.

This phase distribution can be roughly interpreted as a Large α -Region in the centre of the sword, a bulk of Small α -Regions and some α_w -Regions close to the surfaces of the sword.

A higher magnification micrograph of H-CS-8 is shown in Figure 5.2. The top half of the image is a Small α -Region and the bottom half is a α_w -Region. In the Small α -Region of this image, the ferrite and pearlite grains are individually visible. Throughout the bulk, the ratio of ferrite/pearlite grains in this region varies slightly. The α_w -Region shows the individual Widmanstätten ferrite needles and allotriomorphic ferrite grains around the larger grains. Figure 5.2 also shows some of the EPMA measuring lines and shows two types of slag inclusions (encircled yellow and blue). The slag inclusions are presented in the next section (Section 5.1.2).

SEM images of this specimen are shown in Figure 5.3. The Large α -Region contains no carbides. Figure 5.3A shows that a part of the Small α -Regions consists of small round ferrite grains and a minority of slightly smaller angular pearlite grains. In addition, some of the grain boundaries contain cementite and some of the ferrite grains contain small carbides. This is a localised image, other ferrite/pearlite grain ratios are seen throughout the bulk. Figure 5.3B shows part of the Large α -Region. Figures 5.3C and D show that the mother grains in the α_w -Regions is pearlite. Fragmented cementite films cover the grain in small zones of parallel orientation. The films near the grain boundaries are more densely packed than the fragmented film in the core of the grain, which in some places only seem to consist of tiny dots. The structure seems comparable to the old pearlite structure described in Section 3.2.

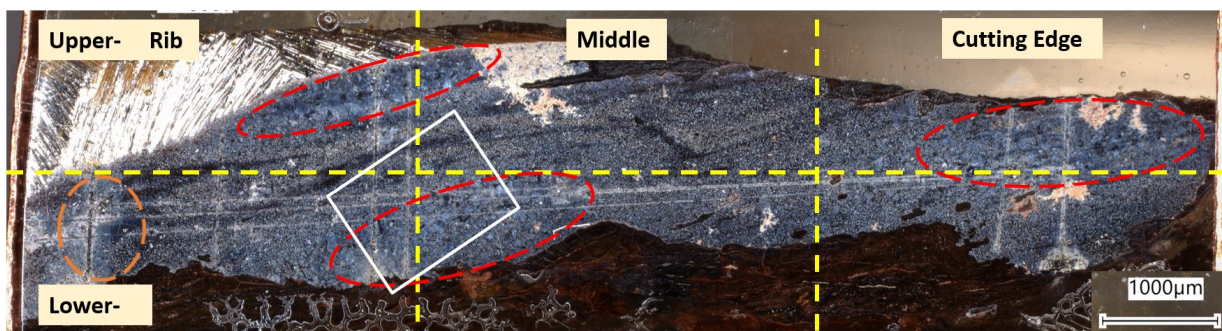


Figure 5.1: Marcograph of H-CS-8, dividing the specimen in Upper- and Lower- Rib, Middle and Cutting edge. The orange circle indicates a Large α -Region, the red circles indicate α_w -Regions. The white square is the location of Figure 5.2.



Figure 5.2: OM of H-CS-8, showing the Widmanstätten microstructure near the surface of the sword, ferrite and pearlite alternating grains, the measurement lines of the EPMA and two types of slag inclusions. (blue: glassy. Yellow: wüstite-glassy/fayalite)

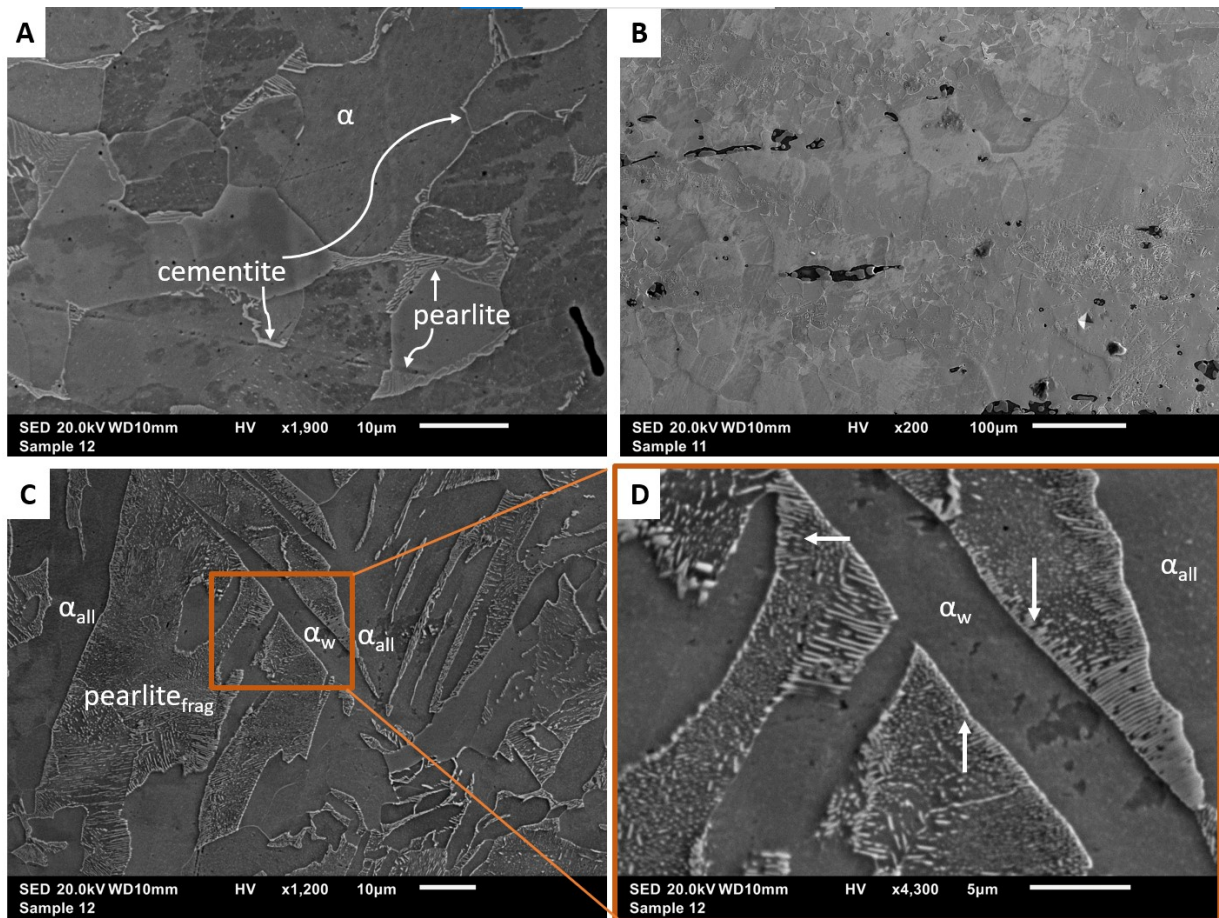


Figure 5.3: SEM images of H-CS-8 A) the Small α -Region and B,C,D) the α_w -Region.

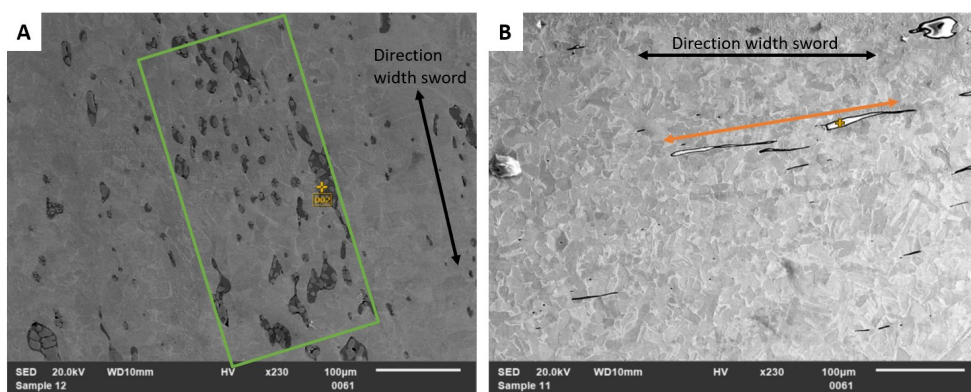


Figure 5.4: SEM image of two types of slag inclusions in specimen H-CS-8 A) a cloud of little wüstite-glass slag inclusions and B) strings of glass slag inclusions. The green box and orange arrow refer to the elongation direction, see Figure 3.8.

5.1.2. Slag Inclusions

There are numerous slag inclusions throughout the cross-section. The SEM-(EDS) shows remarkable differences in shape, size, distribution and composition. Figure 5.4 shows two types of slag inclusions seen in this specimen. SEM-EDS is used to determine the elemental composition of the different types of slag inclusions. The results are presented in Appendix B Table 1. Based on significant amounts of CaO present in the various types of inclusions, the NRC ratio of SiO_2/CaO is chosen to compare inclusions inside H-CS-8. All SiO_2/CaO ratios of H-CS-8 are plotted in Figure 5.5. The inclusions detected in H-CS-8 are visually divided into three categories:

- As seen in Figure 5.4A, there are relatively large groups of little strings and circular inclusions that are generally oriented parallel to the width of the sword. These groups are primarily located in the Small α -Regions. Among the larger inclusions in this group, two different grey tones can be seen in the shape of bubbles and a matrix, similar to the glass-wüstite FeO-rich inclusions described in Section 3.2.2 (see Figures 5.4A and 3.10A). In addition, this type of inclusion is also present in larger irregular shapes, often close to the group of smaller inclusions. These shapes have no particular orientation.

The inclusions with circular shapes in a matrix show extremely high and pure concentrations of FeO within the circles. The FeO concentration is over 94 wt% and the only other elements detected are MnO (<4 wt%) and C. These are valid numbers and shapes for wüstite. The matrix has a SiO_2 concentration around 10-30 wt%, a higher concentration of FeO (50-80 wt%) and significant concentrations of MnO (5-9 wt%) and CaO (<6 wt%). This is a more glass-like content that tends towards the composition of fayalite. The NRC ratio of SiO_2/CaO for this type of inclusion varies between three ratios 10.1, 3.9 and 2.4.

- As seen in Figure 5.4B, there are long strings that do not exist in large groups. The orientation of these inclusions is parallel to the width of the sword and SEM shows a content with a homogeneous tone. They are mainly present in the α_w -Regions. These inclusions are comparable to the glass SiO_2 -rich inclusions described in Section 3.2.2 (seen Figure 5.4B and 3.10C).

The content of this type of inclusion has a FeO concentration below 17 wt%, a high concentration of SiO_2 between 50 and 60 wt% and significant concentrations of CaO (12-22 wt%), MnO, K_2O , Al_2O_3 and MgO. These elemental features match an acceptable glassy inclusion. These inclusions have various ratios of SiO_2/FeO and have NRC ratios (SiO_2/CaO) that fall under the category of 3.9 and 2.4.

- SEM show that some of the strings have a very fine dot pattern inside. This type of inclusion is present in both Small α -Regions and α_w -Regions. They have some similar features to the homogeneous filled strings.

These inclusions have a substantial concentration of FeO (14-24 wt%), a relatively high concentration of SiO_2 (40-50 wt%) and significant concentrations of CaO (10-15 wt%), MnO (± 10), K_2O , Al_2O_3 and MgO. All these inclusions fall under the category of NRC ratio (SiO_2/CaO) 3.9.

The results of examining the H-CS-8 slag inclusions can be interpreted as follows. There are wüstite-fayalite inclusions with a distinction between the group of small inclusions and large irregular shapes, which is confirmed by the SiO_2/FeO ratio; There are glass inclusions with a distinction between two SiO_2/FeO and $\text{Al}_2\text{O}_3/\text{K}_2\text{O}$ ratios, and there are glassy fine pattern inclusions. The NRC ratios are not equal and thus suggest that the processing treatments influenced these inclusions or that at least three iron blooms were used with the piling technique to create the stock for forging a sword.

5.1.3. Carbon

EPMA measurements are performed to determine the concentration and location of carbon in the specimen. The EPMA results for this specimen show a rather erratic behaviour. Figure 5.6 shows a fraction of the results that is representative of the entire specimen. The α_w region has an average carbon concentration of 0.550 wt%, while the small α region has an average carbon concentration of 0.18 wt%; When a pearlite grain or a cementite boundary is (partially) in the measuring spot, the carbon concentration increases to 0.5-1 wt%. The EPMA measurement went through a corrosion-affected area around a pit in the bulk. This area has a carbon content between 1 and 2.5 wt%. The slag inclusions along the measuring path have a carbon concentration between 0.2 and 0.5 wt%, although this is expected to be close to zero.

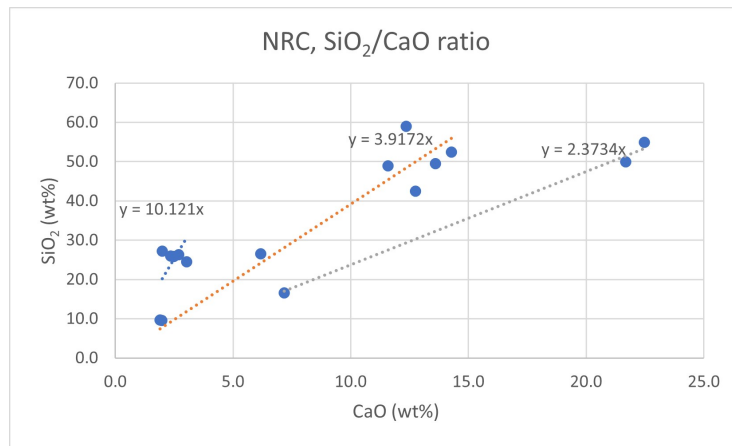


Figure 5.5: Three groups of SiO_2/CaO NRC ratios: 10.1, 3.9 and 2.4.

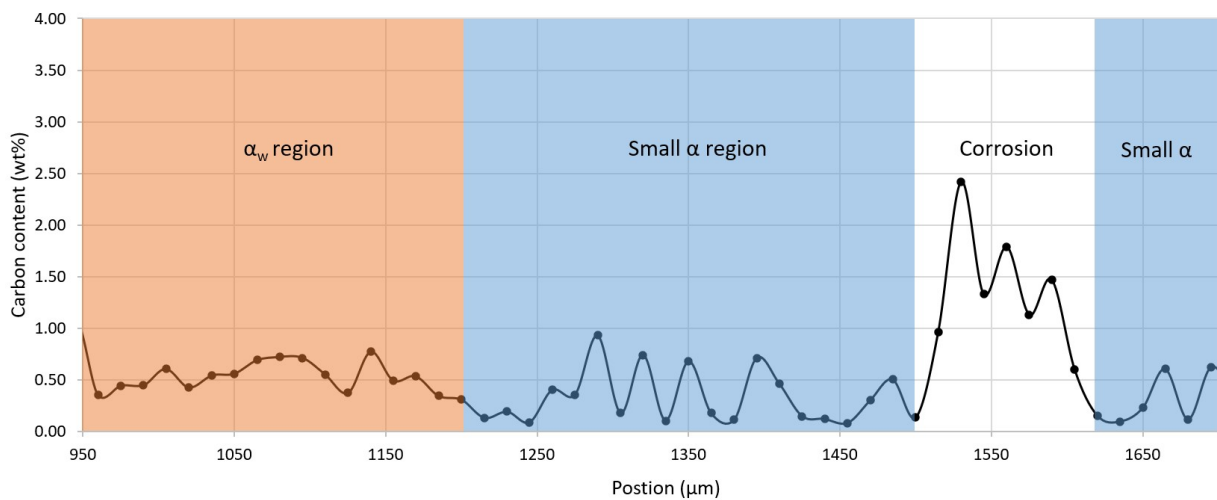


Figure 5.6: Part of the C content from the Heythuysen sword (H-CS-8). EPMA results.

The Vickers hardness measured from rib to edge is 151, 152 and 154 HV, respectively. The first indentation is made in the large α region and the other two are made in α_w regions.

5.1.4. Crystallographic Characterisation

The EBSD images of the cutting edge, middle and rib sections are shown in Figure 5.7, respectively. The top row presents image quality (IQ) maps overlapped with the inverse pole figure (IPF) analysis and the bottom row presents Kernel Average Misorientation (KAM) plots.

In Figure 5.7D, the outlines of a few large pearlite grains are visible through the blue-coloured allotriomorphic ferrite and the Widmanstätten ferrite around it (black arrows). The blue KAM colour correlates with a nihil amount of local misorientation. The fragmented pearlite grains are mainly green but have a significant amount of yellow and red spots, which correlates with a higher amount of local misorientation. The IQ+IPF image (Figure 5.7A), shows within these large grains many subgrains of multiple colours and tones (white arrows). Multiple colours correlate with multiple crystallographic orientations, which mostly correspond with distinctive subgrains; The subtle change in tone correlates with the different colonies of paralleled laminas. The ferrite grains, both allotriomorphic and Widmanstätten, are solid in colour and have no evidence of subgrains (black arrows). In general, the grains near the cutting edge appear to favor blue (111) crystallographic orientation slightly.

In the middle images (Figures 5.7B and E), the division between the α_w region and the small grain region can be clearly seen. The α_w region presents comparable results to those described for the near

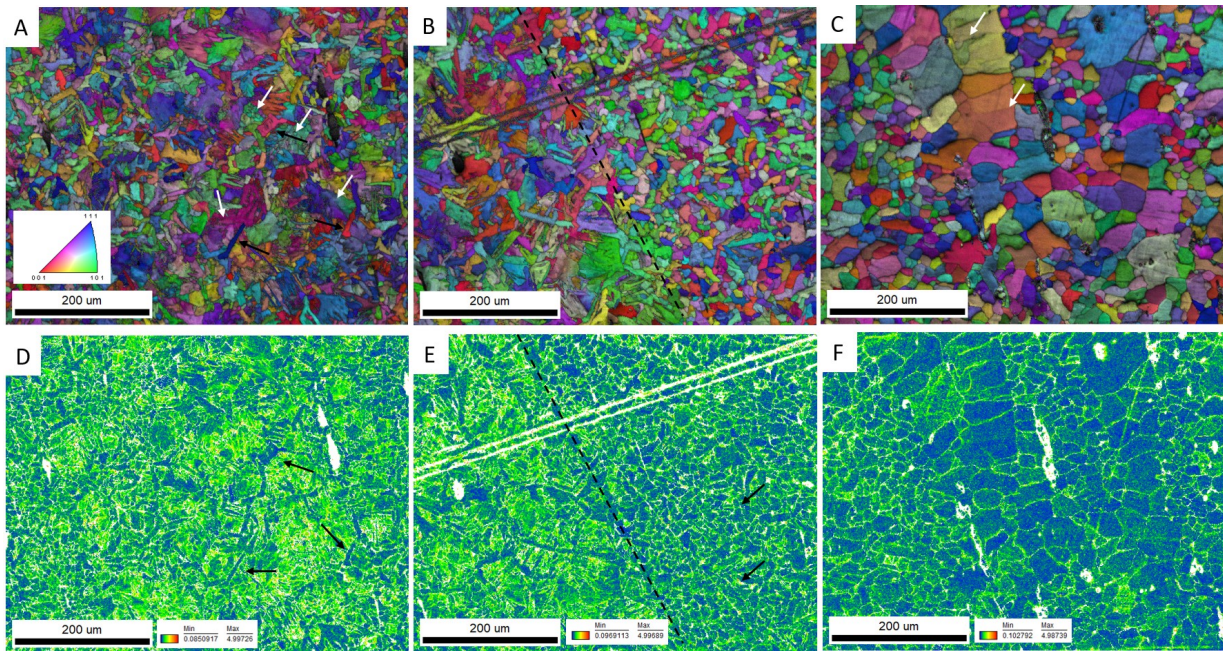


Figure 5.7: EBSD analysis on specimen H-CS-8, upper row are IPF +IQ images, lower row are KAM images. All images are acquired with a step size of $1 \mu m$. The locations: A and D) near the cutting edge (α_w region), B and E) in the middle of the sample (half small α region, half α_w region) and C and F) the rib of the sword (large α region, small α region)

cutting-edge section (Figure 5.7A and D). The small α region shows quite some green colours in the KAM image, mainly around the grain boundaries where slim pearlite grains are located (black arrows). In contrast to fragmented pearlite in the α_w region, only a few sporadic red or yellow spots can be seen here. In the transition area between the α_w region and the small α region, a slight preference for the green (101) crystallographic orientation is seen.

The rib (Figure 5.7C and F) shows large ferrite grains with traces of subgrains, indicated by the dark IQ lines in Figure 5.7C (see the white arrows). The large grains are entirely blue, indicating a negligible dislocation density. The grains do not favour a crystallographic orientation.

In general, specimen H-CS-8 has no dominant texture and the misorientation distribution is close to the McKanzie theory of random orientation for cubic crystals. Furthermore, the KAM plots show a correlation between the phase regions and the local misorientation. Throughout the cross-section, some contradicting results are seen per microstructure. Near the rib, where a Small α -Region is dominant, a central line of low local misorientation is observed. This central line of low local misorientation is not observed near the cutting edge, where α_w -Region influences the KAM values.

5.2. Results of the Domtoren specimens: D-1 and D-2

As previously mentioned, the D-series represents the original state of the Domtoren iron used to make the mock-up sword (M-series). The D-series consists of D-1 and D-2. D-1 is a cross-section of the exact anchoring used to make the mock-up. D-2 is a cross-section taken from another anchoring, that was retrieved from the same badge of removed anchorages during the renovation.

5.2.1. Phases

The microstructure of specimen D-2 is one large Large α -Region with an average diameter of $130 \mu m$. The largest grains observed in this specimen reach a diameter of approximately $800 \mu m$. SEM images of specimen D-2 show no carbides inside the large ferrite grains. The microstructure of this specimen is homogeneous.

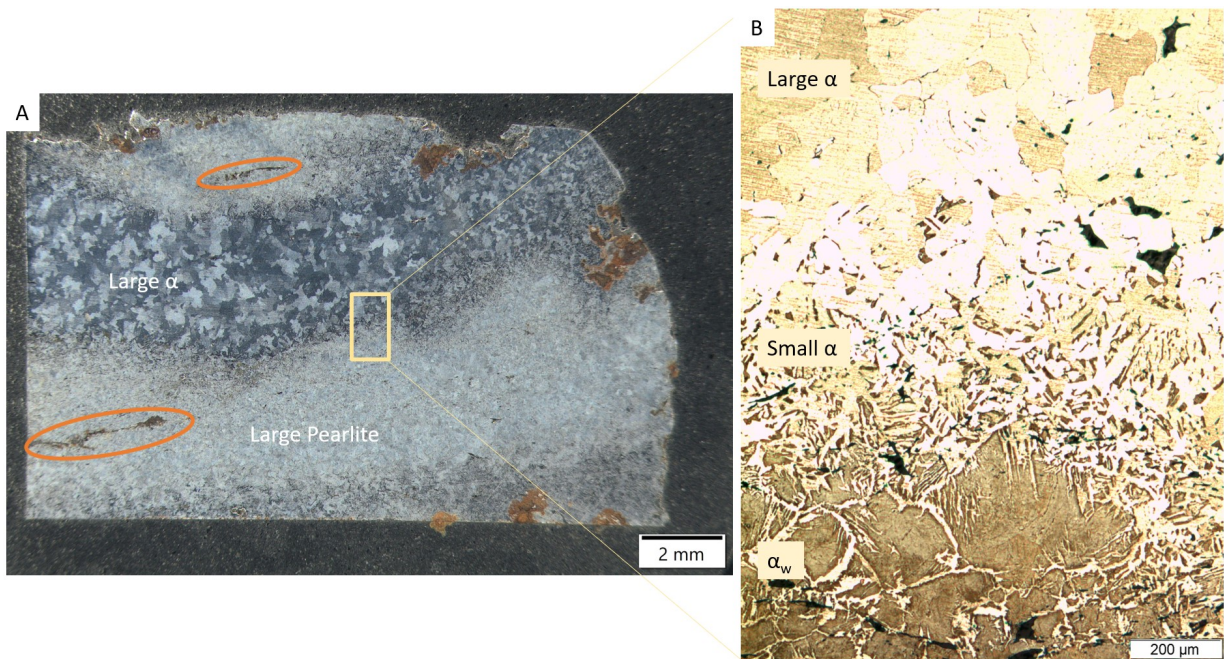


Figure 5.8: A) Macrograph and B) OM image of D1. The orange circles are large strings of inclusions.

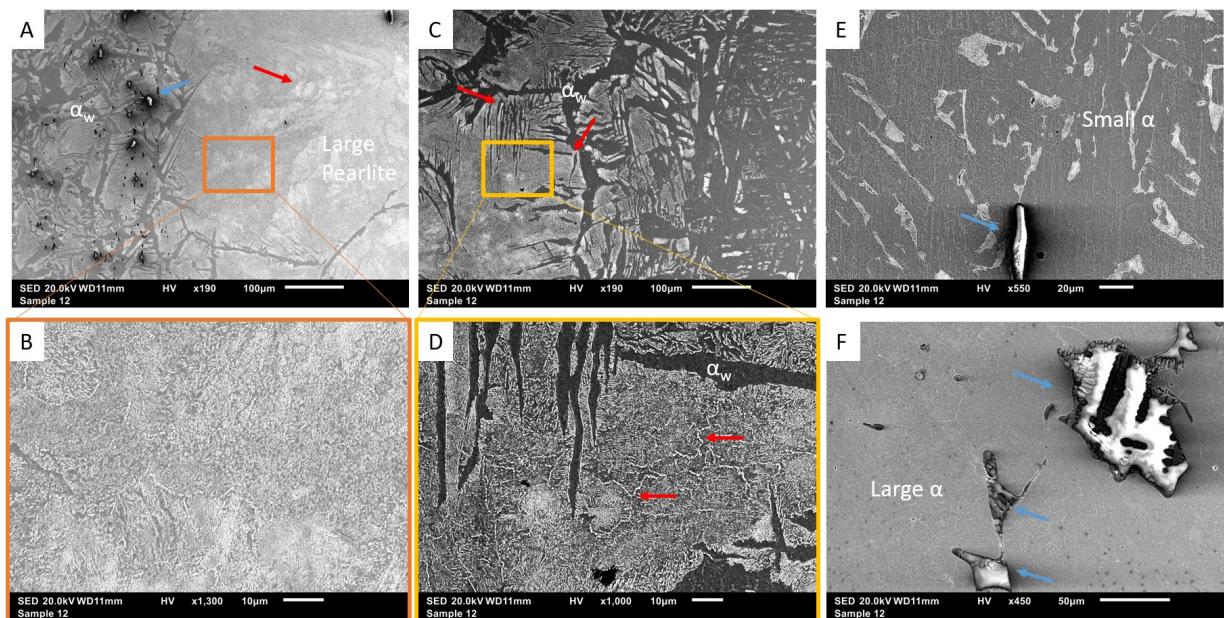


Figure 5.9: SEM images of D-1 A) Large Pearlite Region and α_w -Region, B) higher magnification of the Large Pearlite Region, C and D) α_w -Region, E) Small α -Region and F) Large α -Region.

Specimen D-1 on the other hand, shows multiple phases as seen in the micrograph and OM image in Figure 5.8. Investigation of the cross-section over the height (top to bottom) of the anchorage bar shows several phases. The SEM images in Figure 5.9 provide more detailed information about these phases.

- The top edge has a thick Pearlite Region with minimal allotriomorphic ferrite grains at the grain boundaries and some Widmanstätten needles pointing into the grain. The largest of these observed grains reaches a diameter of around 600 μm . SEM images show that these large grains are pearlitic and have heavily fragmented cementite films, up to a state that films are hard to distinguish and the majority of the cementite are tiny dots and stripes, see Figure 5.9A and B. The red arrow in Figure 5.9A points to heterogeneous vortices that are observed within these grains, which at higher magnification (Figure 5.9B), are observed as higher densities of cementite dots and stripes.
- The Pearlite Region transitions into a α_w -Region, see Figure 5.8B and 5.9C. Broad allotriomorphic ferrites surround semi-large grains and Widmanstätten needles point into the grains at various angles. The red arrows in Figure 5.9C point to some of the needles that are close to the grain boundaries but are not connected to them. Needles cross each other even though they are perpendicular orientated. At high magnification (see Figure 5.9D), the cementite features are observed; Cementite is highly fragmented and appears to form subgrain boundaries around colonies of parallel cementite films (red arrows in Figure 5.9D). However, a large fraction of the cementite is so small that they are not considered films but rather spheres/dots. No pattern can be seen in the cementite density within the pearlite grain.
- A thin stroke of a Small α -Region with a grain size of around 10-20 μm separates the α_w -Region with the Large α -Region. At higher magnification (see Figure 5.9E), it is observed that no carbides are present in the small ferrite grains and that the pearlite grains are mostly composed of cementite films. Both pearlite and ferrite grains have elongated shapes, which could be interpreted as a highly ferrite dominant stage of a α_w -Region.
- The Small α -Region changes into a Large α -Region with ferrite grain sizes between 30 and 100 μm (average 55 μm). Figure 5.9F shows an SEM image of the large ferrite grains. They are covered with small dots/dashes of carbides and faintly show some traces of subgrains.

After the Large α -Region follows another thin layer of a Small α -Region, a layer of an α_w -Region and a thick layer of a Large Pearlite Region. The specimen was cut off at the last α_w -Region. This specimen is clearly built up out of several microstructural layers, which can be interpreted as piling layers.

5.2.2. Slag Inclusions

D-1 and D-2 show a wide variety of slag inclusions that are identified by SEM-(EDS) analysis. The elemental compositions of the slag inclusions measured by SEM-EDS are presented in Appendix B Table 2 and 3. Based on significant amounts of Al_2O_3 present in the various types of inclusions in the D-series, the NRC ratio of $\text{SiO}_2/\text{Al}_2\text{O}_3$ is chosen to compare inclusions inside the specimen.

D-1

The slag inclusions and groups in specimen D-1 are generally elongated in the width of the anchorage. Some examples of various slag inclusions in D-1 are appointed by the blue arrows in Figure 5.9. The slag inclusions detected in D-1 are divided into three categories:

- Two enormous strings of inclusions are present in the α_w -Regions parallel to the large α region, these strings are marked with orange circles in Figure 5.8 A and were seen during the production process of the mock-up. SEM shows a homogeneous tone for the content of these inclusions. This is also seen for a group of slag inclusions that is present in the α_w -Regions, see Figure 5.9A.

Both types of inclusions with a homogeneous content have minimal concentrations of FeO (<5 wt %), high concentrations of SiO_2 (>60 wt%), significant concentrations of Al_2O_3 (± 10 wt%), CaO (± 6 -7 wt%) and K_2O (± 5.0 wt%) and low detection of MnO, MgO, (TiO) and Na_2O . This can be interpreted as pure glass inclusions.

- Upon higher magnification it can be seen that tiny dots (fine pattern) cover glass-like inclusions that are close to the Small α -Region. Some of these strings with tiny dots are just next to the Small α -Region in the Large α -Region.

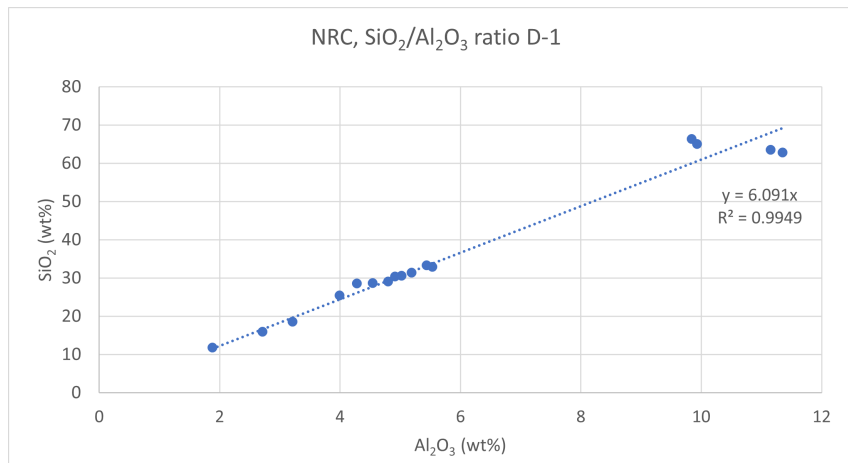


Figure 5.10: NRC ratio $\text{SiO}_2/\text{Al}_2\text{O}_3$ in D-1.

These inclusions have high concentrations of both FeO (40-50 wt %) and SiO_2 (25-35 wt%) and detected concentrations of CaO (± 5.0 wt%), MnO (± 2.2 wt%), K_2O (± 2.8 wt%), Al_2O_3 (± 5.0 wt%), MgO, P_2O_5 , and SO_3 . These inclusions have a bit too much SiO_2 to be fayalite, but this fine pattern might be a combination of glass and fayalite.

- Some relatively large irregularly shaped inclusions are present in the Large α -Region (Figure 5.9F). Figure 5.9F shows that these inclusions have circular shapes orientated in dendritic structures inside a matrix, while the smaller inclusions show a random orientation of circles.

The circles show a very high concentration of FeO (>68 wt%), a minimal SiO_2 concentration between 10-20 wt% and low detections of CaO (± 1.5 wt%), MnO (± 1.0 wt%), K_2O (± 1.0 wt%), Al_2O_3 (1-3 wt%), MgO and P_2O_5 (± 1.0 wt%). This can most likely be interpreted as wüstite bubbles. The matrix shows a slightly lower concentration of FeO (50-60 wt%), a substantial SiO_2 concentration between 20-30 wt%, significant concentrations of CaO (3.0-4.0 wt%), MnO (± 1.5 wt%), K_2O (1.5-2.0 wt%), Al_2O_3 (4.0-5.0 wt%) and detected concentrations of MgO, P_2O_5 and SO_3 . Based on these ratios it can most probably be interpreted as a fayalite matrix.

Figure 5.10 shows a linear correlation between the SiO_2 and Al_2O_3 concentrations in the D-1 slag inclusions. This means that the NRC ratio of all slag inclusions in D-1 is around 6.1 and that these slag inclusions are most probably a direct result of the iron production process. The slag inclusions in the microstructure layers can be distinguished by the presence of Na_2O and TiO_2 in the carbon-rich layer and the presence of P_2O_5 and SO_3 in the carbon-poor layer.

D-2

The inclusions in D-2 are not elongated or shaped in a particular way, see Figure 5.11. Since D-2 has only large ferrite grains without carbides, all inclusions have the same metal environment. The inclusions detected in D-2 are divided into four categories:

- There are relatively large irregularly shaped inclusions with laths shapes and dendritic structures of circles in a matrix, see Figure 5.11A.

The lath shapes have a very high concentration of FeO (>80 wt%), a low concentration of SiO_2 (<10 wt%) and detected concentrations of CaO, MnO, K_2O , Al_2O_3 , MgO, P_2O_5 , SO_3 and TiO_2 . This high concentration of FeO and the low concentration of SiO_2 suggest that the laths are wüstite. The matrix has a high concentration of FeO (53-63 wt%), significant concentrations of SiO_2 (± 20 wt%) and P_2O_5 (± 10 wt%), as well as detected concentrations of CaO, MnO, K_2O , Al_2O_3 and MgO. This SiO_2/FeO ratio could indicate a matrix of fayalite. The dendrites of circles have a high concentration of FeO (67 wt%), a significant concentration of Al_2O_3 (20 wt%), a low concentration of SiO_2 (5.7 wt%) and detected concentrations of CaO, MnO, K_2O , P_2O_5 , SO_3 and TiO_2 . This could be interpreted as wüstite. The NRC ratio of $\text{SiO}_2/\text{Al}_2\text{O}_3$ varies greatly within this large inclusion.

- Slag inclusions with homogeneous content. Upon closer inspection, tiny dots can be seen within these inclusions.

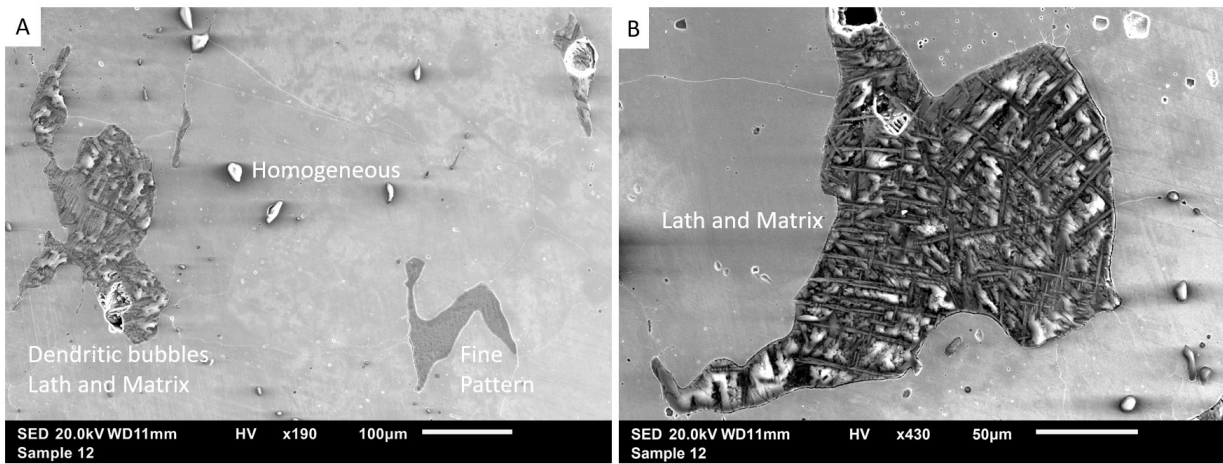


Figure 5.11: SEM-SED images on D2 with 4 types of inclusions.

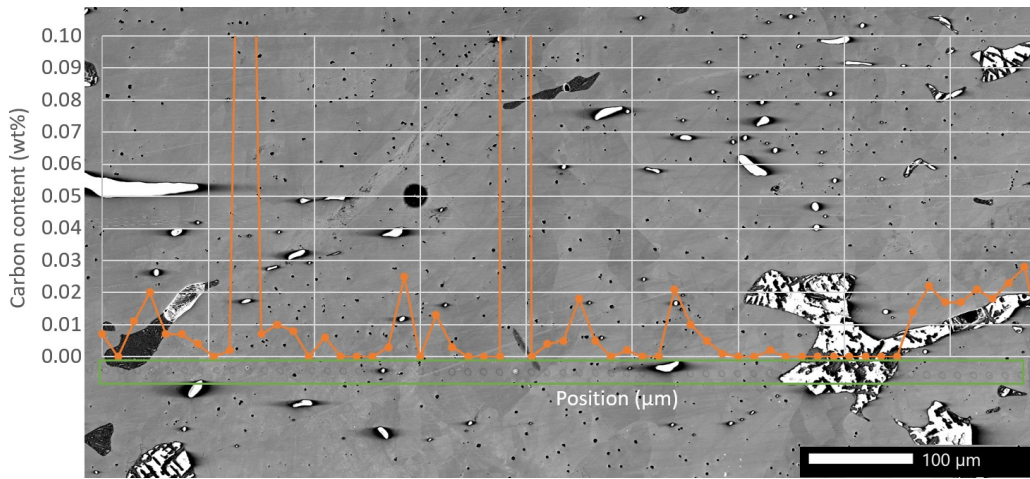


Figure 5.12: Part of the EPMA line on the D2 sample.

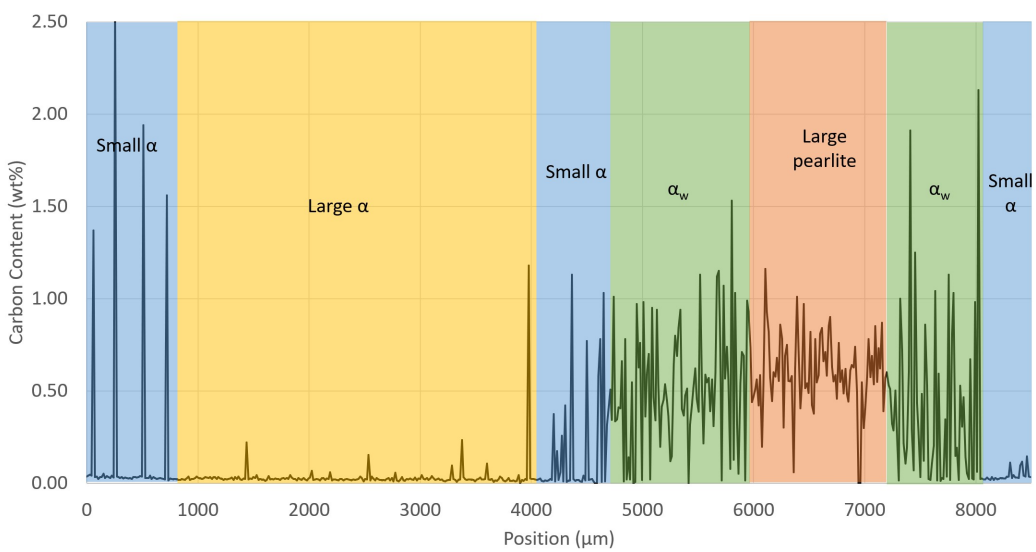


Figure 5.13: The Carbon content (wt%) throughout specimen D1. (EPMA)

These inclusions show substantial concentrations of FeO (± 44 wt%) and SiO₂ (± 24 wt%), a high concentration of P₂O₅ (± 15 wt%) and the detection of CaO, MnO, K₂O, Al₂O₃, MgO and SO₃. These concentrations can be interpreted as a glassy inclusion with possible tiny fayalite dots.

- Slag inclusions with lath shapes in a matrix.

The laths show a high concentration of FeO (>70 wt%), a low concentration of SiO₂ (<15 wt%), a significant concentration of P₂O₅ (2.9-6.5 wt%) and detected concentrations of CaO, MnO, K₂O, Al₂O₃, MgO, SO₃ and TiO₂. Based on the high concentration of FeO, it can be suggested that the laths are wüstite. The matrix has an elemental composition comparable to that of the homogeneous slags described above.

- Slag inclusions with a fine line pattern.

These inclusions have a significant concentration of FeO (± 60 wt%), a low concentration of SiO₂ (<15 wt%), a high concentration of P₂O₅ (± 12 wt%) and detection of CaO, MnO, K₂O, Al₂O₃, MgO, SO₃ and TiO₂. These concentrations slightly resemble fayalite.

In general, it can be said that there is a large variety of inclusions inside this specimen. An important detail is that all measurements show relatively high concentrations of P₂O₅ (up to 15wt%). Additionally, the ratio of non-reduced compounds such as SiO₂/Al₂O₃ fluctuates extremely within this group of inclusions.

5.2.3. Carbon

Specimen D-2 has an average carbon concentration of 0.018 wt%, which is typical of wrought iron. Figure 5.12 shows a fraction of the results. A few extreme peaks are seen on polluted measuring spots but in general the carbon concentration remains between 0.00 and 0.03 wt%. The inclusions contain no carbon at all. Although the metal phase is consistent, the hardness varies between 160-225 HV, with an average hardness of 180 HV being measured.

Specimen D-1 shows large variations in carbon content throughout the cross-section, see Figure 5.13. The Large α -Region has an average of 0.026 wt% and shows only small peaks. The Small α -Regions (blue in Figure 5.13) have a low carbon content similar to the Large α -Region and, depending on the ferrite/pearlite ratio, have some peaks in the carbon content (1.0-2.5 wt%) when a pearlite grain is in the measurement point. The α_w -Regions and Large Pearlite Region show a nice contrast between the allotriomorphic- and Widmanstätten- ferrite and the pearlite grains as the ferrite has a nihil carbon content and the pearlite has a carbon content between 0.3 and 1.2 wt% depending on the cementite density.

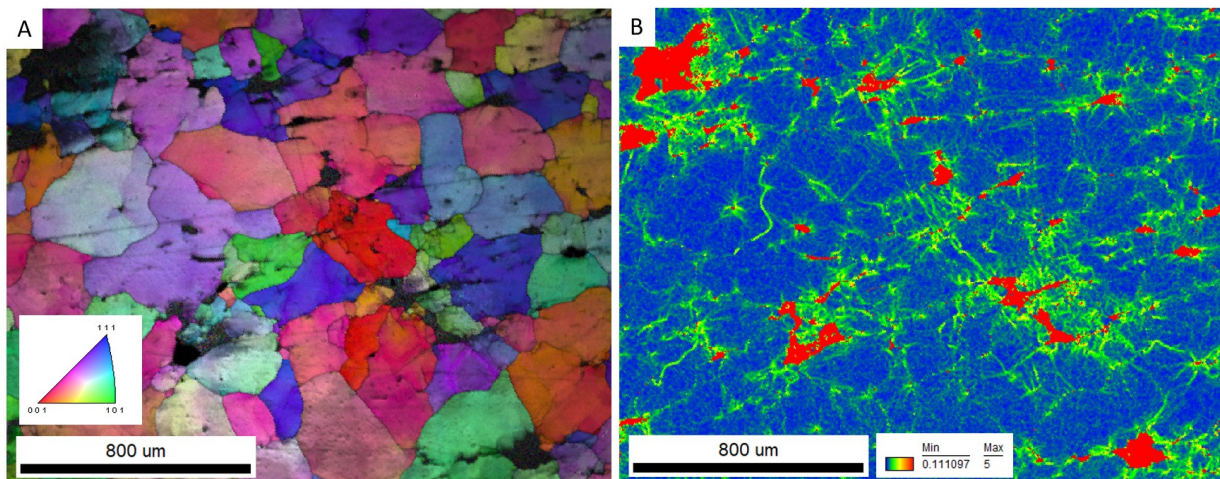


Figure 5.14: EBSD analysis on specimen D2 (large α region) A) IPF +IQ images and B) KAM image.

5.2.4. Crystallographic Characterisation

EBSD images of D2 are presented in Figure 5.14. The IPF IQ image does not show any preferred crystallographic orientation (colour). However, some grey lines within a fairly uniformly coloured grain suggest subgrains. In the KAM map, a clear distinction between inclusions and grains is visible, as the

inclusions are red (maximum local misorientation) and the iron grains are mostly blue (minimum local misorientation). It can be seen that within the grains, the areas near the inclusions have a significantly higher dislocation density (green-coloured) than the rest of the grain. The grain boundaries have an angle misorientation distribution comparable to the random orientation of cubic crystals, with mainly high-angle grain boundaries (HAGB) and significant low-angle grain boundaries (LAGB). The presence of coincidence site lattice (CSL) and Twin boundaries is nihil.

5.3. Results of the Not Bent Mock-up specimens: M-NB-rib and M-NB-edge

M-NB specimen is part of the mock-up series and is the not bent part of the sword. Both rib and cutting edges are embedded in one holder, showing the cross-section so that the lower surface relates to the compressed surface of the M-HB and M-CB series.

5.3.1. Phases

Figure 5.15, shows a micrograph of the entire M-NB cross-section, both cutting edges and the rib. Investigation of the microstructure phases using OM shows the following details:

- Specimen M-NB consists almost entirely of a Small α -Region with a grain size diameter of around 10 μm . However, a difference in the ferrite/pearlite ratio can be seen, as the amount of pearlite grains decreases slightly towards the surface.
- At the rib lower surface, a small Pearlite Region without any allotriomorphic ferrite or Widmanstätten ferrite is observed. The Small α -Regions near the rib upper surface have a slightly higher preference for ferrite.
- The right cutting edge has one small α_w -Region, marked with a orange circle in Figure 5.15.
- Near the left cutting edge, the ferrite/pearlite ratio increases and ferrite occupies the entire microstructure, leaving minimal space for cementite at the grain boundaries or small pearlite grains. The grains are rather small with diameters between 10 and 30 μm . This is a α -Region. On the other hand, the right cutting edge has a low ferrite/pearlite ratio, this is mainly a Small α -Region.

Figure 5.16 shows SEM images of M-NB. Figure 5.16A shows a clear transition from the Small α -Region to the Pearlite-Region. Figure 5.16B, shows a higher magnification of the pearlite region and a wide variety of cementite shapes, small films (blue arrows), large laths (black arrows), and spheres of various sizes (red arrows). In addition, some smaller (dark grey) grains are present in this pearlite area, which shows some martensitic properties but also shows faint film formation (yellow arrows). Figure 5.16C shows the α_w -Region. At a higher magnification Figure 5.16D shows that these pearlite grains are fairly densely covered by cementite films, which are both fragmented (red arrows) and non-fragmented films (blue arrows). Furthermore, Figure 5.16E shows the division between a α -Region and a Small α -Region. This transition seems to be more gradual than the transition from a Small α -Region to a Pearlite Region. However, a large stream of small inclusions is located along this transition. Lastly, Figure 5.16F presents the majority of the M-NB cross-section (Small α -Region) with a low ferrite/pearlite grain ratio.

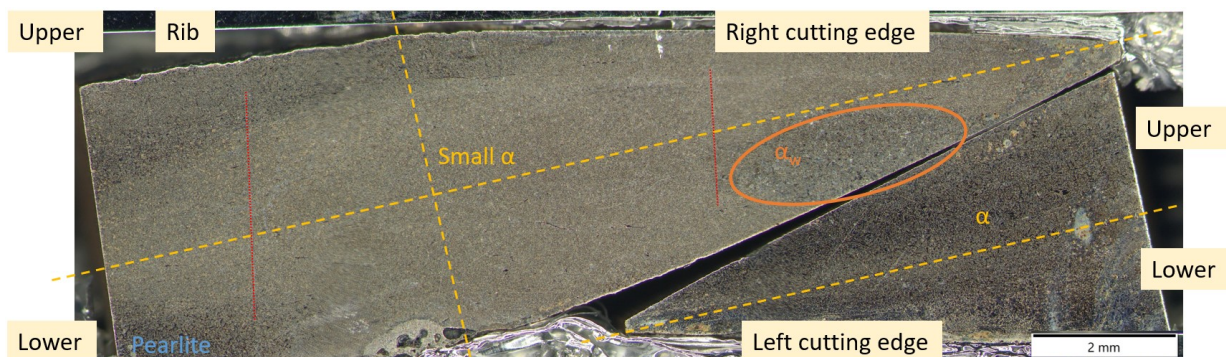


Figure 5.15: Macrograph of specimen M-NB-rib and -edge. The red lines are the location of the EPMA measurements.

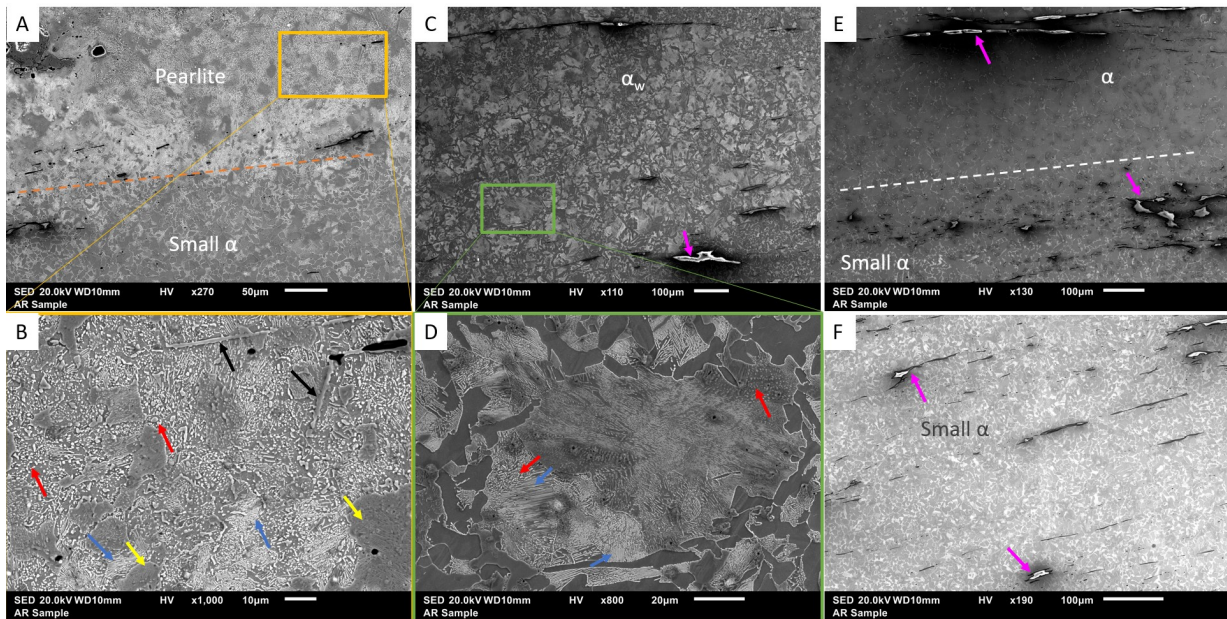


Figure 5.16: SEM-EDS images of M-NB A and B) rib, Pearlite Region and Small α -Region, right edge, pearlite with allotriomorphic ferrite, C and D) right edge, α_w -Region, E) left edge, α -Region and α_w -Region and F) centre rib, Small α -Region.

5.3.2. Slag Inclusions

The elemental compositions of the slag inclusions in M-NB measured by SEM-EDS are presented in Appendix B Table 4. All string inclusions or groups are elongated in the width of the sword. Since the M series originate from the same anchorages as D-1, the elemental composition of the slag inclusions is expected to be comparable. Therefore, the same NRC ratio, $\text{SiO}_2/\text{Al}_2\text{O}_3$, is chosen to compare the inclusion inside the specimen and with other specimens (M- and D-series). The magenta arrows in Figure 5.16C,E,F show some of the slag inclusions observed in specimen M-NB. Based on the shape and visual content of the inclusions, M-NB has two major types of slag inclusions:

- Slag inclusions with homogeneous grey tone. These are observed in the shape of long strings that are sometimes surrounded by small strings or streams of irregular-shaped (large and small) inclusions, see Figure 5.16C,E and F. The large strings in Figure 5.16E have a fragmented content as if air bubbles interrupt the slag content. These types of inclusions are present in α -Regions, Small α -Regions and α_w -Regions.

The elemental composition of these inclusions has a fluctuating ratio of SiO_2/FeO (between 1-20). The inclusion with SiO_2 percentage >63 wt% and a FeO percentage <5 wt% (high ratio) can be interpreted as a glass inclusion. The inclusions with a FeO percentage >30 wt% have significantly too much FeO to be considered glass or even fayalite. Even though the inclusions visually appear glass-like, the type of slag in this homogeneous inclusion is not always glass. Besides the presence of Al_2O_3 , CaO , K_2O , MgO and CaO , a minimal amount of TiO_2 is detected in all these inclusions and a small amount of P_2O_5 and SO_3 are detected in the irregularly shaped inclusions. The NRC ratios (6.0 ± 0.4) of these slag inclusions are similar to the ratios in D-1.

- Slag inclusions with a line pattern. These inclusions have the shape of large strings and are present in Small α -Regions.

They have a high concentration of FeO (± 55 wt%) and a moderate concentration of SiO_2 (± 30 wt%). This could be interpreted as Fayalite. The NRC ratios (4.2 ± 0.1) of these inclusions slightly differ from D-1 and the inclusions above. This could be interpreted as a result of forging the mock-up sword.

5.3.3. Carbon

The EPMA measurements of M-NB-rib and M-NB-edge are similar, as is shown in figure 5.17. The locations of the EPMA measurements are marked by red dashed lines in figure 5.15. Both measurements are in the Small α -Region, as this covered the majority of the cross-section. The EPMA line is alternating due to measuring spots in a ferrite grain, a pearlite grain, inclusion or a combination. The slight change in the ferrite/pearlite ratio is visible as the EPMA graphs show (near) zeros more frequently in the first quarter of the graph than in the remaining three quarters. The average carbon content measured in M-NB-rib is 0.46 wt%. The average carbon content measured in specimen M-NB-edge is 0.59 wt%.

The Vickers hardness indicated that the centre of the M-NB-rib specimen (185 HV) is slightly harder than the surfaces (136-159 HV) and that the right cutting edge (191 HV) is harder than the left cutting edge (151 HV). This is consistent with the observed phase zones as pearlite generally has a higher hardness than ferrite.

5.3.4. Crystallographic Characterisation

Figure 5.18 presents EBSD images (IPF+IQ and KAM) of both the M-NB-rib and the M-NB-edges. No dominant texture is detected in the IPF maps and pole figures and the misorientation distribution is comparable to the theoretical distribution of randomly oriented crystal cubes. However, the histogram of the misorientation distribution shows a small peak for LAGB ($<5^\circ$) and some peaks near 30° , which deviates slightly from the theoretical random orientation.

Figure 5.18A shows the KAM map of the rib. It is evident that there are fewer local misorientations near the upper surface as the KAM map is bluer. The KAM suggests that the highest concentrations of local misorientations are in the middle of the rib and near the lower surface (red circles). The IPF +IQ image corresponding to this KAM image shows random colour combination of small grains.

Figure 5.18B shows the IPF+IQ image of both edges, the upper triangle is the right cutting edge and the lower triangle is the left cutting edge. It is unmistakable that the two edges differ in grain size. The left edge has larger grains with irregular shapes (white arrows). The relatively large regular-shaped grains near the lower surfaces (below the yellow dashed line) correspond to a α -Region. The small grains throughout the right edge correspond to a Small α -Region with small pearlite grains. Figure 5.18C shows the corresponding KAM image to Figure 5.18B. The gap and some slag inclusions are coloured red, indicating total local misorientation. The right edge shows a more yellow layer on the upper surface (outlined in black), indicating more local misorientation than the remaining of the edge. Otherwise, the local misorientation is rather homogeneously distributed. The left edge is generally bluer, but a distinction can be made between above and below the yellow dashed line. Above the yellow line, the irregularly shaped grains (white arrows) are blue, while everything in between is more green. Below the yellow line, less local misorientation is observed. In general, the Small α -Region can be interpreted as a region with many local misorientations. Note that Figures 5.18A and C cannot be compared because the measurement step size is different and therefore the points in the kernel are of different sizes and thus incomparable.

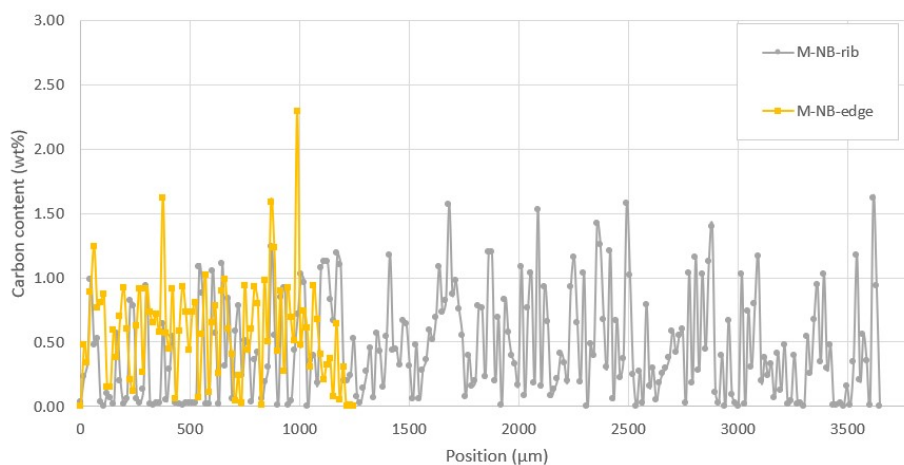


Figure 5.17: Carbon content EPMA measurement of M-NB.

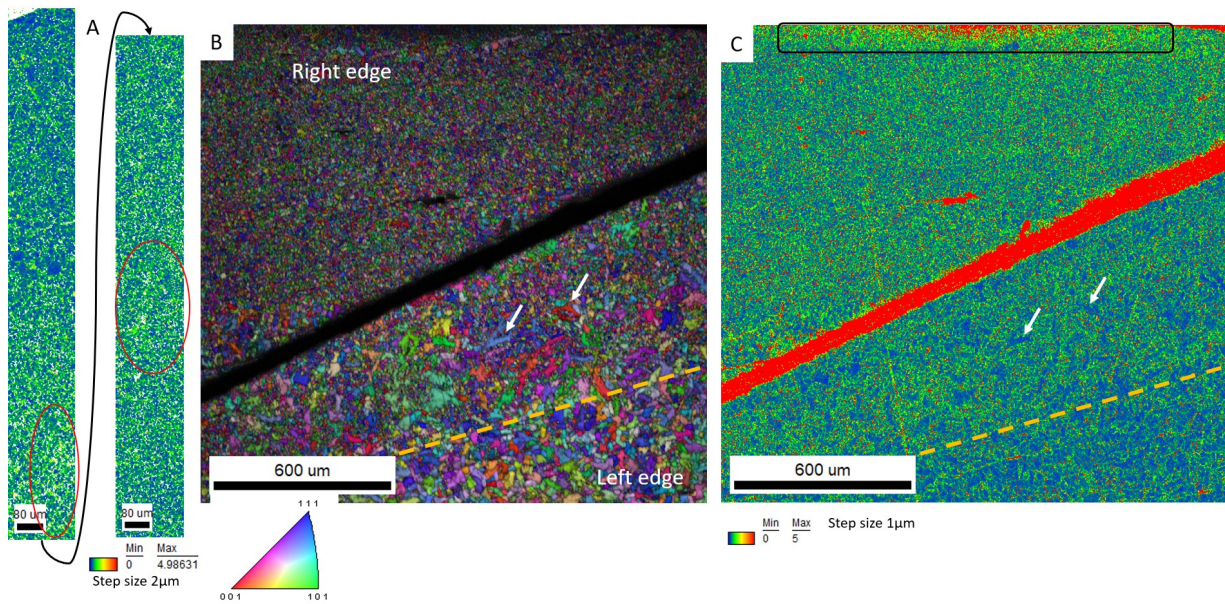


Figure 5.18: EBSD images of M-NB A) KAM of M-NB-rib, B) IPF+IQ of M-NB-edges and C) KAM of M-NB-edges

5.4. Results of the Hot Bent Mock-up specimens: M-HB-rib and M-HB-edge

The M-HB specimens are part of the mock-up series and are bent by reheating and hammering. The rib and the cutting edge are analysed separately. The samples are cut so that when referring to the upper surface, it is the surface that experiences pull forces, while the lower surface experiences compressive force due to bending.

5.4.1. Phases

Figure 5.19 shows that M-HB-edge has a network of large inclusions or cracks that separate two primary structures. The following microstructures are observed:

- The lower part consists of a Large α -Region, with the majority of the grains having a diameter between 20-150 μm and an average of 54 μm .
- The upper part consists of a Small α -Region, with the majority of the grains having a diameter between 5-15 μm and an average of 7 μm . Near the upper surface, a small α_w -Region is observed.

Figure 5.20 shows SEM images of M-HB-edge. Figure 5.20A shows that the Large α -Region has some cementite in the grain boundaries (white arrow) but does not contain carbides inside the ferrite grain itself. Figure 5.20B shows that the Small α -Region consists of ferrite grains with small pearlite grains and some cementite between the grain boundaries (white arrow). Figure 5.20C shows that the α_w -Region has large pearlite grains with (fragmented) cementite films. In the large pearlite grains, meandering cementite seems to indicate subgrains with films in various directions, densities and fragmentation (white arrows). No correlation is detected between the cementite density and the location within the large pearlite grain.

M-HB-rib has some large inclusions but these are not connected in a network. Comparable to M-HB-edge, this specimen is divided into two primary structures: The lower half is a Large α -Region and the upper half is a Small α -Region. In the left upper corner, near the surface of the mock-up sword, a small α_w -Region is observed. Near both surfaces of the mock-up sword, the grains seem to be deformed into elongated shapes, as is shown in Figure 5.21A and B (black arrows). The phases are similar on higher magnification as seen in the M-HB-edge specimen and Figure 5.20.

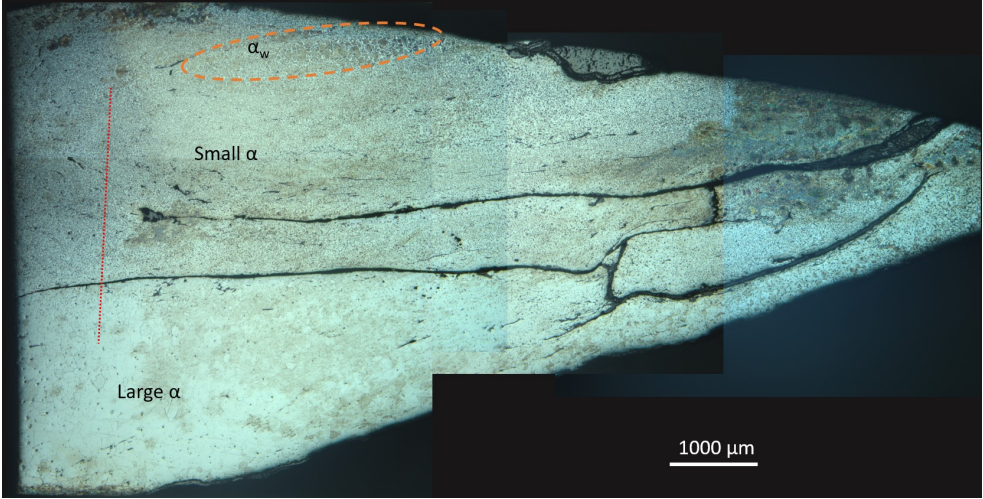


Figure 5.19: OM of M-HB-edge, Large inclusions separate the microstructures. The red line is the location of the EPMA measurements.

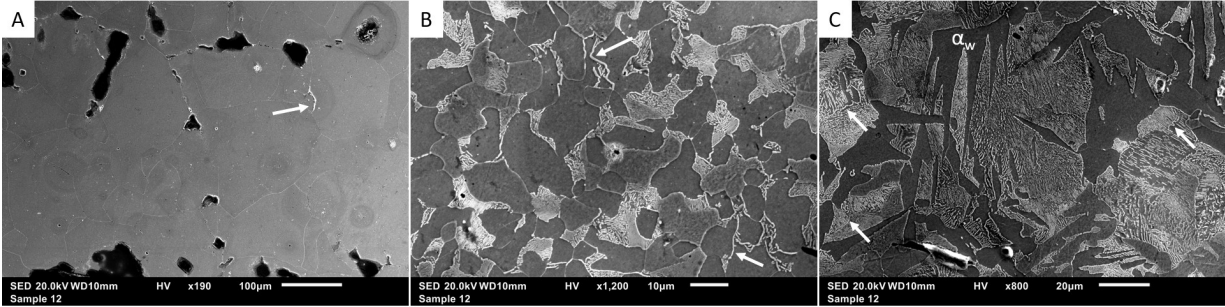


Figure 5.20: SEM of M-HB-edge A) a Large α -Region, B) a Small α -Region and C) a α_w -Region.

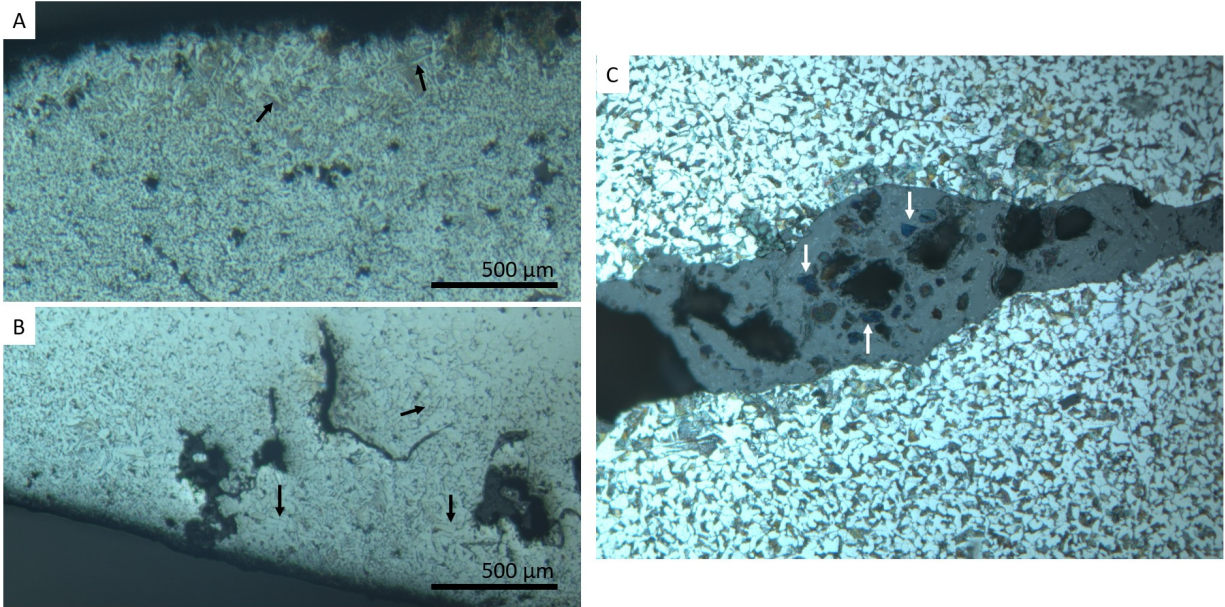


Figure 5.21: OM of M-HB-rib, deformed grains near the surfaces of the mock-up sword. A) the upper surface in the Small α -Region and B) the lower surface in the Large α -Region. C) Inclusions with glass pieces.

5.4.2. Slag Inclusions

The network inclusions in M-HB-edge (Figure 5.19) appear to consist of cracks as SEM-EDS shows difficulty in measuring any content. Some of the smaller inclusions around these cracks are empty (no slag) as well; SEM-EDS has difficulty with the measurements and only detects Fe, O and N. Figure 5.20A shows such inclusions. The SEM-EDS results with the elemental composition of slag inclusions in both M-HB-rib and -edge are presented in Appendix B Table 5. All slag inclusions are elongated in the width of the sword. Next to the cracks and empty inclusions three types of slag inclusions are observed:

- Figure 5.21C shows a giant inclusion with visible blue pieces inside, see the white arrows. Are these glass pieces? This is not seen in any other slag inclusion within this thesis. With SEM this inclusion showed a chaotic slag content with many small dots and dendrites of circles in a matrix. The various particles are not easily distinguished in the SEM image.

SEM-EDS showed for all measurements, independent of location in this slag, a high concentration of FeO (>70 wt%), a low concentration of SiO₂ (<26 wt%) and minor detection of CaO, MnO, Al₂O₃ and MgO. This could be interpreted as a relatively pure slag inclusion that might be a fine structure between wüstite and fayalite/glass. In this case, the blue particles could actually be olivine pieces. The NRC ratios (39-68) for this inclusion are very high and not comparable to any other slag NRC ratio measured in this thesis. This could indicate that this odd inclusion entered the iron in a late stadium of the production process or maybe during the forging of the mock-up sword.

- Smaller slag inclusions with a homogeneous content are observed close to the cracks or in groups in the Small α -Region.

These inclusions have a SiO₂ concentration higher than 50 wt%, a low FeO concentration (<17 wt%) and significant concentrations of Al₂O₃ (± 10 wt%), CaO, MnO, MgO and K₂O. Noteworthy is the low detection of TiO₂ in all of these inclusions. They can all be interpreted as glassy slag inclusions. With one exception, they also have similar SiO₂/Al₂O₃ NRC ratios (6.1 ± 0.7) to D-1 and the M-series.

- Slag inclusions with a fine dot/line pattern are observed in the Large α -Regions and the Small α -Regions with a relatively high ferrite/pearlite ratio.

These slag inclusions show an elemental composition with moderate concentrations of both SiO₂ (35-45 wt%) and FeO (35-45 wt%). Next to the detection of CaO, MnO, K₂O, Al₂O₃ and MgO, small amounts of P₂O₅ and SO₃ are observed. These SiO₂ concentrations are slightly too high to be interpreted as fayalite. However, these fine dots/line patterns could be a fine structure of wüstite and fayalite. Again the NRC ratios (6.0 ± 0.3) are comparable to D-1 and the M-series. Two slightly high NRC ratios (± 8.4) are seen in this type of inclusion, this could be a result of the forging of the mock-up sword.

5.4.3. Carbon

Figure 5.22, present the carbon content measured through both specimens. The EPMA measurements of M-HB-rib and M-HB-edge show a clear difference between the carbon concentrations in the primary structures (Large and Small α -Regions). The exact reason for every peak is determined by examining the specimen's EPMA marks. Specimen M-HB-rib has a glass-slag inclusion separating the Large and Small α -Regions. In the Small α -Region, the carbon content fluctuates between 0.00 and 1.50 wt% (average 0.46 wt%) depending on the measuring spot hitting a small ferrite grain, a small pearlite grain or a fraction of both. The Large α -Region has an average carbon content of 0.024 wt%. In a few cases, the EPMA measuring spot includes a grain boundary with cementite and measures an elevated carbon concentration.

In specimen M-HB-edge, a crack separates the Large and Small α -Regions. The Large α -Region has an average carbon content of 0.016 wt% without any abnormal peaks. The Small α -Region again fluctuates between 0.00 and 1.50 wt% with an average of 0.39 wt%. A few areas show less frequent peaks above the 0.25 wt%, these areas go along with higher ferrite/pearlite ratios. Moreover, one of these areas coincides with a large stream of inclusions.

The Vickers hardness shows that the ferrite grains in the rib have an average of 150 HV and the cutting edge is slightly harder with an average of 160 HV. No clear correlation between the hardness and the grain size is seen.

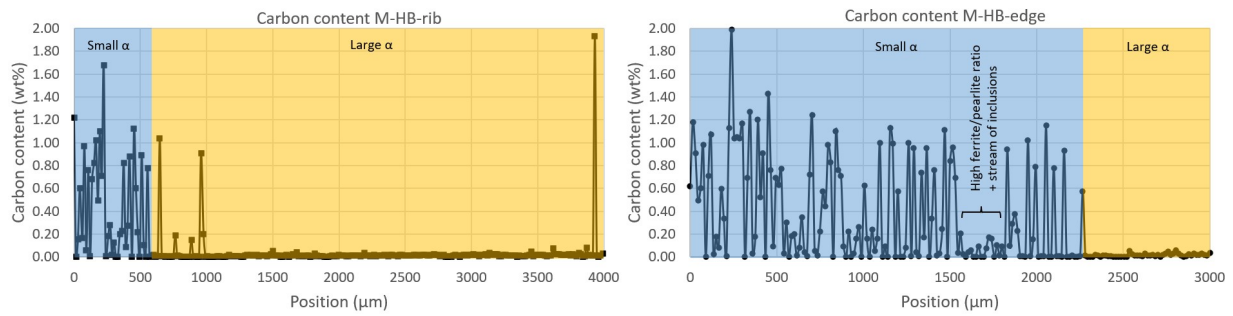


Figure 5.22: EPMA measurement of M-HB-rib and -edge.

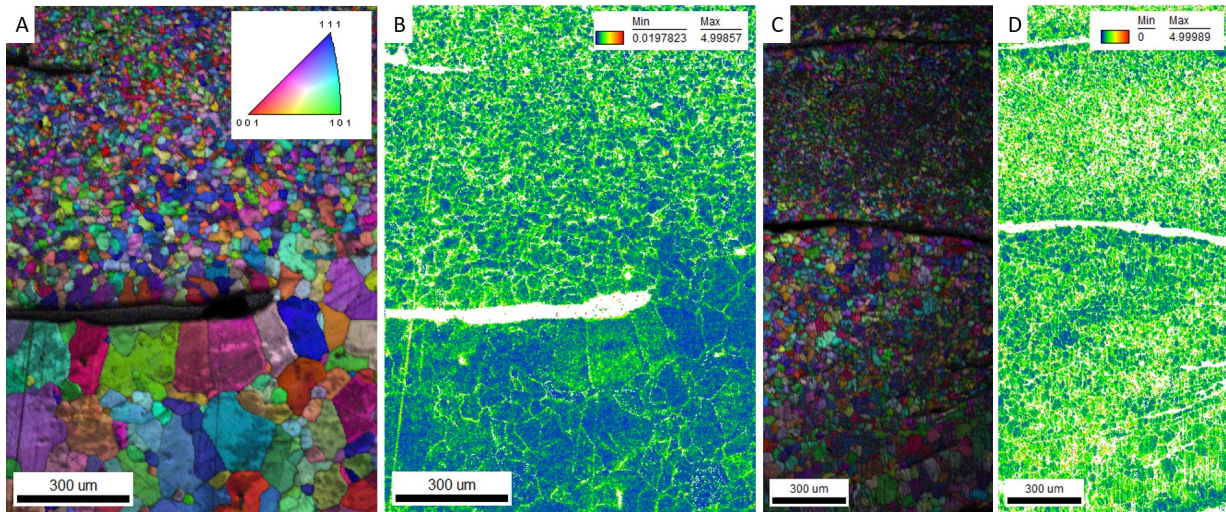


Figure 5.23: EBSD analysis on specimen A,B) M-HB-rib and C,D) M-HB-edge both IPF +IQ image and KAM image (B. stepsize 2 μm , D. stepsize 1.5 μm).

5.4.4. Crystallographic Characterisation

Figure 5.23 presents the IPF+IQ image and KAM image of M-HB-rib and M-HB-edge. SEM-EBSD reveals no dominating texture for both M-HB-rib and -edge as the IPF is a random mixture of all colours. Both Figure 5.23A and C, present no favoured crystallographic orientation. The misorientation distribution of grain boundaries in specimen M-HB-rib is rather similar to the theoretical (McKancie) random misorientation distribution of cubic crystals, except for a high amount of LAGB indicated by a peak for angles smaller than 5 degrees. M-HB-edge seems to have an additional high peak for 45° angles. The KAM of specimen M-HB-rib shows an evident difference in local misorientation for the Large α -Region and the Small α -Region, respectively above and below the inclusion. The Small α -Region is prominently more green than the Large α -Region, indicating a higher dislocation density in this region. This can be interpreted as more local misorientation and higher dislocation densities in the Small α -Regions than in the Large α -Regions. The Large α -Region maintains this concentration of local misorientation until just before the surface when it slightly increases colouring the large grain greener, but in the last 100 μm from the surface, the local misorientation seems to have vanished. The KAM of the Small α -Region seems to stay consistent further along the cross-section up to the last 100 μm where it decreases in value. The IPF,IQ image of specimen M-HB-edge shows slightly larger grains around the cracks even when the major structure consists of small grains. Additionally, KAM shows that the area near the crack has less local misorientation than the bulk structure, regardless of the primary structure.

5.5. Results of the Cold Bent Mock-up specimens: M-CB-rib and M-CB-edge

The M-CB specimens are part of the mock-up series and are cold bent with a leverage effect. The samples are orientated so that when referring to the upper surface, it is the surface that experiences pull forces, while the lower surface experiences compressive forces due to bending.

5.5.1. Phases

Figure 5.24 shows macrographs of the entire M-CB cross-section. Large cracks and inclusions create boundaries between some of the phase regions observed (white lines). In Figure 5.25 more details of the phases are shown. The following phases are observed:

- The rib and the left cutting edge both show large strings of inclusions and cracks, which separate an α_w -Region with a Small α -Region, see the white lines in Figure 5.24 and the black arrow in Figure 5.25A and Figure 5.25B. The pearlite grains are shown in Figure 5.25C, these grains have partly fragmented films of cementite. The pearlite grains appear to be built out of several subgrains as the cementite films exist in colonies of various densities, degrees of fragmentation and directions. For example, the black arrows point towards subgrains with a high density of barely fragmented films in horizontal or vertical directions and the white arrows point towards subgrains with a low density of highly fragmented films in several directions. Some of the grains only have a faint cementite pattern (yellow arrows).
- The Small α -Region generally has grains with a size between 10 and 30 μm in diameter. Most of the grains have a slightly elongated shape. After two streams of small inclusions the phase changes to a region with large ferrite grains (Large α -Region).
- This Large α -Region consists of ferrite grains with a size between 30 and 80 μm (diameter). Figure 5.25D shows that these grains have some minor carbides in the grain boundaries but nothing inside the grains (white arrows). This phase dominates the left cutting edge (Figure 5.24).
- The α_w -Regions dominate the right cutting edge, but there is also a small area where no Widmanstätten ferrite and the allotriomorphic ferrite are observed, a Pearlite Region. Figure 5.25E and F show this Pearlite Region. Different shades of gray are observed for these grains using SEM. At a higher magnification (Figure 5.25F), only a part of the grains show cementite films (white arrows), the other part shows patches of different shades but no clear structure (black arrow).

5.5.2. Slag Inclusions

Various types of inclusions are observed in the M-CB specimens. Appendix B Table 6 presents the SEM-EDS results of the elemental composition of the slag inclusions in M-CB. All inclusions (strings or streams) are orientated parallel to the width of the swords. The slag inclusions detected in M-CB are divided into three categories:

- There are slag inclusions with a content of circular shapes in a matrix. These are observed in major strings or streams of smaller inclusions.

The circular shapes have an extremely high concentration of FeO (>95 wt%) which can be interpreted as wüstite. SEM-EDS confirms this as the pure elemental analysis only presents Fe and O with an atomic percentage ratio of 1:1. It is a characteristic feature of wüstite to have a high purity.

- There are slag inclusions with a homogeneous content, that are observed in the shape strings or groups of more irregular shapes. These inclusions are seen in Pearlite Regions, α_w -Regions and in Small α -Regions.

The slag inclusions in the Pearlite Regions and the α_w -Regions have a low FeO concentration (<10 wt%) and a high SiO₂ concentration (>60 wt%). This could be interpreted as glass slag inclusions. The slag inclusions in the Small α -Region have a higher concentration of FeO (30-45 wt%) and a low concentration of SiO₂ (35-50 wt%). This can not be interpreted as glass or fayalite, it might be that a dot pattern was missed in these inclusions and that it is a combination of wüstite and fayalite/glass. Most of the SiO₂/Al₂O₃ NRC ratios (6.0 ± 0.7) are comparable to those of D-1 and the M-series.

- Some of the major inclusions seen along the white lines in Figure 5.24 have a fine dot pattern.

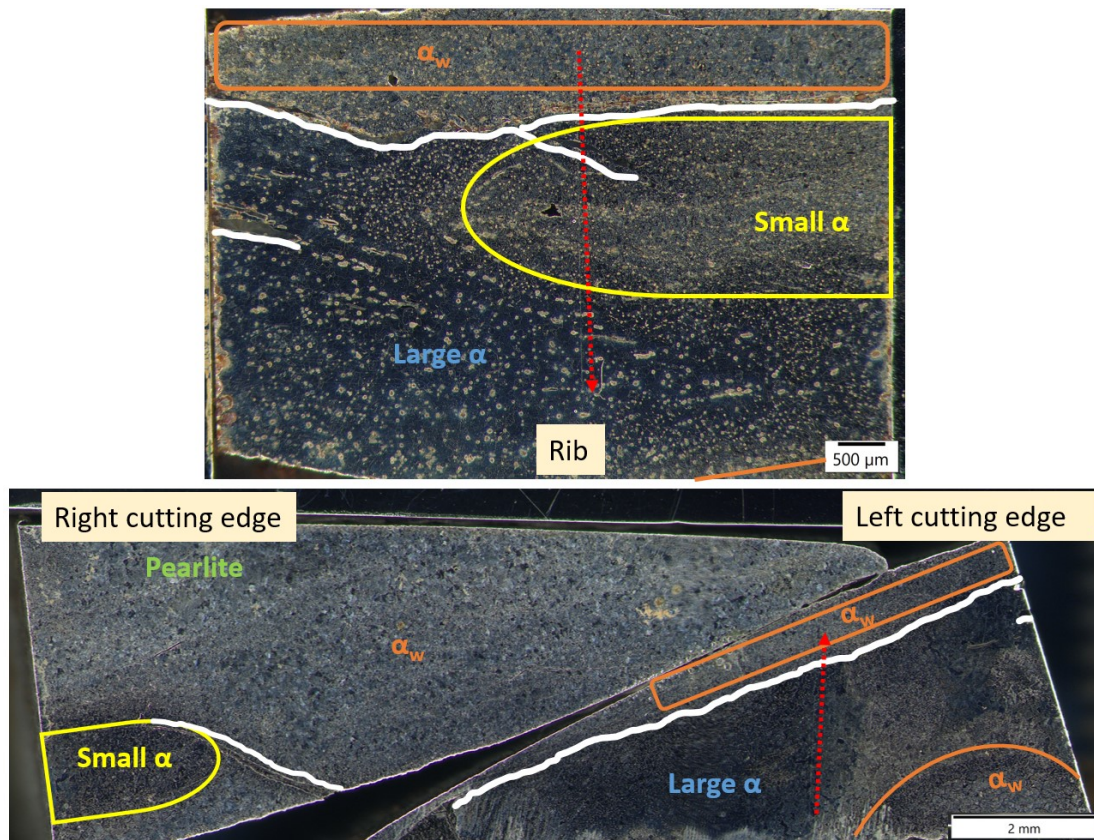


Figure 5.24: macrographs of specimens M-CB-rib and -edges. White lines follow large cracks or inclusions; Red dots indicate the EPMA measuring line; Various phase regions are indicated.

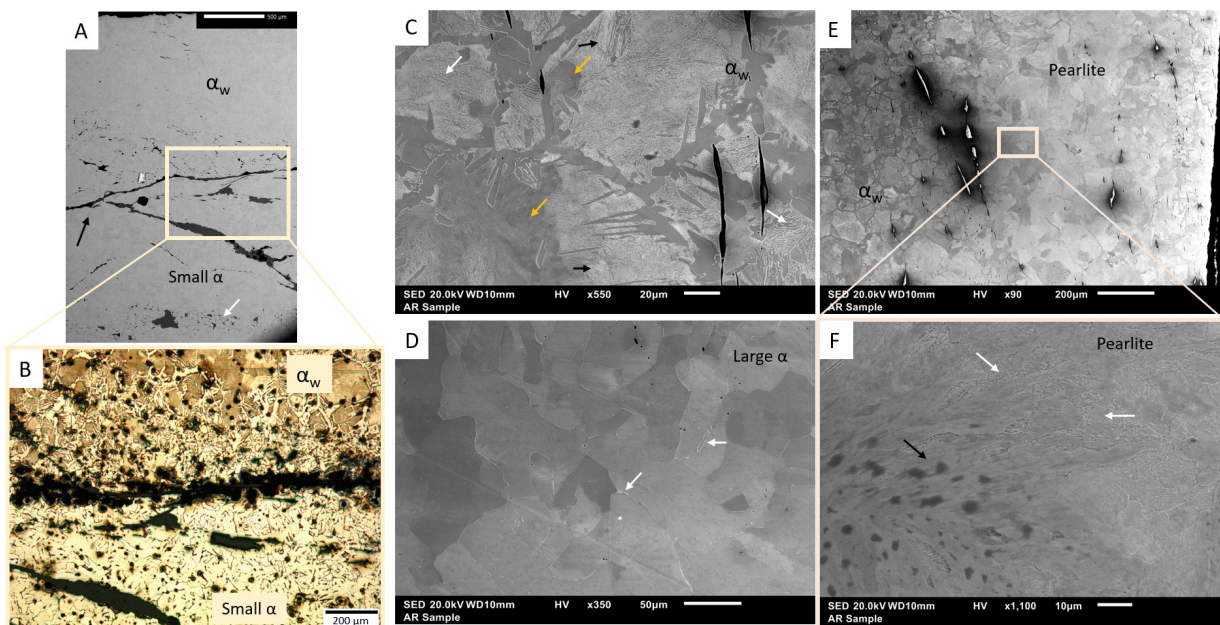


Figure 5.25: SEM images and an OM image of the M-CB specimens. A) SEM (backscatter) show the pattern of inclusions. B) OM showing the α_w -Region transition into the Small α -Region. C) α_w -Region. D) Large α -Region. E) Transition between α_w - and Pearlite Region. F) Pearlite Region.

The elemental composition has an almost 1:1 ratio for SiO_2/FeO and has relatively low concentrations of the remaining NRCs. Therefore the NRC ratios are significantly higher than seen in D-1. This could be caused by the influence of the forging of the mock-up or bending of the sword since the inclusions are present along the main cracks.

Based on the elemental composition of all the slag inclusions the following interpretation can be made. Inclusions with bubbles inside and an almost pure iron oxide elemental composition can be interpreted as wüstite. These inclusions are not representable for the $\text{SiO}_2/\text{Al}_2\text{O}_3$ ratios. A large group of inclusions have a $\text{SiO}_2/\text{Al}_2\text{O}_3$ ratio around 5-6, independent of the SiO_2/FeO ratio. This can be interpreted as a group of inclusions originating from the same iron production process. Inclusions with different ratios indicate a strong influence during the forging of the mock-up or the presence of piling layers.

5.5.3. Carbon

Figure 5.26 presents the EPMA measurements of M-CB-rib and M-CB-edge. The location of the EPMA measurement on the specimen is seen in Figure 5.24. The measurement of M-CB-rib starts with a high carbon concentration in the middle of the α_w -Region. Approaching the first major inclusion, the Widmanstätten ferrite becomes more dominant and the carbon content becomes more erratic. The α_w -Region has an average carbon content of 0.31 wt%. The first major inclusion separates the α_w -Region from the Small α -Region, and the second major inclusion divides the Small α -Region in two. Next, a small inclusion creates a boundary between two gradients of ferrite/pearlite Small α -Regions and a stream of small inclusions separate the Small α -Region with a Large α -Region. The Small α -Region exist of a lesser pearlite area with an average carbon content of 0.07 wt% and a more pearlite area with an average carbon content of 0.22 wt%. The more pearlite the higher the chance to have cementite in the EPMA measuring spot. The Large α -Region has a general average of 0.02 wt%.

The measurements of M-CB-edge start in a Large α -Region with a carbon content of average 0.02 wt%. A major inclusion separates the phase from a α_w -Region with a Small α -Region. The Small α -Region has an average carbon content of 0.18 wt% and the α_w -Region has an average carbon content of 0.44 wt%. In general, the change in carbon content is coherent with the phases, inclusions are clear boundaries in the carbon content and phase changes, and they have close to no carbon in their content. The Vickers hardness of M-CB indicates that the centre of the mock-up sword is the softest with a hardness of around 135 HV. Closer to the sword surface the hardness measurement ranges from 159 HV to 222 HV.

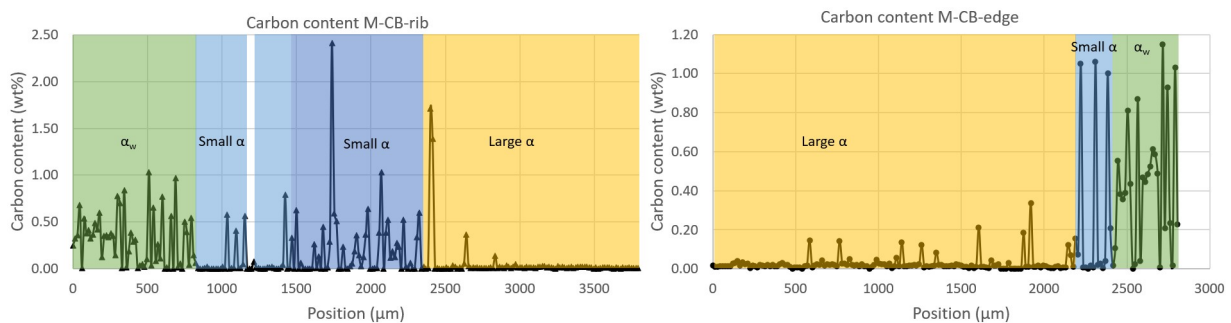


Figure 5.26: Carbon content, EPMA measurement of M-CB.

5.5.4. Crystallographic Characterisation

Figure 5.27, presents detailed IPF+IQ and KAM maps over the entire height of the rib of the cold bent mock-up sword, starting at the lower surfaces and going up. It is clear that a high local misorientation is seen near the lower surface (red encircled). Moreover, these grains are smaller and have irregular shapes elongated diagonally. Then the Large α -Region starts and local mislocations are generally detected at (sub)grain boundaries. A few grey lines on the IQ mapping indicate subgrain boundaries. In the third column the ferrite/pearlite region starts and the grains become smaller and irregular in shape, at the same time the local misorientation increases. Halfway through the fourth column, the α_w -Region starts and a high concentration of local misorientation is detected. Be aware, in the fourth column the inclusions are red coloured as well. The microstructure near the upper surface is visualised with a slightly higher magnification. The grains are diagonally elongated and have a significantly higher local misorientation

inside the grains. However, the most upper layers of grains appear to be free of local misorientation.

Specimen M-CB-rib has no preferred orientation as the pole figures and the IPF show random patterns. The grain boundaries show a misorientation angle distribution rather similar to the theoretical misorientation distribution for random cubic orientations. Grain boundaries with a 45° angle are noticeably present in high amounts.

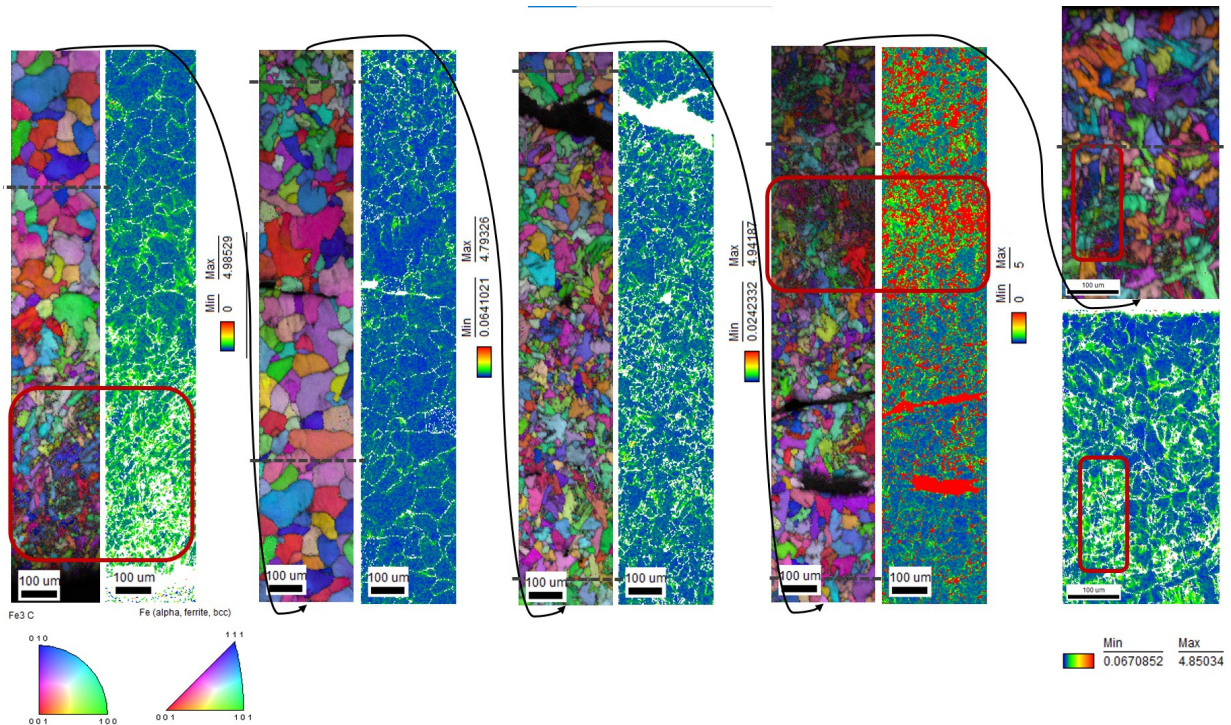


Figure 5.27: EBSD images (IPF+IQ and KAM) of specimen M-CB-rib.

Specimen M-CB-edge has a slight microstructural difference between the left and right edges. However, both have small grains, irregularly shaped grains, no preferred orientation and a misorientation distribution similar to random cubic orientation. The left cutting edge appears to have higher local misorientation than the lower surface of the rib. The grains around a stream of small inclusions seem to have less local misorientation than the grains not close to the stream. Additionally, the elongated allotriomorphic grains around the large pearlite grains seem to have significantly low local misorientations compared to the pearlite grains.

Discussion

6.1. The Heythuysen Sword

In this section, the results of specimen H-CS-8 are discussed and related to the historical concept of the Heythuysen sword. The focus is on the microstructure and slag inclusions. The crystallographic characterisation of H-CS-8 is compared with the M-series bending effects and discussed in Section 6.4.

6.1.1. The Microstructure of the Heythuysen Sword

The H-CS-8 cross-section shows the presence of at least three microstructural phases in the Heythuysen sword:

- A region for large ferrite grains ($\pm 100 \mu\text{m}$) in the centre of the sword.
- A bulk of small ferrite grains ($\pm 15 \mu\text{m}$) and small pearlite grains, with some cementite in the grain boundaries and carbides in the ferrite grains.
- Some regions of coarse pearlite grains with Widmanstätten and allotriomorphic ferrite near the surfaces of the sword. These pearlite grains show a higher density of cementite films near the pearlite-ferrite grain boundaries and show fragmented cementite in the core of the pearlite grain.

The initial hypothesis for the microstructure of Early Iron Age objects was based on the historical theory of iron production. Iron ore would be heated up to 1200°C ; The carbon monoxide from the charcoal reacts with the iron ore, producing metallic iron (Fe) and creating a reducing atmosphere in which only a nihil amount of carbon diffuses into the metal. Most of the slag would melt from the iron bloom in the furnace and part of the remaining slag would be removed by hammering out the liquid from the solid bloom after it was removed from the furnace. Theoretically, this would result in wrought iron with some slag and a very low carbon content ($< 0.02 \text{ wt}\%$), most likely occurring in a purely ferritic microstructure. Therefore, it is unexpected that the H-CS-8 cross-section shows the presence of at least three microstructural phases in the Heythuysen sword.

The EPMA results show a significantly higher carbon content than predicted and carbon-containing phases such as small pearlite and ferrite grains (small α -region) and coarse pearlite grains (α_w -region) are observed. Assuming that the three microstructures are not a direct result of the possible attendance of the sword on a cremation pyre, it can be said that the blacksmith who made the sword knew carburisation techniques. A decreasing carbon gradient can be observed from the surface (α_w -Region) through the bulk (Small α -Region) to the centre (Large α -Region) of the sword. This is characteristic of the carburisation of an entire object [38]. However, due to the severe corrosion, it is debatable whether the current sword surface is representative of the original sword surface. The analysed iron from H-CS-8 is only the iron that remained after years of exposure to corrosion. Furthermore, the coarse pearlite grains are located as seemingly random patches along the sword surface, suggesting that carburisation did not provide a homogeneous diffusion of carbon into the sword. This does not dismiss carburisation but suggests the presence of other microstructural interference. An explanation for this could be the use of piling techniques to enlarge the forging stock. Piling of several iron bars (originally different blooms) can result in layers/patches with originally different carbon concentrations and/or microstructures.

It is noteworthy that no martensite is observed in H-CS-8. Therefore, it can be concluded that water quenching was most probably not the last phase-changing modification step in the history of the sword.

Furthermore, no obvious piling pattern in the form of multiple-layered microstructures, as described in Section 2.2.2 Figure 2.10, is observed. This queries the use of piling techniques as suggested above.

α_{w} -Region

The α_{w} -Regions in H-CS-8 have a peculiar repetitive structure with various degrees of fragmented cementite (films) in the core of the pearlite grains and dense cementite films with small interlamellar spacing near the pearlite/ferrite grain boundaries (Section 5.1.1, Figure 5.3C, D). There is currently no clear explanation in the literature for this specific phenomenon. The cementite and ferrite patterns in pearlite are known to have many features such as films, curvatures, discontinuations and holes [60], [61]. The characteristics of these regions are somewhat comparable to the so-called "old pearlite" mentioned in Section 3.2. However, the mechanism behind this combination of different features is still controversial. A few suggestions towards these characteristics are made.

First suggestion: Figure 6.1 shows an example of a Continuous Cooling Transformation (CCT) diagram for a low alloy steel [62]. Note that this CCT is not fully representative of our samples as it is a characteristic property that depends on the elemental composition of the steel. For example, slow cooling creates a microstructure consisting of ferrite (F) and pearlite (P). The slower the cooling, the larger the average grain size. During cooling, allotriomorphic and Widmanstätten ferrite may grow into austenite grains (Section 3.2.1 Figures 3.6 and 3.7). When this happens carbon will diffuse away from the ferrite towards the ferrite/austenite grain boundaries. As the cooling process continues, pearlite transformation begins at these ferrite/austenite grain boundaries and cementite films start forming. However, if the carbon content is insufficient to stimulate further carbon diffusion into the austenite grain, the growth of the cementite films could stop and individual carbides might form.

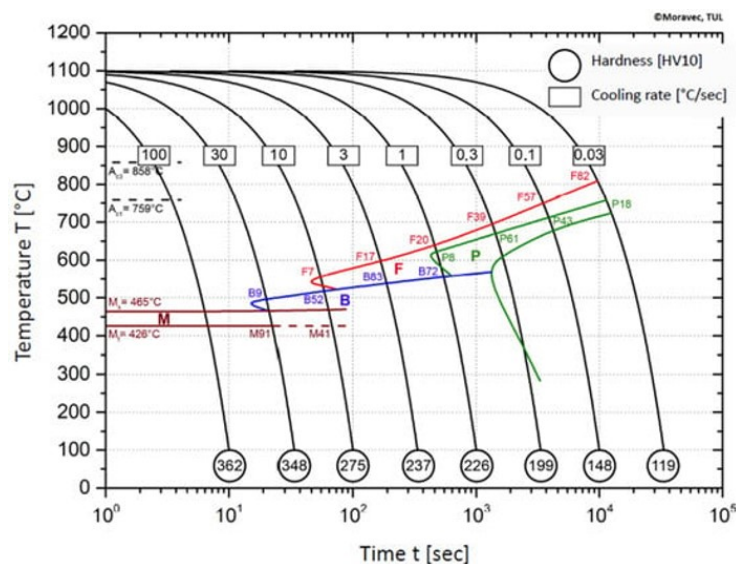


Figure 6.1: CCT of a low alloy steel, retrieved from [62]

Second suggestion: As suggested in the old pearlite theory, see Section 3.2. Over time, carbon could diffuse very slowly through the ferrite, resulting in a minor spheroidising effect as the films disintegrated into small spheres. This process could occur more slowly near the grain boundaries due to less favourable thermodynamics. Contemporary spheroidising occurs at a temperature of around 700 °C for several hours and produces cementite spheres with a larger diameter than the film thickness [53], [54]. In this case, the cementite spheres are equal to or smaller than the films, which does not support the spheroidisation theory. The question remains if the fragmentation of cementite films is a characteristic feature of ageing iron.

Third suggestion: In a study on Early Medieval Celtic knives in the United Kingdom, spheroidisation and carbide needles are explained as the intentional destruction of objects because they drastically reduce the hardness of blades [63]. In this case, they assume that the Celtic people knew that heat treatment would reduce the quality of an iron object. Regarding the results of this thesis, this assumption might be a bit too enthusiastic. Blakelock and McDonnell even go so far as to claim that a spheroidisation heat treatment

is part of the ritual killing of the blades. Heat treatment during the burial ritual could be in the form of a cremation pyre. In the pyre, temperatures can fluctuate over the locations, reaching up to 1000°C in the upper part and the centre and up to 1200°C near the fuel load [14]. These temperatures are too high for spheroidisation as austenitization temperatures are reached. On the outskirts of the pyre, the temperature could be lower and thus good for spheroidisation. However, if spheroidisation is the case, larger spheres might be expected. One could wonder if ageing might have decreased the size of the spheres.

6.1.2. Slag Inclusions inside the Heythuysen Sword

The type of slag inclusions in an object can tell a lot about the history of an object, as discussed in Section 3.2.2. The literature explained that elongated slag inclusions are oriented in the direction of maximum forging deformation (Section 3.2.2). The elongated inclusions in H-CS-8 are aligned with the width of the sword. However, the majority of the inclusions in H-CS-8 are large groups of tiny dots, possibly indicating strings perpendicular to the cross-section, as suggested by literature [22]. These observations and theories could be explained by the historical theory of sword production (Section 2.2.2). This would suggest that the sword is deformed first in length, lengthening the stock, and then in width, widening the sword and creating cutting edges. Since the groups of dots inclusions are located mainly in the rib and middle area of the cross-section and the strings are mainly located in the cutting-edge area, it can be concluded that the lengthening of the sword had the greatest impact on the central area, creating inclusions perpendicular to the cross-section. The widening of the sword had the largest impact on the edge areas, creating elongated inclusions across the width of the sword. It can be concluded that the shape of the inclusions would support the hypothetical sword production technique.

There are three types of inclusion observers in H-CS-8:

- Circular shaped Wüstite in a fayalite matrix, which exists in groups of small inclusions or large irregular shapes in Small α -Region metal phases.
- Singular strings of glassy inclusions occurring in α_w -Region metal phases.
- Strings of fine dot patterns occurring in Small α -Region metal phases.

The first two types of inclusions are similar in shape and metal phase correlation to the inclusions described in the literature review, Section 3.2.2. This theory claims that low furnace temperatures cause a reducing atmosphere that results in FeO-rich slag inclusions and carbon-free metal phases and high furnace temperatures cause an oxidizing atmosphere that results in FeO-poor inclusions (SiO₂-rich) and a metal phase with carbon. Assuming that the inclusions are a direct product of iron production means that the wüstite-fayalite and the glass inclusions are products of different badges of iron production because they exist in different metal phases. This could lead to the conclusion that the α_w -Regions with glass strings and the Small α -Regions with wüstite-fayalite and fine dot pattern inclusions are different piling layers and that the difference in carbon concentration may not be caused by the carburisation of the final product alone but by different furnace temperatures during the iron production.

However, it remains to be discussed if the slag inclusions are a result of iron production or processing. The literature (Section 3.2.2) states that if inclusions are a direct product of iron production, they should have a constant NRC ratio. Therefore, piling layers have different NRC ratios as they originate from different blooms. An inconsistent ratio could also be caused by phase partitioning during the iron processing, the use of additives during forging and the use of sand during welding. In this case, there are at least three different categories of SiO₂/CaO ratios. Three NRC categories suggest three piling layers. However, even within the same group of inclusions, differences in SiO₂/CaO ratios are seen. Therefore, it can be concluded that the forging process or heat treatment did affect the inclusions and that carburisation cannot be excluded. The strict distinction in the location of the wüstite-fayalite and glass inclusions cannot be ignored and therefore piling techniques are also not excluded. Most likely, a combination of piling and carburisation was applied to this sword.

Finally, the notable elements contained in the H-CS-8 slag inclusions are discussed. Manganese oxide is present in relatively large concentrations. Manganese is known to be present in bog iron ore, often in combination with phosphorous and arsenic [23]. Phosphorous predominantly enters the slag phase but is not detected in the slag of this sword. Arsenic is detected in the Heythuysen pieces using Nuclear Resonance Capture Analysis (NRCA), see Appendix D. Manganese preferably enters the glassy phases but also partitions into wüstite according to literature [23]. The elements compose a fairly specific fingerprint

about the origin of the iron ore. A comparison of the Iron Age slag from Hallstatt and the Netherlands could lead to a good estimate of the origin. Compared to the research done on early iron production in the Netherlands (Early Medieval period) by Joosten [23], the slag inclusions from Heythuysen are best comparable to slag from rattlestones from the Veluwe.

6.2. The Original Anchorages of the Domtoren

In this section, the original state of the microstructure and slag of the Domtoren steel is discussed. This is important in order to evaluate the results from the Mock-up correctly. It also contributes to the history of these Domtoren pieces.

6.2.1. The Microstructure of the Domtoren Anchorages

The D-series results show that although the specimens are thought to have a similar origin, the microstructure is very different. D-2 has a typical wrought iron structure, consists of very large ferrite grains of up to 800 μm and contains a very small amount of carbon (0.018 wt%). D-1, on the other hand, shows clear microstructural layers of four phase types, suggesting the use of piling techniques and knowledge of alternating carburised and carbon "free" steels. The Pearlite Regions and the Large α phase form the main microstructure of the layers. The Small α -Regions and α_w -Regions appear to exist only as a small transition layer between the main phases. Based on this, at least three layers of iron were piled up to create this anchorage.

It is essential to compare D-1 (origin of the mock-up) with H-CS-8 (original Early Iron Age sword) on a microstructural basis to see to what extent the former is representative of the latter. Both have multiple phases but the main phases are different. An extensive comparison between the microstructure of H-CS-8 and D-1 is presented in Table 6.1. In conclusion, the microstructure of D-1 is not a perfect match to represent the Heytyhuysen sword as a microstructural replica. However, the arrangement of several phases with roughly Small α -, Large α - and α_w -Regions are as close to a microstructural replica as could be achieved in this thesis. Moreover, the age and old production techniques used to make the anchorages are more similar to the ancient techniques used for the Heythuysen sword than the contemporary steel production techniques.

	H-CS-8	D-1
Microstructures	Multiple: Large α -Regions, Small α -Regions and α_w -Regions	Multiple: Large α -Regions, Small α -Regions, Pearlite Regions and α_w -Regions
Main phases	Small α -Region	Pearlite Region + Large α -Region
Clear microstructural layering pattern (piling)	Piling suggested	Clear pattern, piling technique was applied
Large α-Region	No carbides	Small carbides (dots/needles), cementite at grain boundaries
Small α-Region	More energetically favourable round shaped grains	Elongated grains, resemble dominant α_w and α_{all}
α_w-Regions	High cementite density near ferrite-pearlite grain boundaries, extreme fragmentation of cementite in grain core	Higher cementite density, more evident cementite spheres, cementite sphere form subgrain boundaries
Pearlite Region	n/a	Variations in interlamellar spacing and degree of fragmentation (independent of subgrains or pearlite colonies)

Table 6.1: Microstructural comparison between H-CS-8 and D-1.

6.2.2. Slag Inclusions in the Domtoren Anchorages

The slag inclusions of D-1 and D-2 are also very different. D-2 is composed entirely of ferrite grains and has a low carbon content. According to the literature, only FeO-rich inclusions are expected in this metal phase, which is exactly the case since all D-2 inclusions have a FeO content higher than 44.0 wt%. This is connected to low furnace temperatures. The shape and orientation of the inclusions in D-2 provide no indication of the forging direction, as no predominant elongated shapes are observed. The wüstite-fayalite inclusions with laths (and dendritic bubbles) shapes in a matrix are unique in this study as they are only observed in specimen D-2. This also applies to the relatively high concentration of P_2O_5 (up to 15 wt%).

Phosphorous oxide in slag goes hand in hand with phosphorous in the iron matrix, the ratio depends on oxygen fugacity and temperature [23]. Below 900 °C phosphorous remains in its oxidised state and above 900 °C phosphorous prefers the a reduced state [23], [64]. Note that this thesis does not include measurements for phosphorous concentration in the metal. Therefore, the exact ratio P(iron): P_2O_5 (slag) of D-2 is unknown, so an accurate estimation of the iron production temperature cannot be made based on this theory. It could be suggested that P_2O_5 concentrations above and around 10 wt% are high enough to indicate the preference for the oxidised state, which would suggest a temperature below 900 °C. However, a connection between the mineral phase and the concentration P_2O_5 can be seen as measurements taken in the fayalite matrix of the wüstite-fayalite inclusions and the fine pattern inclusions are significantly higher in P_2O_5 concentration (9.5-15.5 wt%) than in the FeO-rich (wüstite) laths and bubbles (0.9-6.5 wt%). This indicates that P_2O_5 prefers glassy surroundings. Moreover, these high phosphorous concentrations suggest the use of phosphorous-rich iron ore such as bog iron ore, which is commonly found in Europe and the Netherlands. Lastly, the NRC ratios fluctuate extremely from 0.3 to 33.3, indicating the processing procedures interfered with the slag inclusions.

D-1, on the other hand, does have glass slag inclusions preferentially found in the α_w -Regions and Pearlite Regions (carbon-rich) and wüstite-fayalite inclusions in the Large α -Regions (carbon-poor). This is consistent with the theory explained in Section 3.2.2. Although piling is suspected based on the microstructural layers, the NRC ratios suggest that the iron originates from one production as all ratios are the same (6.1 ± 0.6). The slag might not indicate a clear distinction via the SiO_2/Al_2O_3 NRC ratio, it does present a distinction via the presence of other NRC's. Na_2O is present in the slag of the Pearlite Regions and α_w -Regions and P_2O_5 and some SO_3 are present in the slag of the Large α -Region. Thus the hypothesis of the use of piling layers is still valid. The constant NRC ratio indicates that the slag is minimal affected during processing, which means that the slag represents the iron production process well. In this case, the low concentrations of P_2O_5 and MnO do not support the use of bog iron ore. Noteworthy are the relatively high concentrations of Al_2O_3 , up to 11.4 wt% in the glass inclusions (pearlite layer) and up to 5.5 wt% in the glassy inclusions (ferrite layer). Al_2O_3 can originate from both the iron ore and the coal ashes [35]. However, these high concentrations suggest the presence of aluminium in the iron ore.

It can be concluded that the anchorages (specimen D-1 and D-2) were most likely made from different iron ore due to the large difference between the concentration of the phosphorous oxides and aluminium oxide. Moreover, the use of piling techniques is observed in D-1 and not in D-2. The final microstructures suggest that the production process of these iron anchorages has been different. It is remarkable that iron objects, used for the same purpose on the same building for centuries, have such different microstructures. Therefore, it is more likely to date from the 14th century than from the early 20th century as one would expect a more homogeneous iron microstructure or even cast iron for the reinforcement of buildings in the 20th century. Moreover, these extreme differences in microstructure/production process and the big difference in size and shape of the anchorages, see Figure 4.3, might suggest the use of scrap metal as anchorages. Since iron production was not yet done on large scales, the use of scrap metal would not be strange for the 14th century.

6.3. The Mock-up Sword

All mock-up specimens originate from the anchorage of specimen D-1, therefore all changes in the microstructure and slag inclusions can be associated with the reforging of the metal or the bending of the sword. The reforging process of the anchorage into the mock-up sword is the same for all M-series specimens. Macrostructural differences within the M-series could therefore be allocated to the bending procedures. Furthermore, minimal differences in slag inclusions are expected as the bending procedures should have a minimal effect on the inclusions. In this section, the mock-up specimens are compared with each other and specimen D-1 in terms of microstructure and slag inclusions.

6.3.1. The Microstructure of the Mock-up Sword

The forging of the mock-up sword was carried out while the iron was yellow-orange coloured by the heat of around 1100/1200 °C (Section 4.1.2). Thus the austenisation temperature was achieved and allowed the carbon to move more freely through the metal. Reheating was only done for short periods between hammering, therefore the carbon does not have much time to diffuse over long distances. Hammering will cause plastic deformation and thus creates more possibilities for dislocations and carbon to move. The traces of plastic deformation will fade during every annealing cycle. On the contrary, clear microstructural layers are seen in specimens M-HB and M-CB, which indicates that reforging does not eliminate the characteristics of the piling method. Therefore, it can be stated that the lack of microstructure layers in specimen M-NB is due to the heterogeneous distribution of the piling layers.

The main Large α -Regions in M-HB and M-CB has changed slightly compared to specimen D-1. The average carbon concentration is the same (below 0.026 wt%), the grain size is of the same order (30-150 μm) and a small amount of carbides is seen at the grain boundaries. On the other hand, the carbides inside the D-1 ferrite grains have disappeared in the M-series. This could be an effect of reforging the metal. Additionally, the separation between major phases in the M-series is often accompanied by large cracks/inclusions throughout the specimen. The inclusions are already seen in D-1 and the cracks are most probably initiated and grown during the bending process. The major Pearlite Regions in D-1 appear to have been replaced by major regions of α_w and Small α in the M-series as almost no large Pearlite Regions are seen in the M-series and α_w - and Small α -Regions are the dominant high carbon major phases. This suggests a decrease in the carbon content in these regions.

Comparing the EPMA carbon content of D-1 and of the M-series, it is observed that on average the high carbon areas in D-1 have a slightly higher carbon content than the high carbon area in the M-series. This indicates that no carburisation occurred during the forging process but rather minor decarburisation. Unlike the Large α -Regions, the Pearlite Regions underwent a transformation. The cementite features of the small Pearlite Regions seen in the M-series are slightly different from the Pearlite Regions in D-1. This is evident in figures 5.9B and 5.16B at the same magnification. Figure 5.16B (M-NB) shows a large variation in cementite features, including relatively large spheres that mimic spheroidisation, while in 5.9B, the spheres are difficult to distinguish and the cementite is more densely packed. Spheroidising was not part of the reforging process so it is surprising to see this structure, although it is only visible in a small area on the surface of the mock-up. Could this be the result of uneven cooling? It is hard to say because the mock-up sword was laid outside (summer air) to cool after reforging. The α_w microstructure of the M-series is quite similar to the D-series as all have various degrees of fragmentation and various interlamellar spacings.

The M-NB specimens act as a blank for the bending experiment. The cross-section on the not bent part of the mock-up sword consists almost entirely of small ferrite and pearlite grains, only the ratio differs. The right cutting edge contains a high concentration of pearlite, including some α_w -Regions, while the left cutting edge has a higher fraction of ferrite. This indicates no microstructural symmetry through the rib axis of the mock-up sword. M-CB shows that the sword is more consistent in length as the right cutting edge shows higher carbon areas in M-CB-edge (α_w -Regions) than the left side (Large α -Regions). Microstructural differences due to hot or cold bending are not systematically observed using OM or SEM. The SEM-EBSD results have more information about the effects of bending. This will be discussed in Section 6.4.

6.3.2. Slag Inclusions inside the Mock-up Sword

Generally, all string-shaped inclusions are orientated in the width of the sword as they were in the width of the anchorage. The forging process therefore did not gravely disturb the orientation of the inclusions. At most, it might have slightly enhanced the elongation. Most of the M-series inclusions have a high aluminium oxide concentration with a $\text{SiO}_2/\text{Al}_2\text{O}_3$ ratio around 6 as was seen in D-1, with exceptions of the wüstite inclusion, which preferably does not absorb Al_2O_3 . Exceptions are the large inclusion and the small inclusions surrounding these large inclusions, which separate the two major phases in M-CB, they have less Al_2O_3 (ratio $\text{SiO}_2/\text{Al}_2\text{O}_3$ around 12-17); And the large inclusion with various particles in M-HB, which look more like contamination than an original slag inclusion. Furthermore, the distinction between the slag inclusion in the two major phases in D-1 was made based on the presence of Na_2O and some TiO_2 in the pearlite-rich layer and P_2O_5 and SO_3 in the ferrite-rich layer. The distinction between these two can still be seen in the entire M-series. Therefore it can be concluded that the reforging of D-1 into the M-series had an overall minimum effect on the composition of the slag inclusions. The inclusions found in the M-series can be divided into three groups:

- **Glass inclusions**, these are homogeneous inclusions with a FeO concentration below 10 wt% and SiO_2 above 60 wt% plus significant amounts of NRC's. This group has a subgroup of **glassy inclusions**, which are inclusions that predominantly consist of glass but still have a respectable amount of FeO present (10-25 wt%).
- Inclusions consisting of a **combination of glass and fayalite**, these inclusions often show a fine dot pattern, only visible at high magnification. Their SiO_2/FeO ratio of these inclusions is around 1. Increasing the fraction of fayalite shows a fine line pattern, which might be the initiation of lath growth.
- Lastly, **wüstite inclusions** are inclusions filled with pure wüstite circles in a matrix of glass or fayalite. These wüstite circles have minimal contamination and have a FeO concentration above 95 wt%. When these circles are measured for pure elements SEM-EDS gives a 1:1 ratio for the atomic percentage of Fe:O, confirming that the iron oxide is indeed FeO, wüstite.

6.4. How were the Swords Bent?

According to the theoretical hypothesis, EBSD should be able to help identify stored strain energy resulting from plastic deformation, i.e., the bending of a sword by brute force. KAM shows local misorientation relative to a measuring point, i.e., it presents the location and intensity of the misorientation. KAM is independent of the grains, phases, and grain boundaries because it is kernel-based and is, therefore, one of the best mappings for showing the effects of plastic deformation. Hypothetically, local distortion in the crystal lattice structure will be caused by bending and the creation of plastically deformed, resulting in a higher dislocation density and higher KAM values, suggesting stored strain energy in the grain. The IQ mapping provides a qualitative analysis as defects in the material lower the image quality and areas with a larger concentration of defects caused by plastic strain distribution will darken the IQ map [65]. However, IQ has many other factors that influence the grey tint, such as grain boundaries, phases and topology [65] and is therefore not the most trustworthy analysis for plastic deformations. When the sword is bent using a smith's fire and hammering, the stored strain energy will escape during the annealing. While bending our mock-up sword, the sword was annealed until a light cherry/orange-red colour, about 870-1090 °C. This induces austenisation and thus the release of almost all stored strain energy. Therefore, the amount of stored strain energy left inside the object can distinguish the use of a smith's fire or brute force.

The swords are bent over the width, both the historical and the mock-up swords. Figure 6.2 shows a schematic illustration of the main forces in play. Bending over the width means that the impact of deformation is the largest on the surface sides of the rib. The lower half of the sword will experience compression and the upper half will experience tension.

6.4.1. The Bending Experiment of the M-series

The EBSD data from the M-series is difficult to compare due to multiple phases and various proportions of these phases. This is a difficulty also seen in the structure of the Heythuysen sword. Before reforging, the wrought iron has no preferred crystallographic orientation (D-series). After reforging and bending, no dominant crystallographic orientation is found in the M-series, referring to no texture formation during the treatment process.

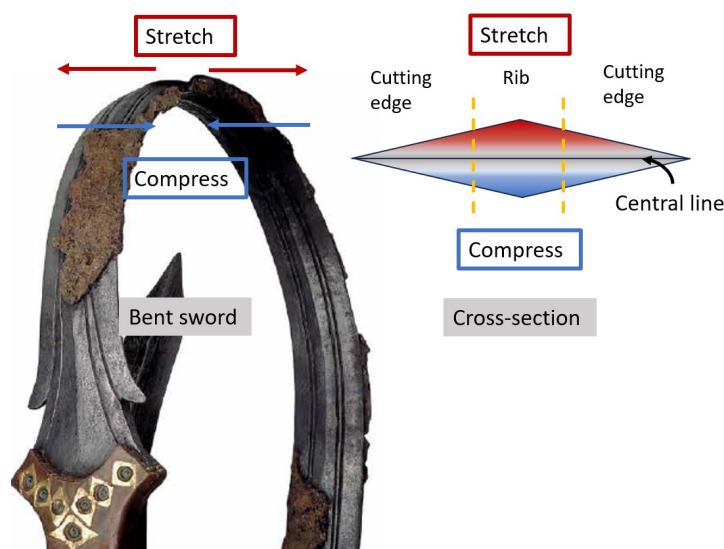


Figure 6.2: Deformation forces on a bent sword.

The KAM mapping of the M-NB-rib (not bent) shows that the highest concentration of local misorientation is present in the centre of the rib and a little towards the lower surface (Figure 5.18A). The difference in local misorientation is however minimal. As stated before, the rib of specimen M-NB consists fully of Small α grains with a gradient in the ratio ferrite/pearlite grains. Towards the surfaces, the amount of pearlite grains decreases, increasing the ferrite/pearlite ratio, the lowest ratio is in the centre. This is parallel to the gradient in local misorientation found in the KAM mapping. A clear difference in KAM value is observed for high and lower fractions of ferrite/pearlite on both edges of M-NB (Figure 5.18C). It is observed that more local misorientation is present in the smaller grains with pearlite than in the bigger grains with ferrite even though some of these bigger grains appear to be deformed. Thus, it can be concluded that the KAM values are sensitive to the ferrite/pearlite ratio of Small α -Regions.

The KAM mapping of the M-HB-rib (hot bent) shows a large difference between the two major phases, which is interpreted as more local misorientation in the Small α -Region than in the Large α -Region regardless of deformation (Figure 5.23B). An increase in local misorientation approaching the surface in the Large α -Region is observed. However, this is unexpected as the hypothesis stated that minimal stored strain energy is expected in a hot bent sword as annealing would decrease this energy. This indicates that even after repeatedly annealing and hammering some strain is left inside the grains, possibly due to hammering as the last step in the cycle. For the upper surface with a Small α -Region, this phenomenon is not seen. For both phases, the last 100 μm to the surface is almost free of mislocations. This phenomenon is seen on a smaller scale around the major crack of M-HB-edge, the grains around the cracks are slightly larger and contain less local misorientation (Figure 5.23D). Might this indicate that defects/carbon might escape out of the lattice into the cracks? To answer this question is out of the scope of this thesis.

Lastly, the KAM mapping of the M-CB-rib (cold bent) presented interesting results as the compressed side (lower surface) shows a high concentration of local misorientation, even though this is part of the Large α -Region, the grains nearing the surface decrease in size and are deformed. This is in accordance with the theoretical hypothesis discussed above. The compressed side clearly shows the effects of deformation, even more so in the grain average misorientation (GAM) which shows that the gradual increase in the misorientation inside the grains nearing the compressed surface. The stretched microstructure does show an increase in misorientation, however, this is parallel to the change into a α_w -Region. Since the increase in misorientation is not very gradual, it could be considered a result of the change of phases instead of bending. The cutting edge of M-CB shows a stroke of lesser misorientation through the middle of the sword, suggesting a middle zone between the compressed and stretched microstructure. However, it should be debated whether this small stroke represents the entire sample as it is not clearly seen in the EBSD results of M-CB-rib. It could be a coincidence that a small stroke of a slightly different composition of microstructure with lower misorientation density runs through the centre of this edge.

Evaluating the EBSD data from the M-series, it is concluded that the cold bending of the sword can be detected in the microstructure with EBSD, regardless of the heterogeneity in phase composition. The plastic deformation is detected best at the compressed surface in the form of a gradual increase in strain (local misorientation), a decrease in grain size and the deformation of the grains with respect to the phase detected at that location. It is evident that the KAM values are sensitive to the change in grain size and phase and the presence of inclusions:

- The α_w -Regions have high concentrations of local misorientation in the coarse pearlite grains and a minimal concentration in the allotriomorphic and Widmanstätten ferrite grains.
- The Small α -Region seems to store local misorientation mainly in the small pearlite grains.
- The Large α -Region stores a minimal concentration of local misorientation in/around the grain boundaries.
- The grains around large inclusions/cracks appear slightly bigger than the average grain size of the current phase and they store less local misorientation.

This complicates the detection of plastic deformation in ancient objects due to their heterogeneous microstructure and high concentration of inclusions.

6.4.2. Was the Heythuysen Sword Bent by Brute Force?

Pieces H-8 is remarkably straight. The discussion of *how* the sword is bent can start with the evaluation if this piece is bent. The sword is not reconstructed, therefore the location and the position of piece H-8 in the sword is unknown. Since the piece is elongated, it can be assumed that it was positioned with the long side in the length of the sword and that specimen H-CS-8 shows the rib to the cutting edge.

EBSD measurements over the width of the cross-section (height of the sword), show slightly contradicting results. Near the rib, where a Small α -Region is dominant, the local misorientation is the lowest in the central line. This can indicate the presence of strain on either side of the central line. However, this must be questioned since this line emerges from the Large α -Region and thus exists predominantly of ferrite grains. Since, it was concluded that the KAM values are sensitive to the phases and thus the ferrite/pearlite ratio, this could certify the low KAM values in the central line. Furthermore, this central line with low misorientation does not cross through the entire H-CS-8 specimen. Therefore, the low misorientation in part of the central line does not provide valid evidence for the deformation of this piece of the Heythuysen sword.

Near the cutting edge, where the upper half of the microstructure exists of an α_w -Region and the lower half of a Small α -Region, the α_w -Region shows a significantly higher local misorientation than the small α -Region as described in Section 5.1.4. Here, the local misorientation is the highest in the central line of the cross-section, respectively to the present microstructure, and slightly decreases towards the surfaces. This is the opposite of what is seen near the rib and of what is expected of a brute-bent sword. This could be explained by the evidence that different phases appear to have various degrees of local misorientation, as discussed above.

Finally, it can be concluded that no evidence of plastic deformation is found in the specimen H-CS-8. Therefore, it can be said that specimen H-CS-8 was most likely not bent by brute force but by a blacksmith with a forge fire or was not bent at all. However, it is debatable whether this is representative of the entire sword as H-CS-8 is not clearly bent and the surface is heavily affected by corrosion, which may have undermined evidence of plastic deformation. Also, the possibility of brute force bending cannot be fully dismissed yet as our conclusion is based on the assumption that the sword was not on the cremation pyre. If this assumption is rejected and the sword was on the cremation pyre, a distinction between brute bending and blacksmith bending is hard to make.

If one assumes that all bent swords found in the Netherlands are bent in the same ritual and manner, one might suspect that the swords were bent by a blacksmith using a forge fire. The sword of Meerlo (Figure 2.14B) is bent/folded so sharply, that if this was done by brute force, these curves would have been broken before these sharp angles were reached. Only with the help of a smithing fire, these angles could be achieved. This sword was found in pieces, which might refute this argument. But all in all, it supports the argument that the Heythuysen sword was most likely bent by a blacksmith with a forge fire.

Part IV

Closure

Conclusion

General conclusions about the Heythuysen sword, the Domtoren and the mock-up sword are listed.

The Heythuysen sword has at least three microstructures:

- Large ferrite grains without carbides.
- Small ferrite grains with small pearlite grains and cementite in the grain boundaries.
- Coarse pearlite grains with allotriomorphic and Widmanstätten ferrite.

Assuming that the historical iron production theory is correct, it can be concluded that the blacksmith who made the Heythuysen sword knew carburisation techniques. On the other hand, water quenching was not the last phase-changing modification. The shape of the inclusions in the H-CS-8 support the historical sword production process, as described in Section 2.2.2. There are three types of inclusion observers in H-CS-8:

- Wüstite circles in a fayalite matrix existing in groups of small inclusions or large irregular shapes in Small α -Region metal phase.
- Singular strings of glass inclusions in α_w -Region metal phase.
- Strings of fine dot patterns in Small α -Region metal phase.

The slag inclusions have a high concentration of manganese. This suggests the use of bog iron ore for iron production. Based on the presence and location of the various microstructures, the measured carbon concentrations, the presence and location of various slag inclusions and NRC ratios, it is concluded that a combination of piling techniques and carburisation was most likely applied to the Heythuysen sword.

The Domtoren anchorages (D-1 and D-2) were most likely made from different iron ore and underwent different processing procedures. D-2 is a typical wrought iron with a carbon content of 0.018 wt% and D-1 is constructed with a piling technique, alternating carburised and not carburised iron. The anchorages most likely originate from the 14th century, the original construction of the Domtoren. The microstructure of D-1 is not a perfect match to represent the Heythuysen sword as a microstructural replica. However, the age and old production techniques of the anchorage and the arrangement of several phases are more similar to the ancient sword than contemporary steel and techniques.

The microstructure of the mock-up sword has no symmetry through the rib axes but does show consistency throughout the length of the sword. The reforging of D-1 into the M-series had an overall minimum effect on the composition of the slag inclusions. However, The forging of the mock-up sword slightly decarburised the iron.

How were Early Iron Age iron sword deliberately bent and how does the microstructure of the metal support the theory?

With the help of EBSD and the M-series bending experiment, it is evident that the brutal bending of a sword at outside temperature leaves traces of plastic deformation, such as an increase in local misorientations and deformations of the grain shape within a phase. When bending is performed with the help of a blacksmith and fire, the traces of plastic deformation are marginal. The local misorientation (KAM) values are sensitive to the presence of inclusions and the changes in grain size and phase. This

complicated the evaluation of the Heysthuysen sword. The results of H-CS-8 were inconsistent and did not provide strong evidence of plastic deformation. Therefore, this piece was most likely not bent by brute force but by a blacksmith with a forge fire or not at all. The possibility of brute force bending cannot be fully dismissed yet as our conclusion is based on the assumption that the sword was not on the cremation pyre. The general assessment of all swords in the “bent iron sword” category from the Hallstatt period in the Netherlands suggests that these swords are most likely bent with fire by a blacksmith.



Recommendations

It is wonderful to have studied a sample from a real Dutch bent iron sword. However, as described in the discussion, this piece is rather straight and not an optimal case to study bending. It would be desirable to take another sample from the same sword with a clear bent in order to compare this with H-CS-8 and form an even better conclusion about the treatment of the sword. Of course, this is an undesirable answer for possible future conservation and restoration of the Heythuysen sword. Moreover, it would be a challenge to retrieve a bent sample with minimal influence of external forces and embed it properly to handle the pieces. Further research in this direction should be carefully considered.

A safer route to study the metal microstructure is already mentioned in this thesis, neutron imaging and diffraction. These nondestructive techniques provide information on the microstructure within the objects without sample collection. This research will continue in this direction. The mock-up sword, the entire Heythuysen sword and part of the Wijchen sword will be measured. It would be recommended to compare and relate these results to the outcome of this thesis. This will indicate the accuracy of the nondestructive method with respect to the destructive method and might improve the understanding of results.

Swords are not the only iron object from the Hallstatt C period in the Netherlands. Multiple tools such as pins, rings and wheels are found in this category. No metallographic research on these objects has yet been performed. Therefore, it could be suggested that research on Iron objects from the Hallstatt C period in the Netherlands, in general, might deliver an interesting view of the origin, quality and use of the objects, the trade of iron objects, the production techniques and skills of these iron objects and the degradation of iron over millennia. Next to the techniques used in this thesis, research should include elemental analysis of the metal itself and precisely targeted hardness measurements.

References

- [1] S. Van der Vaart-Verschoof, *Fragmenting the chieftain: a practice-based study of Early Iron Age Hallstatt C elite burials in the Low Countries*. Sidestone Press, 2017.
- [2] B. Arnold, "Gender, temporalities, and periodization in early iron age west-central europe," *Social Science History*, vol. 36, no. 1, pp. 85–112, 2012. DOI: 10.1017/s0145553200010385.
- [3] H. Hildebrand, "Sur les commencements de l'âge du fer en europe," *Comptendu de la 7. session/Congrès International d'Anthropologie et d'Archéologie Préhistoriques: Stockholm, 1874*.
- [4] J. Haywood, *Atlas of the Celtic World*. Thames & Hudson, 2001.
- [5] "File:celts in europe.png," 2011-10-07. [Online]. Available: https://commons.wikimedia.org/wiki/File:Celts_in_Europe.png (visited on 12/29/2023).
- [6] P. Milcent, "Le premier âge du fer en france centrale," *Mémoires de la Société préhistorique française*, vol. 34, pp. 371–718, 2004.
- [7] D. Măndescu, "Killing the weapons. an insight on graves with destroyed weapons in late iron age transylvania," in *Iron Age Rites and Rituals in the Carpathian Basin. Proceedings of the International Colloquium from Târgu Mures*, 2012, pp. 343–356.
- [8] Z. Zetochová, "Intentional destruction of inventory in celtic warrior graves in the middle danube region," *Studia Historica Nitriensia*, vol. 23, no. SUPPL. Pp. 215–226, 2019. DOI: 10.17846/shn.2019.23.s.215-226.
- [9] R. Pleiner, *The Celtic Sword*. Oxford University Press, 1993.
- [10] N. Roymans, "Late urnfield societies in the northwest european plain and the expanding networks of central european hallstatt groups," in *Images of the past: studies on ancient societies in Northwestern Europe*, N. Roymans and F. Theuws, Eds. Instituut voor Pre-en Protohistorische Archeologie Amsterdam, 1991, pp. 8–89.
- [11] E. Theunissen, J. de Kort, E. Rensink, C. van Rooijen, and V. L.B.M., *Prehistorisch grafveld de Busjop bij Heythuysen weer zichtbaar* (Rapportage Archeologische Monumentenzorg). uNiek-Design, Almere, 2013, vol. 214.
- [12] L. Theunissen, T. de Groot, J. de Kort, and F. Laarmand, *Verstoord door schatgraverij* (Rapportage Archeologische Monumentenzorg). Xerox/OBT, Den Haag, 2021, vol. 270.
- [13] H. Fokkens and R. Jansen, *Het vorstengraf van Oss. Een archeologische speurtocht naar een prehistorisch grafveld*. Matrijs, Utrecht, 2004.
- [14] J. Nienhuis, "Artefact biography 2.0: The information value of corroded archaeological bronzes," Ph.D. dissertation, Delft University of Technology, 2017.
- [15] H. Fokkens, S. Van der Vaart, D. Fontijn, *et al.*, "Hallstatt burials of oss in context," in *The End of Our Fifth Decade*, C. Bakels and H. Kamermans, Eds., *Analecta Praehistorica Leidensia* 43/44. Leiden University Press, 2012, pp. 183–204.
- [16] K. Grömer, "Hallstatt period textile finds from the netherlands," in *Fragmenting the chieftain. Late Bronze and Early Iron Age elite burials in the Low Countries. Catalogue*, S. Van der Vaart-Verschoof, Ed. 2017, pp. 263–272.
- [17] K. Grömer, "Textiles as early iron age prestige goods—a discussion of visual qualities," in *Connecting elites and regions: Perspectives on contacts, relations and differentiation during the Early Iron Age Hallstatt C pe-riod in Northwest and Central Europe*, R. Schumann and S. Van der Vaart-Verschoof, Eds. 2017, pp. 221–236.

- [18] I. Joosten, M. van Bommel, R. Hofmann-de Keijzer, and H. Reschreiter, "Micro analysis on hallstatt textiles: Colour and condition," *Microchimica Acta*, vol. 155, pp. 169–174, 2006. DOI: 10.1007/s00604-006-0537-6.
- [19] P. Wells, *How ancient Europeans saw the world vision, patterns, and the shaping of the mind in prehistoric times*. Princeton University Press, 2012.
- [20] R. Meijers, "Restauratieverslag gac2013.14," Museum het Valkhof Nijmegen, kunst and archeologie. Unpublished report, 2013.
- [21] A. Marshall, in *Experimental Archaeology: 1. Early Bronze Age Cremation Pyres ; 2. Iron Age Grain Storage* (BAR British series), BAR British series. 2011, vol. 530, ch. Simulation of prehistoric cremation: experimental pyres, and their use for interpretation of archaeological structures, pp. 2–79.
- [22] R. Walker, "The production, microstructure, and properties of wrought iron," *Journal of chemical education*, vol. 79, no. 4, p. 443, 2002. DOI: 10.1021/ed079p443.
- [23] I. Joosten, "Technology of early historical iron production in the netherlands," Ph.D. dissertation, Vrije Universiteit Amsterdam, 2004.
- [24] J. Schlegel, *The World of Steel: On the History, Production and Use of a Basic Material*. Springer Wiesbaden, 2023.
- [25] P. Matteis and G. Scavino, "Mechanical performance of historical wrought iron rods," *Archaeometry*, vol. 61, no. 5, pp. 1053–1065, 2019. DOI: 10.1111/arcm.12470.
- [26] A. Williams, *The Sword and the Crucible: A History of the Metallurgy of European Swords up to the 16th Century*. Brill, 2012.
- [27] H. Tolboom and M. van Hunen, "Smeedijzer in the exterior: Beheer and onderhoud," *RCE Kennisbank*, 2022. [Online]. Available: https://kennis.cultureelerfgoed.nl/index.php/Smeedijzer_in_het_exterieur_-_beheer_en_onderhoud (visited on 12/28/2023).
- [28] M. C. Flemings and D. V. Ragone, "Puddling: A new look at an old process," *ISIJ international*, vol. 49, no. 12, pp. 1960–1966, 2009.
- [29] W. Chapma, *Workshop Technology, Part 1*, fifth. Routledge, 2011.
- [30] J. Sherby o.d.and Jeffrey Wadsworth, "Ancient blacksmiths, the iron age, damascus steels, and modern metallurgy," *Journal of Materials Processing Technology*, vol. 117, no. 3, pp. 347–353, 2001. DOI: [https://doi.org/10.1016/S0924-0136\(01\)00794-4](https://doi.org/10.1016/S0924-0136(01)00794-4).
- [31] J. Lang, "The technology of celtic iron swords," in *The Crafts of the Blacksmith, Essays Presented to R.F. Tylecote at the 1984 Symposium of the UISPP Comité Pour la Sidérurgie Ancienne Held in Belfast, N. Ireland, 16th - 21st September 1984*, 1987, pp. 61–72.
- [32] T. Read, "The early casting of iron: A stage in iron age civilization," *Geographical Review*, vol. 24, no. 4, pp. 544–554, 1934. DOI: 10.2307/208844.
- [33] W. Manning, "Ironworking in the celtic world," in *The Celtic World*, M. Green, Ed. 1995, pp. 310–320.
- [34] A. Velling, "Iron-carbon phase diagram explained," *Fractory*, 2020. [Online]. Available: <https://fractory.com/iron-carbon-phase-diagram/> (visited on 08/07/2023).
- [35] V. Buchwald and H. Wivel, "Slag analysis as a method for the characterization and provenancing of ancient iron objects," *Materials Characterization*, vol. 40, no. 2, pp. 73–96, 1998. DOI: [https://doi.org/10.1016/S1044-5803\(97\)00105-8](https://doi.org/10.1016/S1044-5803(97)00105-8).
- [36] P. Polybius, S. D. Olson, and W. R. Paton, in *The histories volume vi : books 28-39. fragments*. Harvard University Press, 2012, ch. book 39.
- [37] J. Lang, "Study of the metallography of some roman swords," *Britannia*, vol. 19, pp. 199–216, 1988. DOI: 10.2307/526199.
- [38] J. Lang and A. Williams, "The hardening of iron swords," *Journal of Archaeological Science*, vol. 2, no. 3, pp. 199–207, 1975. DOI: 10.1016/0305-4403(75)90057-6.

- [39] G. Langford, "Microstructures: Low alloy steels, lesson 1, seventh specimen," 2005, Accessed: 2024-01-10. [Online]. Available: <https://www.georgesbasement.com/Microstructures/LowAlloySteels/Lesson-1/Specimen07.htm>.
- [40] L. Murr, E. Trillo, A. Bujanda, and N. Martinez, "Comparison of residual microstructures associated with impact craters in fcc stainless steel and bcc iron targets: The microtwin versus microband issue," *Acta Materialia*, vol. 50, no. 1, pp. 121–131, 2002. DOI: 10.1016/S1359-6454(01)00334-2.
- [41] A. Kelly, "Neumann bands in pure iron," *Proceedings of the Physical Society. Section A*, vol. 66, no. 4, pp. 403–405, 1953. DOI: 10.1088/0370-1298/66/4/312.
- [42] J. Lang, "Iron tyres from iron age burials at wetwang, yorkshire," *Historical Metallurgy*, vol. 48, no. 1 & 2, pp. 8–15, 2014.
- [43] J. Jiménez, E. Bravo, A. Criado, *et al.*, "A new method for dating ancient steel samples using vickers microhardness," *Materials Characterization*, vol. 52, no. 2, pp. 145–151, 2004. DOI: <https://doi.org/10.1016/j.matchar.2004.04.005>.
- [44] L. García, A. Criado, G. Queirós, J. Meseguer-Sánchez, J. de Salazar, and A. Criado, "Pearlitic morphologies found in carbon steel artefacts more than 2,000 years old," *Journal of Material Sciences & Manufacturing Research.*, vol. 143, pp. 2–7, 2022. DOI: doi.org/10.47363/JMSMR/2022.
- [45] B. M. E., J. Fernández, J. Arasanz, *et al.*, "Archaeologic analogues: Microstructural changes by natural ageing in carbon steels," *Journal of Nuclear Materials*, vol. 349, no. 1, pp. 1–5, 2006. DOI: <https://doi.org/10.1016/j.jnucmat.2005.06.022>.
- [46] G. Queiros, L. García, T. de la Fuente, J. de Salazar, and A. Criado, "Metallographic interpretation of the morphology of the very old pearlite," *Archives of Physics Research*, vol. 10, no. 1, pp. 42–51, 2019.
- [47] A. Thiele and J. Hošek, "Estimation of phosphorus content in archaeological iron objects by means of optical metallography and hardness measurements," *Acta Polytechnica Hungarica*, vol. 12, no. 4, pp. 113–126, 2015.
- [48] A. Pense, "Iron through the ages," *Materials Characterization*, vol. 45, no. 4-5, pp. 353–363, 2000. DOI: 10.1016/S1044-5803(00)00105-4.
- [49] C. Mori, G. Ghiara, P. De Montis, P. Piccardo, G. Gatta, and S. Trasatti, "Archaeometallurgical analyses on two renaissance swords from the "luigi marzoli" museum in brescia: Manufacturing and provenance," *Heritage*, vol. 4, no. 3, pp. 1269–1283, 2021. DOI: 10.3390/heritage4030069.
- [50] K. Bhadeshia, *Theory of Transformations in Steels*. CRC Press, 2021.
- [51] A. Criado, L. García, A. Criado, and J. Salazar, "Typical morphologies of iron carbides in pieces of preromans steel submitted to rites of incineration in the iberian peninsula," *International Journal of Recent Scientific Research*, vol. 6, pp. 7844–7848, Dec. 2015.
- [52] H. K. D. H. Bhadeshia, *Interpretation of the microstructure of steels*, 2008. [Online]. Available: http://cml.postech.ac.kr/2008/Steel_Microstructure/SM2.html (visited on 05/12/2024).
- [53] M. Caruso and S. Godet, "Microstructural evolution during spheroidization annealing of eutectoid steel: Effect of interlamellar spacing and cold working," in *THERMEC 2009 Supplement*, ser. Advanced Materials Research, vol. 89, Trans Tech Publications Ltd, Feb. 2010, pp. 79–84. DOI: 10.4028/www.scientific.net/AMR.89-91.79.
- [54] J.-J. Sun, F.-L. Lian, H.-J. Liu, *et al.*, "Microstructure of warm rolling and pearlitic transformation of ultrafine-grained gcr15 steel," *Materials Characterization*, vol. 95, pp. 291–298, 2014. DOI: <https://doi.org/10.1016/j.matchar.2014.07.011>.
- [55] G. Ghiara, P. Piccardo, S. Campodonico, and M. Carnasciali, "Microstructural features in corroded celtic iron age sword blades," *JOM*, vol. 66, pp. 793–801, 2014.
- [56] M. L'Héritier, S. Leroy, P. Dillmann, and B. Gratuze, "Characterization of slag inclusions in iron objects," in *Recent Advances in Laser Ablation ICP-MS for Archaeology*. Springer, 2016, pp. 213–228. DOI: 10.1007/978-3-662-49894-1.

- [57] M. Joseph and M. Jabbar, "Effect of aging process on the microstructure, corrosion resistance and mechanical properties of stainless steel aisi 204," *Case Studies in Construction Materials*, vol. 11, e00253, 2019. DOI: <https://doi.org/10.1016/j.cscm.2019.e00253>.
- [58] *De domtoren: Een tijdlijn*, 2024. [Online]. Available: <https://www.domtoren.nl/het-verhaal/tijdlijn/> (visited on 02/09/2024).
- [59] L. Saraf, "Kernel Average Misorientation Confidence Index Correlation from FIB Sliced Ni-Fe-Cr alloy Surface," *Microscopy and Microanalysis*, vol. 17, no. S2, pp. 424–425, 2011. DOI: 10.1017/S1431927611002996.
- [60] F. Frank and P. K.E., "Cementite morphology in pearlite," *Acta Metallurgica*, vol. 4, no. 2, pp. 206–210, 1956. DOI: [https://doi.org/10.1016/0001-6160\(56\)90140-7](https://doi.org/10.1016/0001-6160(56)90140-7).
- [61] H. Bhadeshia, *Theory of transformations in steels*. CRC Press, 2021.
- [62] J. Moravec, M. Mičian, M. Málek, and M. Švec, "Determination of cct diagram by dilatometry analysis of high-strength low-alloy s960mc steel," *Materials*, vol. 15, no. 13, 2022. DOI: 10.3390/ma15134637. [Online]. Available: <https://www.mdpi.com/1996-1944/15/13/4637>.
- [63] E. Blakelock and G. McDonnell, "A review of metallographic analyses of early medieval knives," *Historical metallurgy*, vol. 41, no. 1, pp. 40–56, 2007.
- [64] Y. Xue, C. Tian P.and Li, D. Zhao, and S. Wang, "Reduction mechanism of p_2o_5 in steel slag," *Trans Indian Inst Met*, vol. 73, pp. 251–258, 2020. DOI: <https://doi.org/10.1007/s12666-019-01829-3>.
- [65] S. Wright, J. Kacher, and T. Ruggles, "Electron backscatter diffraction based strain analysis in the scanning electron microscope.," Sandia National Lab.(SNL-NM), Albuquerque, NM (United States), Tech. Rep., 2021.
- [66] D. Mannes and E. Lehmann, "Neutron imaging of cultural heritage objects," in *Handbook of Cultural Heritage Analysis*, S. D'Amico and V. Venuti, Eds. Springer International Publishing, 2022, pp. 211–237. DOI: 10.1007/978-3-030-60016-7_9.
- [67] M. Strobl, N. Manke I.and Kardjilov, A. Hilger, M. Dawson, and J. Banhart, "Advances in neutron radiography and tomography," *Journal of Physics D: Applied Physics*, vol. 42, no. 24, p. 234 001, Dec. 2009. DOI: 10.1088/0022-3727/42/24/243001.
- [68] J. Radon, "On the determination of functions from their integral values along certain manifolds," *IEEE Transactions on Medical Imaging*, vol. 5, no. 4, pp. 170–176, 1986. DOI: 10.1109/TMI.1986.4307775.
- [69] F. Salvemini, F. Grazzi, N. Kardjilov, *et al.*, "Non-invasive characterization of ancient indonesian kris through neutron methods," *The European Physical Journal Plus*, vol. 135, pp. 1–25, 2020. DOI: 10.1140/epjp/s13360-020-00452-2.
- [70] F. Salvemini, F. Grazzi, S. Peetermans, M. Gener, E. Lehmann, and M. Zoppi, "Characterization of european sword blades through neutron imaging techniques," *The European Physical Journal Plus*, vol. 129, pp. 1–8, 2014. DOI: 10.1140/epjp/i2014-14202-4.
- [71] F. Grazzi, F. Cantini F.and Salvemini, A. Scherillo, *et al.*, "The investigation of indian and central asian swords through neutron methods," *Journal of Archaeological Science: Reports*, vol. 20, pp. 834–842, 2018. DOI: 10.1016/j.jasrep.2018.06.010.
- [72] F. Grazzi, L. Bartoli, F. Civita, A. Paradowska, A. Scherillo, and M. Zoppi, "Non destructive characterization of phase distribution and residual strain/stress map of two ancient (koto) age japanese swords," *Materials Science Forum*, vol. 652, pp. 167–173, 2010. DOI: 10.4028/www.scientific.net/msf.652.167.
- [73] B. D. Cullity, *Elements of X-ray Diffraction*. Addison-Wesley Publishing, 1956.
- [74] F. Grazzi, L. Bartoli, F. Civita, *et al.*, "From koto age to modern times: Quantitative characterization of japanese swords with time of flight neutron diffraction," *Journal of Analytical Atomic Spectrometry*, vol. 26, no. 5, pp. 1030–1039, 2011. DOI: 10.1039/c0ja00238k.

- [75] F. Grazzi, F. Civita, A. Williams, *et al.*, “Ancient and historic steel in japan, india and europe, a non-invasive comparative study using thermal neutron diffraction,” *Analytical and bioanalytical chemistry*, vol. 400, no. 5, pp. 1493–1500, 2011. DOI: 10.1007/s00216-011-4854-1.
- [76] E. Barzagli, F. Grazzi, A. Williams, *et al.*, “Characterization of an indian sword: Classic and noninvasive methods of investigation in comparison,” *Applied Physics A*, vol. 119, no. 1, pp. 97–105, 2015. DOI: 10.1007/s00339-014-8968-0.
- [77] F. Grazzi, M. Celli, S. Siano, and M. Zoppi, “Preliminary results of the italian neutron experimental station ines at isis: Archaeometric applications,” *NCimC*, vol. 30, no. 1, pp. 59–65, 2007. DOI: 10.1393/ncc/i2006-10039-5.
- [78] A. Botti, M. Ricci, G. De Rossi, W. Kockelmann, and A. Sodo, “Methodological aspects of sans and tof neutron diffraction measurements on pottery: The case of miseno and cuma,” *Journal of Archaeological Science*, vol. 33, no. 3, pp. 307–319, 2006. DOI: <https://doi.org/10.1016/j.jas.2005.06.016>.



Summary of Results

	H-CS-8	D-1	D-2	M-NB	M-HB	M-CB
Microstructures	Multiple: Large α -Regions, Small α -Regions and α_w -Regions	Multiple: Large α -Regions, Small α -Regions, Pearlite and α_w -Regions	One: Large α -Regions	Multiple: Small α -Regions, Pearlite and α_w -Regions	Multiple: Large α -Regions, Small α -Regions and α_w -Regions	Multiple: Large α -Regions, Small α -Regions, Pearlite and α_w -Regions
Main phases	Small α -Region	Pearlite Region, Large α -Region	n/a	Small α -Region	Large α -Region, Small α -Region	Large α -Region, α_w -Region
Layering pattern (piling)	Piling suggested	Clear pattern, piling technique was applied	n/a	n/a	Large inclusion network separating the main phases	Large inclusion network separating the main phases
Large α-Region	No carbides, average grain size 100 μm	Small carbides (dots/needles), cementite at grain boundaries, grain size 30-100 μm	No carbides, average grain size 130 μm	n/a	No carbides, grain size 20-150 μm	Cementite in grain boundaries, minor small carbides, grain size 30-80 μm
Small α-Region	Cementite in grain boundaries, small carbides in ferrite, average grain size 15 μm	Elongated grains, resemble dominant α_w and α_{alt} , grain size 10-20 μm	n/a	Gradients in the ferrite/pearlite ratio, relatively low ratio, average grain size 10 μm	Cementite in grain boundaries, grain size 5-15 μm	Grain size 10-30 μm
α_w-Regions	High cementite density near ferrite-pearlite grain boundaries, extreme fragmentation of cementite in grain core	Higher cementite density, more evident cementite spheres, cementite sphere form subgrain boundaries	n/a	High cementite density both (not)-fragmented, more α_{alt} than α_w ferrite	Tiny cementite spheres form subgrain-boundaries, with various cementite density/fragmentation.	High cementite density both (not)-fragmented, darker grains with faint film formation
Pearlite Region	n/a	Variations in inter-lamellar spacing and degree of fragmentation (independent of subgrains or pearlite colonies)	n/a	Wide variety of cementite shapes: small films, large laths, spheres in various sizes, darker grains with faint film formation	n/a	Patches of different grey tones, with and without cementite features
α-Region	n/a	n/a	n/a	Cementite in grain boundaries, grain size 10-30 μm	n/a	n/a

Table A.1: Summary of all observed microstructures.

	H-CS-8	D-1	D-2	M-NB	M-HB	M-CB
General orientation slag inclusions	Width of the sword	Width of the anchorage	n/a	Width of the sword	Width of the sword	Width of the sword
Slag inclusion	Wüstite in a fayalite matrix, groups of small inclusions or large irregular shapes, Small α metal phases	Wüstite in fayalite matrix, irregular shaped	Wüstite laths and dendritic circular shapes in fayalite matrix	Strings of glass(y) slag, α_w , α , Small α - metal phases	Small glassy inclusion close to the cracks, Small α metal phases	Wüstite in matrix, major strings and surrounding small inclusions
Slag inclusion	Singular strings of glassy inclusions, α_w metal phases	Strings of glass inclusions, α_w and Pearlite metal phases	Strings of fine dot patterns, glassy. + Fine line pattern, element concentrations resemble fayalite	Strings of fine line pattern, glassy, Small α metal phase	Strings with fine dot/line pattern, glassy, Small α - and Large α - metal phases	Strings or groups of small inclusions, glass or glassy inclusions in Pearlite-, α_w - and Large α - metal phases
Slag inclusion	Strings of fine dot patterns, Small α metal phases	Strings of fine dot patterns, Large α metal phases	Wüstite laths in matrix	n/a	Large irregular inclusion with various particles, fayalite, unique	Major strings with fine dot pattern, Small α
NRC ratio	3 categories	All similar, distinction between the presence of Na ₂ O and TiO ₂ or P ₂ O ₅ and SO ₃	Extremely fluctuating	Similar to D-1, 2 categories	Similar to D-1, expect the inclusion with various particles	Glass(y) inclusion are similar to D-1, the Major strings are have different NRC values
Notable elements	Relative high manganese	Relatively high aluminium	Relatively high phosphorous	Similar to D-1	Silimar to D-2	Silimar to D-3

Table A.2: Summary of all Slag Inclusions.

B

Slag Inclusions: Elemental composition

Table B.1: Specimen H-CS-8, results on elemental composition in slag inclusions.

Circles + Matrix (measured) (Wüstite-Glass)		wt%											ratio		
Placement	Shape	FeO	SiO ₂	CaO	MnO	K ₂ O	Al ₂ O ₃	MgO	Na ₂ O	P ₂ O ₅	Cl	C	SiO ₂ /FeO	SiO ₂ /CaO	
Upper middle	Big group, small inclusions	60.1	25.9	2.4	7.1	n/a	n/a	2.0	n/a	n/a	n/a	2.5	0.4	11.0	
Upper middle	Big group, small inclusions	60.9	25.9	2.5	6.1	n/a	n/a	1.1	n/a	n/a	n/a	3.5	0.4	10.4	
Upper middle	Big group, small inclusions	60.5	26.3	2.7	6.5	n/a	n/a	1.0	n/a	n/a	n/a	3.0	0.4	9.8	
Lower rib	Big group, small inclusions	59.8	24.5	3.0	8.3	n/a	n/a	1.1	n/a	n/a	n/a	3.3	0.4	8.1	
Lower rib	Big group, small inclusions	54.7	26.6	6.2	7.8	n/a	n/a	0.9	n/a	n/a	n/a	4.0	0.5	4.3	
Lower rib	Big group, small inclusions	56.3	27.2	2.0	8.8	n/a	n/a	2.1	n/a	n/a	n/a	3.1	0.5	13.6	
Lower rib	Large irregular shape	80.0	9.7	1.9	5.2	n/a	n/a	0.8	n/a	n/a	n/a	2.5	0.1	5.1	
Lower rib	Large irregular shape	76.8	9.5	2.0	5.3	n/a	n/a	0.7	n/a	n/a	n/a	5.7	0.1	4.8	
Upper middle	Large irregular shape	64.2	16.5	7.2	6.3	1.0	0.4	0.6	n/a	1.6	n/a	2.3	0.3	2.3	
Circles (measured) + Matrix (Wüstite-Glass)		wt%											ratio		
Placement	Shape	FeO	SiO ₂	CaO	MnO	K ₂ O	Al ₂ O ₃	MgO	Na ₂ O	P ₂ O ₅	Cl	C	SiO ₂ /FeO	SiO ₂ /CaO	
Upper middle	Big group, small inclusions	95.6	n/a	n/a	2.6	n/a	n/a	n/a	n/a	n/a	n/a	1.7	n/a	n/a	
Upper middle	Big group, small inclusions	96.2	n/a	n/a	2.1	n/a	n/a	n/a	n/a	n/a	n/a	1.7	n/a	n/a	
Lower rib	Big group, small inclusions	94.8	n/a	n/a	2.7	n/a	n/a	n/a	n/a	n/a	n/a	2.5	n/a	n/a	
Lower rib	Big group, small inclusions	97.1	n/a	n/a	2.9	n/a	n/a	n/a	n/a	n/a	n/a	n/a	n/a	n/a	
Lower rib	Large irregular shape	95.0	n/a	n/a	3.6	n/a	n/a	n/a	n/a	n/a	n/a	1.4	n/a	n/a	
Lower rib	Large irregular shape	94.4	n/a	n/a	3.7	n/a	n/a	n/a	n/a	n/a	n/a	1.9	n/a	n/a	
Lower rib	Large irregular shape	94.5	n/a	n/a	3.6	n/a	n/a	n/a	n/a	n/a	n/a	1.9	n/a	n/a	
Upper middle	Large irregular shape	94.6	0.5	n/a	3.8	n/a	n/a	n/a	n/a	n/a	n/a	1.1	n/a	n/a	
Upper middle	Large irregular shape	96.1	n/a	n/a	3.8	n/a	n/a	n/a	n/a	0.1	n/a	n/a	n/a	n/a	
Homogenous (Glass)		wt%											ratio		
Placement	Shape	FeO	SiO ₂	CaO	MnO	K ₂ O	Al ₂ O ₃	MgO	Na ₂ O	P ₂ O ₅	Cl	C	SiO ₂ /FeO	SiO ₂ /CaO	
Lower middle	Irregular shape (singular)	2.5	54.9	22.5	3.6	6.6	2.7	2.3	n/a	n/a	n/a	4.8	22	2.4	
Upper cutting edge	String (singular)	4.6	59.0	12.4	11.3	3.7	2.6	1.8	0.4	n/a	n/a	4.3	13	4.8	
Lower middle	String (singular)	16.3	52.5	14.3	4.8	1.8	3.3	1.6	n/a	n/a	1.3	4.1	3.2	3.7	
Lower middle	Big irregular shape	11.2	50.0	21.7	5.4	1.6	3.1	2.5	n/a	n/a	0.5	3.9	4.4	2.3	
Fine pattern (Glassy)		wt%											ratio		
Placement	Shape	FeO	SiO ₂	CaO	MnO	K ₂ O	Al ₂ O ₃	MgO	Na ₂ O	P ₂ O ₅	Cl	C	SiO ₂ /FeO	SiO ₂ /CaO	
Upper cutting edge	Long string (singular)	19.3	49.0	11.6	9.1	3.1	2.4	2.3	n/a	n/a	n/a	3.3	2.5	4.2	
Upper cutting edge	Long string (singular)	14.1	49.5	13.6	10.9	2.1	1.6	3.0	n/a	n/a	n/a	5.3	3.5	3.6	
Upper cutting edge	Long string (singular)	24.8	42.5	12.8	10.5	1.7	1.4	2.7	n/a	n/a	n/a	3.7	1.7	3.3	

Table B.2: Specimen D-1, results on elemental composition in slag inclusions.

Enormous homogenous inclusion (Glass)													wt%				Ratio			
Shape	Metal Phase	FeO	SiO ₂	CaO	MnO	K ₂ O	Al ₂ O ₃	MgO	Na ₂ O	P ₂ O ₅	SO ₃	TiO ₂	C	SiO ₂ /FeO	SiO ₂ /Al ₂ O ₃					
long strings (group)	Pearlite Region	1.8	65.0	7.8	3.4	4.5	9.9	1.9	0.2	n/a	n/a	0.5	6.4	35.3	6.5					
long strings (group)	Pearlite Region	1.8	66.3	7.7	3.4	4.6	9.8	1.8	0.4	n/a	n/a	0.5	6.0	36.5	6.7					
Homogenous (Glass)													Ratio							
Shape	Metal Phase	FeO	SiO ₂	CaO	MnO	K ₂ O	Al ₂ O ₃	MgO	Na ₂ O	P ₂ O ₅	SO ₃	TiO ₂	C	SiO ₂ /FeO	SiO ₂ /Al ₂ O ₃					
long strings (group)	α _w Region	2.0	63.5	6.3	2.3	5.8	11.2	2.2	0.4	n/a	n/a	n/a	2.6	32.2	5.7					
long strings (group)	α _w Region	4.4	62.9	5.5	2.0	5.5	11.4	2.1	0.4	n/a	n/a	n/a	n/a	14.4	5.5					
Fine pattern (dots) / Homogeneous													Ratio							
Shape	Metal Phase	FeO	SiO ₂	CaO	MnO	K ₂ O	Al ₂ O ₃	MgO	Na ₂ O	P ₂ O ₅	SO ₃	TiO ₂	C	SiO ₂ /FeO	SiO ₂ /Al ₂ O ₃					
long strings homogeneous (small group)	Large α Region (carbides)	51.0	28.6	4.8	2.2	2.9	4.5	0.9	n/a	1.9	0.6	n/a	5.0	0.6	6.3					
long strings homogeneous (small group)	Large α Region (carbides)	50.0	30.4	5.6	2.2	2.9	4.9	1.0	n/a	1.9	0.7	0.5	3.6	0.6	6.2					
long sting fine pattern	Large α Region (carbides)	44.1	33.3	5.4	2.4	3.0	5.4	1.2	n/a	1.6	0.9	n/a	2.8	0.8	6.1					
long sting fine pattern	Large α Region (carbides)	42.1	32.9	5.2	2.4	2.4	5.5	0.9	n/a	1.7	1.0	n/a	5.9	0.8	6.0					
long sting homogeneous	Large α Region (carbides)	49.8	31.4	5.0	2.1	2.9	5.2	1.1	n/a	1.8	0.8	n/a	n/a	0.6	6.1					
long sting homogeneous	Large α Region (carbides)	47.1	30.6	4.5	2.2	2.5	5.0	1.0	n/a	1.9	0.7	n/a	4.5	0.6	6.1					
(Dentritic) Circles (measured) + Matrix (Glass-Wüstite)													Ratio							
Shape	Metal Phase	FeO	SiO ₂	CaO	MnO	K ₂ O	Al ₂ O ₃	MgO	Na ₂ O	P ₂ O ₅	SO ₃	TiO ₂	C	SiO ₂ /FeO	SiO ₂ /Al ₂ O ₃					
Irregular shape, bubble	Large α Region (carbides)	72.8	16.0	1.8	1.1	1.2	2.7	n/a	n/a	1.1	n/a	n/a	3.2	0.2	5.9					
Irregular shape, dentritic bubble	Large α Region (carbides)	78.8	11.8	1.3	1.0	0.7	1.9	0.4	n/a	0.6	n/a	n/a	3.4	0.1	6.3					
Irregular shape, dentritic bubble	Large α Region (carbides)	68.2	18.6	1.9	1.1	1.2	3.2	0.9	n/a	1.1	n/a	n/a	3.9	0.3	5.8					
(Dentritic) Bubbles + Matrix (measured) (Glass-Wüstite)													Ratio							
Shape	Metal Phase	FeO	SiO ₂	CaO	MnO	K ₂ O	Al ₂ O ₃	MgO	Na ₂ O	P ₂ O ₅	SO ₃	TiO ₂	C	SiO ₂ /FeO	SiO ₂ /Al ₂ O ₃					
Irregular shape (singular)	Large α Region (carbides)	58.1	25.4	3.2	1.4	1.6	4.0	0.8	n/a	1.4	0.9	n/a	3.2	0.4	6.4					
Irregular shape (singular)	Large α Region (carbides)	49.9	29.1	4.0	1.6	2.0	4.8	0.8	n/a	1.7	1.4	n/a	4.9	0.6	6.1					
Irregular shape (singular)	Large α Region (carbides)	53.2	28.5	3.4	1.6	1.7	4.3	0.8	n/a	1.7	0.8	n/a	4.0	0.5	6.7					

Table B.3: Specimen D-2, results on elemental composition in slag inclusions. D-2 only has a Large α - Region.

Dendritic cicles + Lath + Matrix (wüstite-fayalite)													
Type of Inclusion	wt%										ratio		
	FeO	SiO ₂	CaO	MnO	K ₂ O	Al ₂ O ₃	MgO	P ₂ O ₅	SO ₃	TiO ₂	C	SiO ₂ /FeO	SiO ₂ /Al ₂ O ₃
Dendritic bubble, laths, matrix	93.7	1.2	0.4	n/a	n/a	1.2	n/a	0.9	0.6	0.5	1.6	0.0	1.0
Dendritic bubble, laths, matrix	83.9	4.7	0.6	n/a	0.2	5.1	n/a	2.3	0.7	0.8	1.7	0.1	0.9
Dendritic bubble, laths, matrix	79.7	9.4	0.5	1.1	n/a	4.0	0.6	4.4	n/a	0.4	n/a	0.1	2.4
Dendritic bubble, laths, matrix	63.1	20.7	0.3	1.9	n/a	0.6	1.3	9.8	n/a	n/a	2.3	0.3	32.8
Dendritic bubble, laths, matrix	63.8	20.3	n/a	1.7	n/a	0.7	1.5	9.6	n/a	n/a	2.4	0.3	27.4
Dendritic bubble, laths, matrix	53.9	17.9	3.8	1.7	2.9	5.6	0.8	11.7	n/a	n/a	1.9	0.3	3.2
Dendritic bubble, laths, matrix	66.9	5.7	0.9	0.8	0.9	20.1	n/a	3.0	0.8	0.9	n/a	0.1	0.3
Laths + matrix (wüstite-fayalite)													
Type of Inclusion	wt%										ratio		
	FeO	SiO ₂	CaO	MnO	K ₂ O	Al ₂ O ₃	MgO	P ₂ O ₅	SO ₃	TiO ₂	C	SiO ₂ /FeO	SiO ₂ /Al ₂ O ₃
laths, matrix	54.6	15.5	2.6	1.5	2.3	3.8	0.5	15.3	1.3	n/a	2.5	0.3	4.0
laths, matrix	81.0	6.7	n/a	0.7	n/a	4.7	n/a	2.9	n/a	1.2	2.8	0.1	1.4
laths, matrix	70.9	11.2	0.5	1.0	0.7	6.3	0.5	6.5	n/a	0.6	2.0	0.2	1.8
laths, matrix	73.5	7.6	0.9	0.8	0.4	7.0	n/a	3.8	2.1	1.1	3.0	0.1	1.1
laths, matrix	71.1	9.3	1.2	1.1	0.5	6.2	0.6	5.3	n/a	1.3	3.6	0.1	1.5
Homogenous (fine dot pattern)													
Type of Inclusion	wt%										ratio		
	FeO	SiO ₂	CaO	MnO	K ₂ O	Al ₂ O ₃	MgO	P ₂ O ₅	SO ₃	TiO ₂	C	SiO ₂ /FeO	SiO ₂ /Al ₂ O ₃
Homogenous (fine dot pattern)	44.5	23.8	3.6	2.9	2.1	5.9	1.3	14.7	1.3	n/a	n/a	0.5	4.1
Fine pattern (lines)													
Type of Inclusion	wt%										ratio		
	FeO	SiO ₂	CaO	MnO	K ₂ O	Al ₂ O ₃	MgO	P ₂ O ₅	SO ₃	TiO ₂	C	SiO ₂ /FeO	SiO ₂ /Al ₂ O ₃
Fine pattern (lines)	60.9	13.5	2.0	1.4	1.0	4.6	0.6	12.5	1.7	n/a	1.9	0.2	3.0
Fine pattern (lines)	60.6	14.1	1.8	1.5	0.9	4.6	0.6	12.0	1.5	0.4	2.0	0.2	3.1

Table B.4: Specimen M-NB, results on elemental composition in slag inclusions.

Homogenous (glassy)																
Shape	Metal Phase	wt%											ratio			
		FeO	SiO ₂	CaO	MnO	K ₂ O	Al ₂ O ₃	MgO	Na ₂ O	P ₂ O ₅	SO ₃	TiO ₂	Cl	C	SiO ₂ /FeO	SiO ₂ /Al ₂ O ₃
Strings (group)	Small α Region	3.3	63.5	8.1	4.2	4.8	10.5	1.8	0.3	n/a	n/a	0.5	n/a	3.1	19.5	6.1
Strings (group)	Small α Region	5.0	62.1	8.2	4.5	4.5	10.0	2.0	n/a	n/a	n/a	0.7	n/a	3.1	12.5	6.2
String (group) (Fig. 5.14E)	α Region	24.7	43.1	9.9	3.2	3.2	7.4	0.8	n/a	0.6	0.5	0.4	n/a	6.2	1.7	5.9
String (group) (Fig. 5.14E)	α Region	12.0	55.3	8.7	3.3	4.7	9.3	1.8	n/a	n/a	n/a	0.5	n/a	4.3	4.6	5.9
Irregular shape (group) (Fig. 5.14E)	Small α Region	38.0	36.5	6.1	2.3	0.7	6.6	0.8	n/a	0.8	1.9	0.4	1.3	4.6	1.0	5.6
Irregular shape (group) (Fig. 5.14E)	Small α Region	39.3	37.2	4.3	2.3	0.4	6.3	1.8	n/a	1.0	1.2	0.4	0.5	5.2	0.9	5.9
Fine line pattern																
Shape	Metal Phase	wt%											ratio			
		FeO	SiO ₂	CaO	MnO	K ₂ O	Al ₂ O ₃	MgO	Na ₂ O	P ₂ O ₅	SO ₃	TiO ₂	Cl	C	SiO ₂ /FeO	SiO ₂ /Al ₂ O ₃
String singular	Small α Region	54.8	29.1	2.5	1.4	2.0	6.9	0.6	n/a	n/a	0.6	n/a	n/a	2.1	0.5	4.2
String singular	Small α Region	54.2	29.4	2.5	1.4	2.0	7.2	0.8	n/a	n/a	0.6	n/a	n/a	2.0	0.5	4.1

Table B.5: Specimen M-HB, results on elemental composition in slag inclusions.

Various particles		wt%														ratio		
Specimen	Metal Phase	FeO	SiO ₂	CaO	MnO	K ₂ O	Al ₂ O ₃	MgO	Na ₂ O	P ₂ O ₅	SO ₃	TiO ₂	C	Cl	SiO ₂ /FeO	SiO ₂ /Al ₂ O ₃		
Rib	Small α Region	69.9	25.4	0.9	1.4	n/a	0.5	0.3	n/a	n/a	n/a	n/a	1.6	n/a	0.4	56.5		
Rib	Small α Region	70.4	24.6	1.0	1.4	n/a	0.6	0.4	n/a	n/a	n/a	n/a	1.6	n/a	0.3	39.7		
Rib	Small α Region	68.5	26.4	0.9	1.6	n/a	0.4	0.6	n/a	n/a	n/a	n/a	1.6	n/a	0.4	67.8		
Rib	Small α Region	80.0	15.6	0.6	1.1	n/a	0.4	0.4	n/a	n/a	n/a	n/a	1.9	n/a	0.2	39.0		
Rib	Small α Region	76.2	18.9	0.8	1.1	n/a	0.5	n/a	n/a	n/a	n/a	n/a	2.5	n/a	0.2	42.1		
Rib	Small α Region	74.5	20.0	0.9	1.2	n/a	0.4	0.5	n/a	n/a	n/a	n/a	2.6	n/a	0.3	52.7		
Rib	Small α Region	71.9	22.8	0.8	1.3	n/a	0.3	0.8	n/a	n/a	n/a	n/a	2.1	n/a	0.3	66.9		
Homogeneous (glassy)		wt%														ratio		
Specimen	Metal Phase	FeO	SiO ₂	CaO	MnO	K ₂ O	Al ₂ O ₃	MgO	Na ₂ O	P ₂ O ₅	SO ₃	TiO ₂	C	Cl	SiO ₂ /FeO	SiO ₂ /Al ₂ O ₃		
Rib (group)	Small α Region	6.8	62.8	7.9	3.2	3.8	9.7	1.9	n/a	n/a	n/a	0.5	3.3	n/a	9.2	6.4		
Rib (group)	Small α Region	6.5	63.7	7.8	3.3	4.3	9.4	1.8	n/a	n/a	n/a	0.5	2.7	n/a	9.8	6.8		
Rib (group)	Small α Region	7.9	61.7	8.2	3.1	4.1	9.5	1.7	0.4	n/a	n/a	0.5	2.9	n/a	7.9	6.5		
Rib	Small α Region	13.9	57.3	7.0	3.5	3.9	9.4	1.3	n/a	n/a	n/a	0.5	3.1	n/a	4.1	6.1		
Rib	Small α Region	14.9	55.4	7.6	4.1	4.2	8.8	1.7	0.3	n/a	n/a	0.6	2.5	n/a	3.7	6.3		
Edge	Small α Region	10.9	60.8	4.7	3.2	4.3	10.2	1.3	0.4	n/a	n/a	0.5	3.8	n/a	5.6	6.0		
Edge	Small α Region	16.7	54.9	5.4	4.1	3.6	9.1	1.4	0.3	n/a	0.7	0.4	3.5	n/a	3.3	6.0		
Edge	Small α Region	12.4	55.5	8.5	4.3	4.6	9.4	1.9	n/a	n/a	n/a	0.5	2.9	n/a	4.5	5.9		
Edge (group)	Small α Region	3.2	61.7	8.9	3.9	5.0	10.6	2.1	0.3	n/a	n/a	0.6	4.0	n/a	19.5	5.8		
Edge (group)	Small α Region	5.8	59.6	8.8	4.1	4.9	10.4	2.0	n/a	n/a	n/a	0.5	3.4	0.4	10.3	5.7		
Edge (group)	Small α Region	13.2	56.0	7.9	4.1	4.4	9.3	1.9	n/a	n/a	n/a	0.5	2.9	n/a	4.2	6.0		
Edge	Small α Region	5.1	51.1	14.3	0.6	8.0	14.4	3.0	n/a	n/a	n/a	1.0	2.5	n/a	10.0	3.6		
Fine dot pattern		wt%														ratio		
Specimen	Metal Phase	FeO	SiO ₂	CaO	MnO	K ₂ O	Al ₂ O ₃	MgO	Na ₂ O	P ₂ O ₅	SO ₃	TiO ₂	C	Cl	SiO ₂ /FeO	SiO ₂ /Al ₂ O ₃		
Edge	Small α Region	39.8	39.4	3.7	3.5	2.2	6.6	0.9	n/a	2.1	1.4	0.3	n/a	n/a	1.0	6.0		
Edge	Small α Region	41.4	37.8	3.9	3.6	2.0	6.2	1.0	n/a	2.0	1.7	0.4	n/a	n/a	0.9	6.1		
Rib	Small α Region	40.3	37.9	4.9	2.6	2.8	6.5	1.3	n/a	0.8	0.4	n/a	2.6	n/a	0.9	5.9		
Rib	Small α Region	39.3	38.5	4.7	2.8	2.8	6.4	1.2	n/a	0.9	n/a	n/a	3.3	n/a	1.0	6.0		
Rib	Large α Region	41.7	35.9	5.1	2.9	3.1	6.3	1.1	n/a	0.7	0.5	n/a	2.6	n/a	0.9	5.7		
Rib	Large α Region	45.6	36.6	3.3	3.0	1.9	4.3	1.5	n/a	n/a	n/a	n/a	3.7	n/a	0.8	8.5		
Rib	Large α Region	35.1	44.1	3.9	1.6	1.6	6.4	1.0	n/a	0.7	0.8	n/a	3.6	1.2	1.3	6.9		
Rib	Large α Region	36.9	44.7	3.7	1.5	1.8	5.4	0.9	n/a	0.6	n/a	n/a	3.7	0.9	1.2	8.3		

Table B.6: Specimen M-CB, results on elemental composition in slag inclusions.

Circles (measured) + Matrix		wt%														ratio		
Specimen	Shape	Metal Phase	FeO	SiO ₂	CaO	MnO	K ₂ O	Al ₂ O ₃	MgO	Na ₂ O	P ₂ O ₅	SO ₃	TiO ₂	C	Cl	SiO ₂ /FeO	SiO ₂ /Al ₂ O ₃	
edge	Major string	Small α Region	100.0	n/a	n/a	n/a	n/a	n/a	n/a	n/a	n/a	n/a	n/a	n/a	n/a	n/a	n/a	n/a
edge	Major string	Small α Region	98.9	n/a	n/a	n/a	n/a	n/a	n/a	n/a	n/a	n/a	n/a	1.1	n/a	n/a	n/a	n/a
rib	Small (group) (Fig 5.25 A)	Small α Region	97.2	0.5	n/a	n/a	n/a	0.6	n/a	n/a	n/a	n/a	n/a	1.7	n/a	n/a	n/a	0.8
rib	Small (group) (Fig 5.25 A)	Small α Region	96.8	0.5	n/a	0.7	n/a	0.5	n/a	n/a	n/a	n/a	n/a	1.5	n/a	n/a	n/a	0.9
Homogeneous (glassy)			wt%														ratio	
Specimen	Shape	Metal Phase	FeO	SiO ₂	CaO	MnO	K ₂ O	Al ₂ O ₃	MgO	Na ₂ O	P ₂ O ₅	SO ₃	TiO ₂	C	Cl	SiO ₂ /FeO	SiO ₂ /Al ₂ O ₃	
edge	String (fragmented)	Pearlite Region	3.6	66.6	4.6	1.6	4.6	12.2	1.4	0.4	n/a	n/a	0.8	4.0	n/a	18.4	5.5	
edge	String (fragmented)	Pearlite Region	5.2	64.8	4.6	1.6	4.8	12.2	1.4	0.4	n/a	0.6	0.9	3.4	n/a	12.4	5.3	
edge	Irregular small	α _w Region	9.6	62.2	7.3	3.6	3.5	7.9	1.7	n/a	n/a	n/a	n/a	4.2	n/a	6.5	7.8	
rib	Small (group) (Fig 5.25 A)	Small α Region	45.1	36.2	3.6	2.7	0.8	5.7	1.0	n/a	1.4	1.6	0.3	n/a	1.7	0.8	6.4	
rib	Small (group) (Fig 5.25 A)	Small α Region	44.5	36.5	3.9	2.6	0.8	5.9	1.1	n/a	1.4	1.5	n/a	n/a	1.7	0.8	6.2	
rib	Large Irregular (group) (Fig 5.25 A)	Small α Region	31.1	47.5	4.0	1.8	0.7	8.0	1.7	n/a	1.4	1.9	1.9	n/a	n/a	1.5	5.9	
Fine dot pattern			wt%														ratio	
Specimen	Shape	Metal Phase	FeO	SiO ₂	CaO	MnO	K ₂ O	Al ₂ O ₃	MgO	Na ₂ O	P ₂ O ₅	SO ₃	TiO ₂	C	Cl	SiO ₂ /FeO	SiO ₂ /Al ₂ O ₃	
rib	Major string (Fig 5.25 A B)	Small α Region	48.4	44.3	1.8	1.0	1.0	2.8	0.5	n/a	n/a	n/a	0.2	n/a	n/a	0.9	15.8	
rib	Major string (Fig 5.25 A B)	Small α Region	48.8	39.2	1.7	1.2	1.1	2.3	0.4	0.4	n/a	n/a	n/a	5.1	n/a	0.8	17.2	
edge	String	Small α Region	55.0	36.0	1.7	1.0	0.9	2.1	n/a	0.5	n/a	n/a	n/a	3.0	n/a	0.7	17.4	
rib	Major string (Fig 5.25 A B)	Small α Region	41.9	47.2	2.9	1.4	1.2	3.8	0.8	n/a	n/a	n/a	0.8	n/a	n/a	1.1	12.4	

Neutron imaging

Nowadays, neutron imaging is popular in the research field of cultural heritage objects for multiple reasons [66]. An important aspect is that neutron imaging is a non-destructive and non-invasive technique that can be used on relatively large samples (up to tens of cm) [66]. The principle of the technique is similar to X-ray imaging method but it delivers complementary information. In contrast with X-rays, neutron imaging works with a beam of free neutrons. These neutrons interact with the nuclei of the atoms, creating a strong nuclear force (see Figure C.1b). Conversely, X-rays interact with the electron cloud and create electromagnetic force (see Figure C.1a). Neutrons have a deeper penetration due to the fact that they don't interact with the electron clouds. Moreover, as a result of the neutron interaction with the nuclei, neutron imaging can distinguish the difference between isotopes of the same element and elements that are close to each other in the periodic table [67]. Another characteristic aspect is the sensitivity to several light elements, including hydrogen. Unfortunately, there is no rule of thumb for the mass attenuation coefficients of thermal neutrons (see figure C.1c).

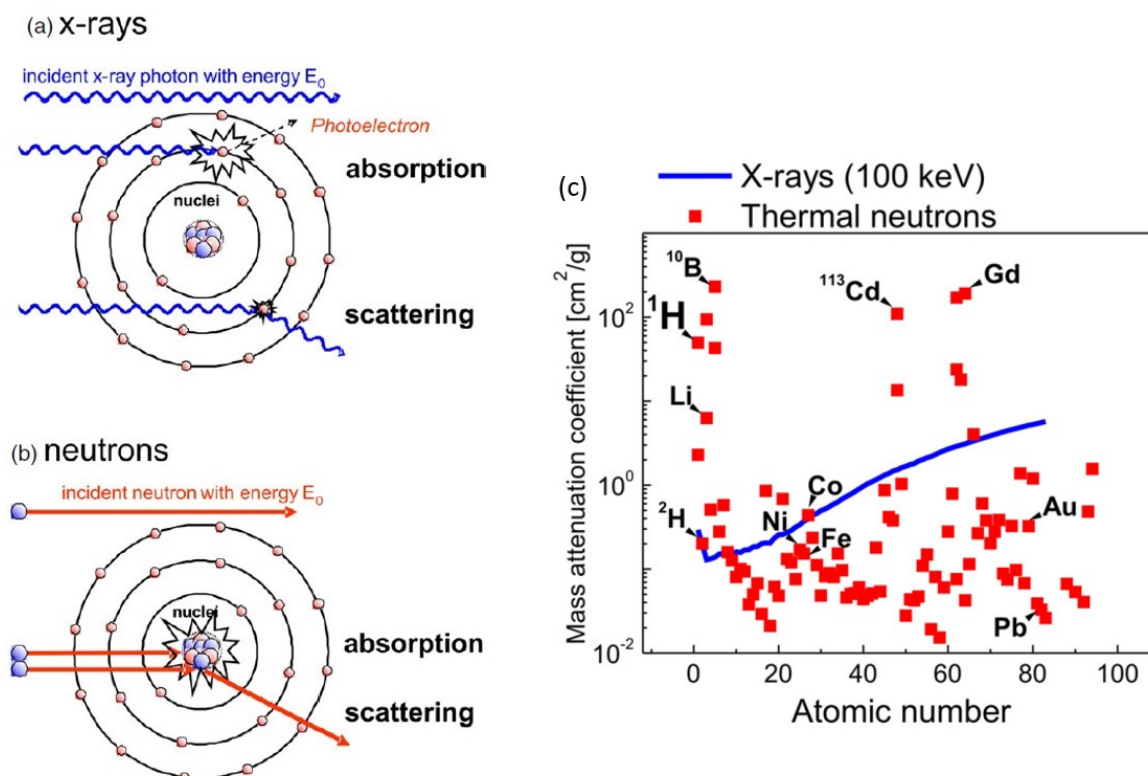


Figure C.1: Schematic illustration of A) X-ray interaction, B) neutron interaction. C) The mass attenuation coefficient vs the atomic number for both x-rays (100 keV) and thermal neutron beams. Retrieved from [67].

There are various methods for neutron imaging, each with its unique attributes. The most basic method is neutron radiography, a projection image according to the exponential Beer-Lambert attenuation law:

$$I(x, y, E) = I_0(x, y, E) \times e^{-\int_{path} \mu(x, y, z, E) ds} \quad (C.1)$$

Here I_0 is the intensity of the incident beam and I is the attenuated intensities after the beam went through the object. μ is the linear attenuation coefficient of the material and s is the path length through the object. When the object rotates (180°) on the y -axis and such a radiography image is recorded at several hundred different angles, a 3D neutron tomography image can be created. An example will be given in Section C.1 and Figure C.2. A reconstruction program is needed to translate the images (x, y) of different angles (θ) into the corresponding cross-sections derived from the 3D image. This is done via the Radon transform which results in sinograms, these are normalized and filtered before being back-projected and reconstructed into the 3D image [68].

C.1. Neutron Tomography

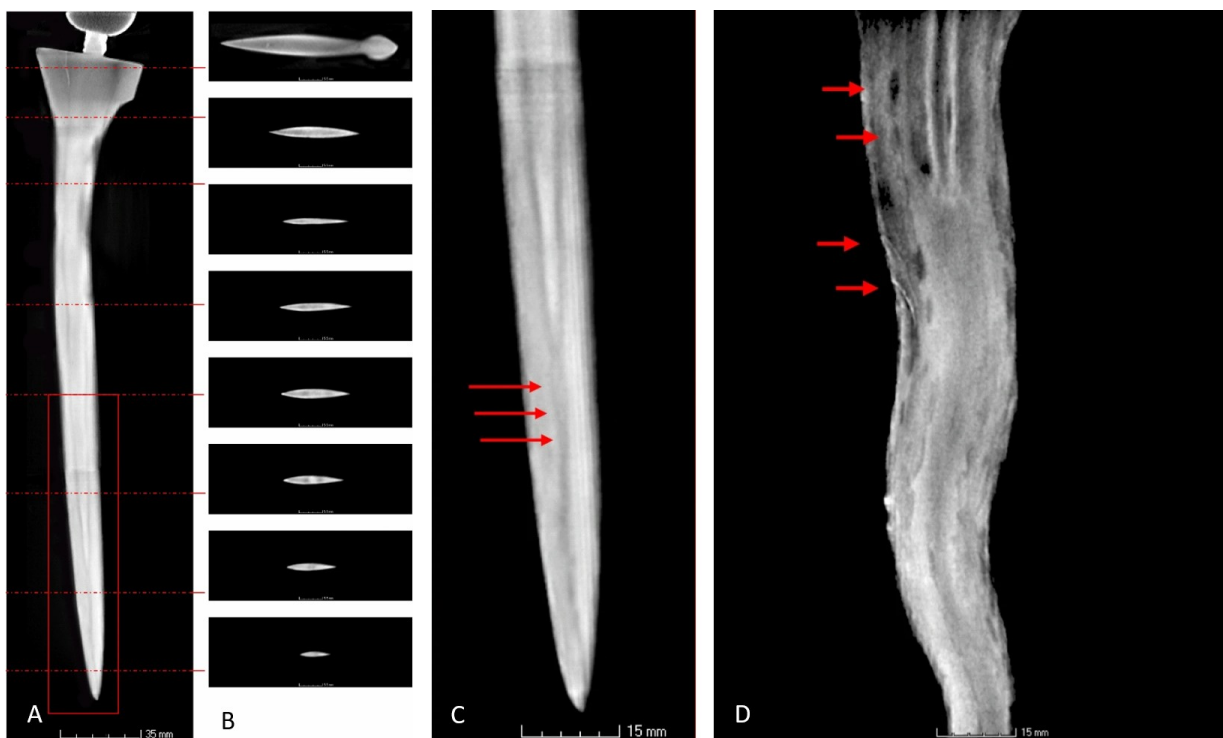


Figure C.2: White beam tomography images from the krisse researched in [69]. A) A horizontal slice through an entire blade and B) some vertical slices. C) A close-up of the tip of the blade. The red arrows point to the dark lines that represent the conjunction between layers as a result of piling. This would indicate a core layer with 2 outer layers. D) This is a close-up of another kris blade. It shows clear dark spots for slag inclusions and white lines for cracks. Retrieved from [69].

Whitebeam tomography has been applied successfully on multiple problems related to the macrostructure and microstructure of historical swords [69]–[71]. Through the 3D reconstruction of the volume and the virtual reconstruction of macroscopic cross-sections, neutron tomography can reveal many details on the buildup of the sword. Details such as the morphology of the metal, inclusions, mineralization and structural flaws [69]–[71]. Even the complicated piling pattern with up to twenty pieces of iron and steel in Indonesian kris blades can be distinguished [69]. A few examples are shown in Figure C.2. A clear layer pattern is seen in Figure C.2C, the dark line represents the area of conjunction between layers of metal. Slag inclusions are displayed by random dark spots inside the metal due to higher neutron sensitivity of the silicon dioxide present, see the upper two red arrows in Figure C.2D. Cracks that propagate into the metal are visible as white lines as corrosion product in the cracks are less sensitive for neutrons, see the lower

two red arrows in Figure C.2D. The thin layer of light gray around the metal object can be the result of a patina layer caused by etching (see Figure C.2B). Likewise, iron corrosion is displayed by a light (almost white) gray compared to the metal core [70]. Salvemini and Grazi often combine this method with Time of Flight Neutron Diffraction (ToF-ND) [69]–[72].

C.2. Time of Flight Neutron Diffraction

ToF-ND is complementary to neutron tomography, and provides a quantitative phase analysis of the crystalline structure. It can obtain details on the weight fractions and characterization of the phases, domain microstructures, defect distribution and intensity and residual stress [69], [71], [72], [74]–[76]. Diffraction patterns are based on constructive interference of a few directions of scattering and only take place when the Bragg's law is satisfied (Eq. 6) [73]. Figure C.3, shows an illustration of the diffraction of an incident beam on a set of lattice planes.

Bragg's law:

$$n\lambda = 2d' \sin\theta \quad (\text{C.2})$$

or in the first order

$$\lambda = 2d_{hkl} \sin\theta \quad (\text{C.3})$$

In order to satisfy the Bragg's law the neutron source needs a wavelength λ , which is comparable to the distance d_{hkl} between the lattice planes of the crystallographic structure [78]. If the law is satisfied the intensity I at a diffraction angle of 2θ has reached a maximum. In general, a diffractometer scan over different d_{hkl} planes is done with a fixed λ and by varying the diffraction angle. The time of flight technique works inverted; A full diffraction pattern is obtained at a fixed diffraction angle 2θ , and a polychromatic beam allows the neutrons to hit the sample with different energies (wavelengths) at the same time [78]. To discriminate the energies a pulse source is used to measure the time of flight of the neutrons from the source, through the sample, to the detector (length L). With the use of the Broglie equation, the TOF can be related to the wavelength (Eq. 8):

$$t = 505.56Ld_{hkl} \sin\theta \quad (\text{C.4})$$

When this TOF technique uses several detectors composed in diffraction banks over a range of $0 - 180^\circ$ (see Figure C.4), multiple full diffraction patterns are obtained [77]. Each diffraction bank measures the signal of a group of grains with a specific orientation [71]. When an anisotropic orientation (texture) occurs, the relative intensity of the diffraction peaks will change banks [71]. This way TOF-ND can obtain information about the texture present inside the object.

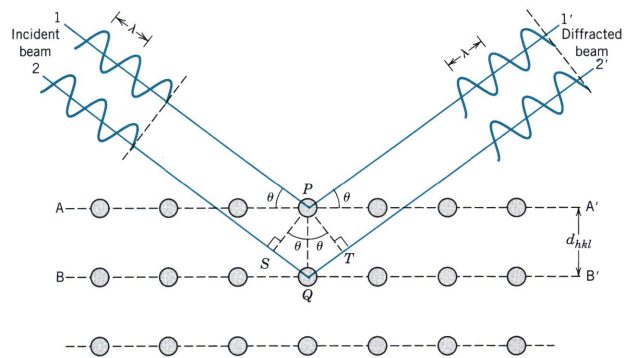


Figure C.3: Schematic illustration of the diffraction of an incident beam on a set of lattice planes. Retrieved from [73]

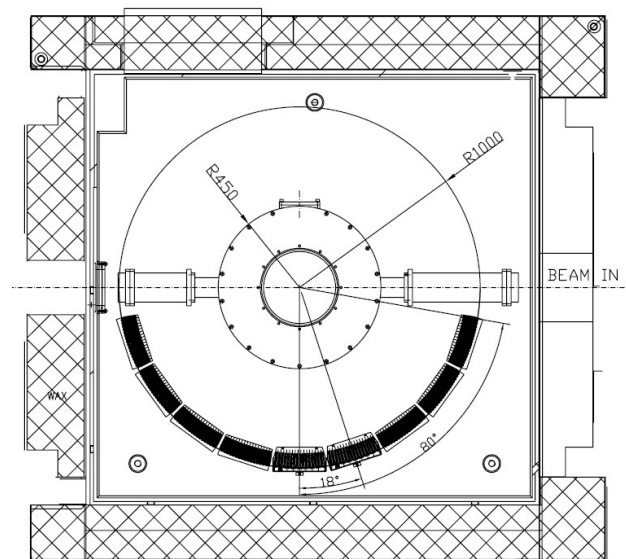


Figure C.4: Illustration of the Time of Flight Neutron Diffractometer INES at the ISIS neutron and muon source (UK). Retrieved from [77]

D

Measurements at INES

CONTINUATION PROPOSAL

HOW WERE THEY BENT? THE ART OF DISTORTING A HALLSTATT C PERIOD IRON SWORD: A NEUTRON DIFFRACTION STUDY

Ineke Joosten, Dorien Westert, Francesco Grazzi, Francesco Cantini, Antonella Scherillo, Giulia Marcucci

In the Netherlands, a few bent iron swords from the Early Iron Age Hallstatt C period were discovered [1]. The most famous bent sword was a Mindleheim-type sword found 'curled-up' inside a bronze situla in the Chieftain's burial in Oss in 1933 (Fig. 1A). Given the massive size of the barrow (53m Ø) the mourners could have elected to leave the exceptional sword straight and deposit it alongside the bronze urn, but instead they invested time and effort into bending the sword. Why? In addition to the sword from Oss, several other bent swords dating to the Hallstatt C period have been found in the Netherlands, for example, the sword-grave of Heythuizen and the wagon-grave of Wijchen (Fig. 1B-C). The question remains, how were these swords bent, by brute force or by heating and hammering? Could this have been done at the place of burial or was it necessary to bring the sword to a smithy? Knowing how the swords were bent, implies the knowledge, skills and equipment of people in this period and thus adds to the archaeological framework around the Hallstatt culture and burials found in the Netherlands. The aim of this research is to study the bending process on the basis of the microstructure of the swords, preferably by non-invasive methods. Therefore, the structure and composition of the metal (and the corrosion) will be studied through neutron imaging and diffraction. Fortunately, we could sample one of the swords which enables us to perform a complementary method, SEM-EBSD. The results of neutron imaging will be compared to the metal structure seen in the cross-sections [2].

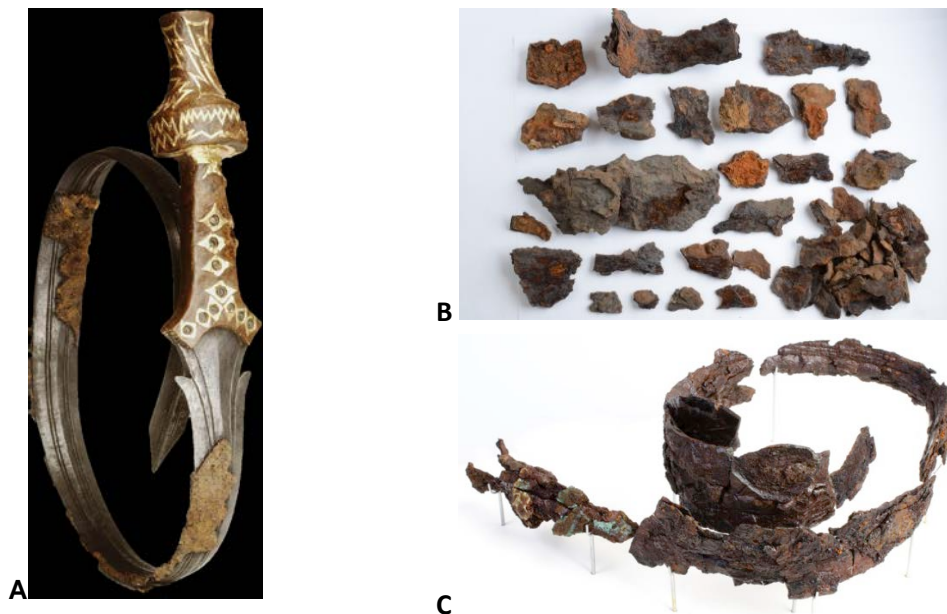


Fig. 1. A: Mindelheimsword from Oss (Photo by P.J. Bomhof, RMO), B: Sword from Heythuizen-Bisschop (photo by J. van Donkersgoed), C: Sword from Wijchen (photo by J. van Donkersgoed)

Preceding Experiments, Proposed Experiment and Expected Results

In order to obtain metallurgical information about the composite structure of these swords, we performed a combined analysis of neutron diffraction and neutron imaging, which provide the best combination of morphological and structural details [3-4]. Neutron diffraction was used to characterise the material in terms of crystalline phases and microstructure. In particular, we aimed at understanding how the sword was bent by identifying residual stress. Specifically, by measuring the distribution and the intensity of the residual stress it is possible to distinguish if the sword was bent with or without heating. Residual stresses are determined by analysing the Gaussian broadening of the ferrite diffraction peaks.

During the preceding experiment RB 2220462 (1), we encountered some obstacles due to a paraloid conservation treatment on the sword from the Wijchen excavation site, that induced a very high background thanks to its high hydrogen content. This, combined with the heavy corrosion of the sample,

made impossible to study the Ferrite peak, as clearly seen in Fig. 2. To clarify this situation, we propose additional neutron diffraction measurements on untreated pieces of the Wijchen sword, larger than the very small one already measured, since they are more representative of the entire sword, that were not incorporated into the restored museum pieces (Fig. 1C).

Furthermore, NRCA elemental analysis simultaneous to the neutron diffraction measurements, revealed the presence of arsenic only in the sword pieces of Heythuizen. The presence of such a substitutional element has an influence on the lattice parameter of the ferrite phase. To clarify if shift observed in the lattice parameter of ferrite in the Heythuizen samples (see Fig. 2) and see a distinct difference in the elemental composition of both Heythuizen and Wijchen swords, potentially explaining the origin of the iron ore, we propose a more detailed elemental analysis by means of transmission measurements (NRTI)[5].

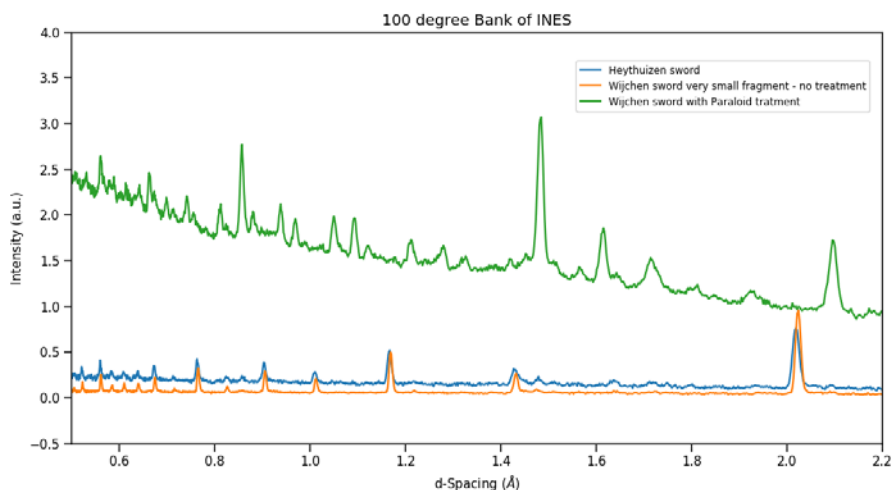


Fig. 2: Comparison between diffractograms obtained for a very small untreated sample of the Wijchen sword, the Wijchen treated sword, and the Heythuizen sword. In particular, the main ferrite peak around 2 Angstrom clearly shows a shift probably due to As in the iron alloy in the Heythuizen sword and the very small fragment of the Wijchen sword, and is not visible due to the very high background induced by corrosion and hydrogen from paraloid in the Wychen sword.

The samples we propose to measure include 3 pieces up to 2 cm in height and width from the Wijchen sword and 1 sample up to 3 cm in height and width from the Heythuizen sword. The NRTI measurements will be performed using the INES pixelated 2D transmission detector, in order to characterize the composition and the homogeneity of the samples. The fragments of the swords will be mounted on a specially prepared aluminium frame and encapsulated within aluminium sheets; the pieces will be aligned on the beam-line by exploiting the INES laser blades system.

We estimate that 400 μ amps (about 2.5 h) of integrated beam current will be necessary to give good statistics in the measured points for the diffraction measurements, and 2000 μ amps (about 12 h) of integrated beam current, assuming an average ISIS current of about 170 μ amps. Considering we propose to measure the 3 pieces with neutron diffraction and 2 pieces with gamma elemental analysis, we ask for 3 days of beam time, including set-up time of the samples and the transmission measurements (about 1 day).

The results obtained will be disseminated through standard methods such as publication in peer-reviewed scientific journals and presentations at international conferences.

Bibliography

- [1] S. Van der Vaart-Verschoof, (2017)
- [2] F. Salvemini et al. Eur. Phys. J. Plus **129**, 1 (2014)
- [3] F. Grazi et al. J. Arch. Sci. Rep. **20**, 834 (2018)
- [4] F. Salvemini et al. Eur. Phys. J. Plus **135**, 1 (2020)
- [5] A. Fedrigo, et al. J. Anal. At. Spectrom., **34**, 12 (2019)